Universitat Politècnica de Catalunya
Programa de Doctorat de Matemàtica Aplicada

Departament de Matemàtica Aplicada III

# Title of the dissertation: Shock capturing with Discontinuous Galerkin methods

by Eva Casoni

Doctoral Thesis
Advisor: Antonio Huerta

Barcelona, July 2011

## Abstract

Title of the dissertation:
Shock capturing with Discontinuous Galerkin methods

Eva Casoni

This thesis proposes shock-capturing methods for high-order Discontinuous Galerkin (DG) formulations providing highly accurate solutions for compressible flows.

In the last decades, research in DG methods has been very active. The success of DG in hyperbolic problems has driven many studies for nonlinear conservation laws and convection-dominated problems. Among all the advantages of DG, their inherent stability and local conservation properties are relevant. Moreover, DG methods are naturally suited for high-order approximations. Actually, in recent years it has been shown that convection-dominated problems are no longer restricted to low-order elements. In fact, highly accurate numerical models for High-Fidelity predictions in CFD are necessary. Under this rationale, two shock-capturing techniques are presented and discussed.

First, a novel and simple technique based on on the introduction of a new basis of shape functions is presented. It has the ability to change locally between a continuous or discontinuous interpolation depending on the smoothness of the approximated function. In the presence of shocks, the new discontinuities inside an element introduce the required stabilization thanks to the numerical fluxes, thus exploiting DG inherent properties. Large high-order elements can therefore be used and shocks are captured within a single element, avoiding adaptive mesh refinement and preserving the locality and compactness of the DG scheme.

Second, a classical and, apparently simple, technique is advocated: the introduction of articial viscosity. First, a one-dimensional study is perfomed. Viscosity of the order $\mathcal{O}(h^k)$ with $1 \leq k \leq p$ is obtained, hence inducing a shock width of the same order. Second, the study extends the accurate one-dimensional viscosity to triangular multidimensional meshes. The extension is based on the projection of the

one-dimensional viscosity into some characteristic spatial directions within the elements. It is consistently shown that the introduced viscosity scales, at most, with the DG resolutions length scales, $h/p$. The method is especially reliable for high-order DG approximations, say $p \geq 3$.

A wide range of different numerical tests validate both methodologies. In some examples the proposed methods allow to reduce by an order of magnitude the number of degrees of freedom necessary to accurately capture the shocks, compared to standard low order h-adaptive approaches.

# Acknowledgments

I would like to thank my advisor, Antonio Huerta, for giving me the opportunity of developing a thesis and bringing me to the research world. Thanks for providing all the rigor and the highest quality in this work and for teaching me to be a good researcher.

I specially would like to express my gratitude to professor Jaime Peraire for giving me the chance to spend ten months in the *Aerospace Computational Design Laboratory* at the MIT. Many thanks for his suggestions, guidance and dedication. Thanks to Ale and Britt for their invaluable hospitality and support. I can only smile when I remember the cold evenings in the lab. And thanks to Masa, for spending so many hours of the snowy Sundays helping me with all the implementation details in C and the problems with the cluster. My deepest gratitude to Jewel and Judy for making me feel home in the cold Boston. Thanks to *Agència de Gestió d'Ajuts Universitaris i de Recerca* (AGAUR) for the financial support.

I also would like to thank all the people in *LaCàN* that has shared some part of my PhD. Thanks to Sonia for the mathematical discussions and support. I made with her my first steps in DG methods. To Agus for his confidence and giving me the opportunity to work with him, and making it such as easy. To Xevi and David for the constant technical and personal support. And for all the moments that you both make me laugh. Thanks to Imma for solving all the administrative work and for being a friend. A heartfelt thanks to Esther, for being there when it matters, in all senses. My deepest gratitude goes to Rubén, for all the insightful discussions, suggestions and conversations. Thanks to Adeline, who also continued with *that work*. I really acknowledge her encouragement in this final year. I feel so lucky to have coincided with both of them.

Many people between *la sala de gràfics* and *la 208*. Special thanks to Alba that lives *in the other room*. And from my small place in room 208, many thanks to Jordi and Óscar for being there in this hard last year (and for all the patience). Special mention to Cris, for all her energy spread, and for being such a good friend.

I am very grateful to Sergi and to Esteve, for being by GPS. Special thanks to Esteve for showing me the trick of all the things: never throw in the towel.

Thanks to all the people *outside the scenario of the thesis*. I can't forget mentioning Rut and Alba for their friendship, even not being physically. And Elena, for being there in the tough times.

Finalmente, y por encima de todo, gracias a mi familia. A la Laia que, sin saberlo, ha sido uno de los principales motores de esta tesis. Y a mis padres, por respetar y apoyarme en todas las decisiones que he tomado, incluso a veces sin entenderlas. Gracias mil por hacerme mirar siempre adelante.

Partial financial support of this thesis has been provided from the grants of *Agència de Gestió d'Ajuts Universitaris i de Recerca* and *Generalitat de Catalunya*, and also from *Universitat Politècnica de Catalunya*. Their support is gratefully acknowledge.

# Contents

# List of Figures

# List of Tables

# Chapter 1

# Introduction

The increase in computational power over recent years enables the simulation of multiple engineering problems involving complex physical processes. Among them, Computational Fluid Dynamics (CFD) is a clear example in which high-fidelity simulations are mandatory. CFD is the branch of fluid mechanics that, by means of numerical methods and algorithms, solves flow problems. Nowadays it is an essential tool for engineering design and analysis. It is impossible to imagine, for instance, in the aerodynamic or automotive industries a design process without a computer aid. Today CFD is used as a viable alternative and complement to experimental measurements, offering advantages in terms of cost, time and data acquisition.

## 1.1 Motivation

Computer simulation of flow phenomena covers a wide range of applications, such as aircraft designs, blood flow simulations, external car aerodynamics, indoor and outdoor air simulations and combustion, among many others. Although young, the field of CFD has matured enough to effectively solve problems involving complicated geometries and complex features. However, far from being a closed field, CFD deals with many challenging problems. Consider, for instance, the motion of a compressible fluid under the effect of an explosion: the extremely large velocities, usually greater than the speed of sound, and the abrupt changes of the physical quantities occur in

a very short period of time and different space scales. Currently there is a lack of general robust and accurate numerical schemes to attack these kind of problems and obtain high-fidelity solutions.

In problems where high-accuracy is needed spectral methods, based on Fourier expansions, are usually applied. This contrasts with the polynomial approximations, almost universally accepted for numerical simulations, and shows the particular character of these problems. For a review of these techniques see for example the works developed by Mavriplis (1994) and Gottlieb and Hesthaven (2001). Spectral methods are able to achieve very high-accuracy, but its use on complex geometries, requiring unstructured meshes common in CFD simulations, is still an open problem. In this context, high-order polynomials appears as one viable alternative, see Silvester (1969) or Hesthaven and Warburton (2002).

Shock waves are characterized by an abrupt, nearly discontinuous change in the characteristics of the medium. It is a common fact in compressible flow models the existence of shocks waves and choked flow (which is associated to the Venturi effect, and only limits the velocity of the mass flow rate). Mathematically both effects are modeled as discontinuities, hence becoming a serious handicap in high-order methods. In fact, for problems involving both, strong shocks and also smooth flow, the shocks can limit the order of accuracy in a significant region surrounding the shock.

The dichotomy between high-order and shock-capturing is the main focus of this thesis. High-order accuracy and shock-capturing presents as contradictory ideas. Shock waves can only be captured with first-order schemes, as stated by Godunov (1954) and Harten (1983). The use of high-order will cause the appearance of spurious oscillations that will lead the solution to be unstable. On the contrary, low order approximations produce an excessive smearing of the solution, leading to physically unacceptable results. Hence, a compromise should be taken between high-order accuracy and shock-capturing.

## 1.2 Objectives

The objective of this PhD thesis is the development of robust shock-capturing methods for high-order Discontinuous Galerkin (DG) finite element method and apply them to model problems in compressible flow, for transonic and supersonic flows.

For this purpose, the following partial goals are considered:

1. **To preserve high-order approximations.** The main drawback of actual shock-capturing methods is the loss of high-order. In fact, the actual tendency is to use low-order approximations combined with mesh adaptivity. However, changes in shock strength, cell size and orientation usually introduce errors that can convect downstream and pollute the solution also far away of the shock. Hence, the global accuracy is reduced to first order, not only in the shock area, where low degree approximations are used, but also in a large part of the domain. One of the main goals of this thesis is to overcome this drawback. First, the method presented in Chapter 2 allows to use large high-order elements, preserving the locality and compactness of the method. Numerical tests consistently show that the high-order degree is kept in the large majority of the domain and only in the elements where the shock is contained the solution is approximated with a combination of piecewise-constant and continuous shape functions. Second, in Chapter 3 an artificial diffusion method for high-order DG is presented. In the vicinity of shocks the approximation is not systematically reduced to first order, in fact, is kept as high as possible .

2. **To permit the use of large high-order element without h-adaption** As pointed out, the most obvious and standard methodology to capture shocks is to reduce the order of the approximation in the vicinity of shocks. However, to preserve high-accuracy it is necessary to adaptively refine that region by locally decreasing the mesh size, $h$. In this work the goal is to maintain high-order accuracy without $h$-adaptive process, hence reducing the computational overhead of mesh adaptivity, especially relevant for DG (recall that DG methods duplicate nodes). As it will be shown in the numerical tests, sub-cell resolution

is obtained and the different scales of the flow are captured without changing the topology of the mesh.

3. **To obtain shock width less than the element size.** The resolution given by a polynomial of order $p$ scales like $h/p$. This means that the amount of viscosity required to resolve a shock profile is only $\mathcal{O}(h/p)$. When very large high-order elements are used an accurate solution requires the shock to be contained within a single element without smearing. In Chapter 3 an artificial diffusion method is presented. The introduced viscosity scales like $\varepsilon \sim \mathcal{O}(h^k)$ for some $1 \leq k \leq p$, hence obtaining a shock width thinner than $h/p$, as numerical tests consistently show.

4. **To obtain a robust method easily extensible to multiple dimensions.** Many effective shock-capturing methods have been defined for one-dimensional problems, providing stable and accurate solutions, see for example Cockburn and Shu (1989), Biswas et al. (1994) or Krivodonova (2007). However, their extension to higher dimensions involves several difficulties, such as the directionality, the introduction of problem-dependent parameters, the necessity of an structured mesh or the loss of high-order, among many others. In Chapter 2 a simple shock-capturing method based on the modification of shape functions is presented. The approach is simple, based only on a single parameter which automatically modifies the approximation depending on the smoothness of the solution. Results show the robustness of the method, which only depends on a linear function $\alpha$ that takes value from 0 to 1, depending on the smoothness of the solution. Same function is used with independence of the test to be solved. Numerical tests demonstrate that small modifications on the value $\alpha$ do no have a major consequence in the overall solution. The artificial diffusion method defined in Chapter 3 appears as a robust technique since it does not require any parameter. It can also be extended to higher dimensions for any degree of approximation and any complex geometry. The extension is based on the one-dimensional projection of the solution along some characteristic direc-

tions, and hence, it can be generalized for any spatial dimension. However, in this work only the two-dimensional case is considered.

5. **To develop a code for solving compressible flows with high-order DG.** When highly accurate simulations are needed, computational costs using current techniques imply the use of very fine meshes or very high-order approximations, or even both. The number of total amount of degrees of freedom increases dramatically. Moreover, the use of specific techniques that are required to ensure the stability of the scheme avoiding spurious oscillations, also implies more involved computations with an increase in computational cost, in terms of time and memory requirements. A code for standard high-order DG methods incorporating both, the continuous-discontinuous shock-capturing method of Chapter 2 and the artificial diffusion scheme of Chapter 3, has been developed also in the context of this thesis. The code has been implemented in Matlab and later translated to C language, due to the excessive CPU time of the steady state simulations to converge. Efficient strategies for the element-by-element formulation and face integrals have been use, also including ordering algorithms for the optimal treatment of nodes and elements. For comparison purposes, the slope limiting techniques by Biswas et al. (1994) and a classical FV method, see for instance LeVeque (2002), have been also implemented.

6. **To verify the method with different sets of equations: convection-dominated problems and Euler equations.** Several problems of different nature, steady and unsteady, have been tested with the two approaches presented in this thesis. In both cases the methods provide stable and highly accurate results, maintaining the properties and goals described above. Both techniques can be used to solve any compressible problem or either convection-diffusion equation, since they do not involve any problem-dependent parameter. Both methods are compared, through numerical tests, with classical shock-capturing approaches, such as the slope limiting techniques and the Finite Volume method with h-adaption.

## 1.3 Sate of the Art

### 1.3.1 Discontinuous Galerkin methods

In the last decades Discontinuous Galerkin finite element methods have centered many studies for the simulation of CFD. The DG method combines in an optimal manner the high-order discretization tools of the general Galerkin finite elements and the local conservation properties typical of Finite Volume (FV) technology, which has been successful in the simulation of flows with discontinuities, see for instance the work by Barth (1994) or the monograph by LeVeque (2002). The essential idea of DG is to use element-by-element discontinuous approximations, enforcing continuity across the elements in a weak form by means of the numerical fluxes.

Thanks to its attractive properties, DG appears as a good solution for the development of high-order accurate methods, using structured and unstructured grids. First, high-order approximations can be easily built, just by increasing the order of the approximating polynomial within each element. The element-by-element formulation makes these methods well-suited for $p$-adaptive discretizations on both, structured and unstructured meshes, providing also a compact scheme. Second, the introduction of fluxes at the discontinuous element boundaries allows the elementwise coupling, but it also provides an inherent stabilization of the method. However, in the context of discontinuous solutions and non-linearities, this natural stabilization is not enough for high-order ($p \geq 2$) approximations.

The DG method was first introduced by Reed and Hill (1973) for solving the neutron transport equation. One year later, Lasaint and Raviart (1974) presented the first numerical analysis of the method for a linear advection equation. Johnson and Pitkäranta (1986) extended the analysis for general triangulations, improving the error estimate to $\mathcal{O}(h^{p+1/2})$. This result was later confirmed numerically by Peterson (1991) to be optimal. For structured non-Cartesian grids, Richter (1988) also improved the estimate to $\mathcal{O}(h^{p+1})$.

The first extension to nonlinear problems was carried out by Chavent and Salzano (1982), by using the Godunov's Riemann solver to evaluate the flux across element

boundaries. Riemann solvers are common in FV methods, see Toro (1999); LeVeque (2002). Since their apparition, there has been a rapid proliferation of new DG techniques as well as many analyses and applications. The work developed by Cockburn, Shu and co-authors in the decade of the 90's, see the series of papers Chavent and Cockburn (1989); Cockburn and Shu (1989); Cockburn et al. (1989, 1990); Cockburn and Shu (1998a), serves as a point of reference for the DG community in nonlinear problems. They introduce the Runge-Kutta Discontinuous Galerkin (RKDG) method for nonlinear hyperbolic problems, which was initially designed for Finite Difference (FD) and FV methods, see Shu and Osher (1988) and LeVeque (1992), to ensure Total Variation Diminishing (TVD) approximations. This method was later generalized to be high-order accurate in time as well as space, see Shu (1988) and Spiteri and Ruuth (2002).

DG methods originally were intended for purely hyperbolic problems. The excellent results obtained led its extension for convection-diffusion problems. The first attempt was made by Arnold (1982) in his PhD thesis, proposing an interior penalty method with Discontinuous finite elements. Since then a great effort was put in the construction of different schemes for the discretization of viscous terms. For instance, Bassi and Rebay (1997a, 2001) demonstrated the capabilities of DG for the Navier-Stokes equations and Baumann and Oden (1999) proposed a discontinuous *hp* method for general convection-diffusion equations. Cockburn and Shu (1998b) introduced the *Local Discontinuous Galerkin* (LDG) formulation, which has been successfully analyzed and generalized to many equations, see for instance the work by Sherwin et al. (2006) devoted to reduce the stencil of LDG. It is of particular interest the work by Brezzi et al. (2000) and Arnold et al. (2001) that makes an effort to summarize all the different techniques. Recently, based on LDG, some methods arise with the aim of providing a more compact stencil: the *Compact Discontinuous Galerkin* (CDG), introduced by Peraire and Persson (2008) and more recently, the *Hybridizable Discontinous Galerkin* (HDG) by Cockburn et al. (2009), which is focusing researchers' attention.

### 1.3.2 Shock-capturing

One of the biggest challenges of using high-order unstructured solvers is their inability to handle flow discontinuities. A considerable development of shock-capturing techniques have emerged during the last 40 years. The following is a brief overview with an historical perspective.

#### Artificial diffusion

The key of shock-capturing schemes is dissipation. In fact, artificial diffusion was already proposed in the 50's by Von Neumann and Richtmyer (1950). It consists on explicitly adding viscous terms to the governing partial differential equation. Lapidus (1967) followed the same idea and presented another early artificial diffusion method for FD. However, reincorporating the relevant physics in nonlinear hyperbolic conservation is not trivial, see for instance Cockburn (2001). Following the idea of Streamline Upwind Petrov-Galerkin (SUPG) methods for Finite Elements, proposed by Hughes et al. (1986); Hughes and Mallet (1986a,b), several authors introduced an artificial diffusion term based on residual quantities and applied it to the solution of Euler and Navier-Stokes equations, see for instance the relevant works by Bassi and Rebay (1997b), Bassi and Rebay (1997a) and Hartmann (2006). However, the inherent difficulties in determining where and how much viscosity must be introduced without causing unnecessary smearing have deterred the extensive use of the artificial diffusion approach.

Persson and Peraire (2006) presented an artificial viscosity term based on the mesh size, $h$, and the degree of the interpolating polynomial, $p$. The idea behind the method is to spread the discontinuity over a length scale so that it can be resolved in the space of interpolating functions. Introducing artificial viscosity that scales like $h/p$ gives a shock of width $\delta = Ch/p$, for some $C \geq 1$. Based on the same idea, Barter and Darmolfal (2007) propose a smoother representation of articial viscosity, rather than the piecewise constant approach of Persson and Peraire. Both approaches are complemented with a shock detection algorithm which is based on the rate of decay

of the expansion coefficients of the solution.

### Limiting

Another older and successful approach for shock-capturing methods is limiting techniques. These methods were initially designed in the context of FD and FV and induced a Total Variation Diminishing scheme, which was introduced by the series of papers by van Leer (1974, 1977a,b, 1979). A general overview of these methods is given by LeVeque (1992). Slope limiting for DG was extended by Cockburn and Shu (1989),Cockburn and Shu (1998a) and Cockburn and Shu (2001), commonly known as RKDG methods. They combine approximate Riemann solvers and nonlinear operators (i.e. slope limiters) in order to satisfy Total Variation Bounded in the means (TVBM). This approach has become one of the more popular techniques for shock-capturing in DG, see for instance the high-order extensions by Biswas et al. (1994) and Krivodonova (2007). Despite yielding satisfactory solutions, the main drawback of these techniques lies in the fact that they drastically reduce the order of the approximations in the vicinity of shock. Thus, mesh adaption (refinement) procedures are needed. In fact, reducing the order of the interpolating polynomial is equivalent to add diffusion of the order of the mesh size, $h$. Moreover, the extension to multi-dimensional problems is not straightforward. On one hand, Goodman and LeVeque (1985) proved that, except in very especial cases, any method that is TVD in two space dimensions is at most first order accurate. On the other hand, recall that adaption should incorporate mesh directionality because shocks are lower dimensional structures. Several approaches, based on Cockburn's work, have been proposed, see for instance the interesting works by Burbeau et al. (2001) and Kuzmin (2010). However, nowadays high-order limiters still need further improvement.

### ENO and WENO reconstruction methods

Lately, high-order non-oscillatory reconstruction methods, known as (weighted) essentially non-oscillatory (ENO or WENO) approaches, are focusing researchers' at-

tention. These methods were first proposed by Harten et al. (1987) and Harten and Osher (1987) with the idea of keeping high-order approximations. With that purpose, they use additional degrees of freedom to resolve sharp profiles, also preserving nonlinear stability. They were first used in the context of FD, see for instance the extensive work by Shu and Osher (1988, 1989), but later extended to FV, see Casper and Atkins (1993) and Abgrall et al. (1999). However, despite their attractive features, these techniques have some important drawbacks that preclude their extensive use. For instance, their computational overhead is excessive for high-order approximations, they require structured grids, they may loose robustness for high-order schemes, and to date their extension to multiples dimensions has not yet been demonstrated. Nonetheless, a considerable progress has been done in this direction (Luo et al. (2007); Zhu et al. (2008)), and nowadays this is an active area of research.

**Non-polynomial approximations: vanishing spectral viscosity**

High-accuracy is directly related to spectral methods, see Gottlieb and Hesthaven (2001). As in many other numerical methods, the formation of Gibbs phenomenon due to spontaneous shock discontinuities in the solution is one of its greatest challenges. In the context of spectral methods, stabilization is carried out by adding viscosity to the different spectral scales of the solution, commonly known as *vanishing viscosity*. Vanishing viscosity was mainly developed by Tadmor (1990) and Maday et al. (1993) in the early 90's. However, since it is a spectral method, it suffers from the main drawback of these techniques: since date they have not yet been demonstrated in the practical unstructured mesh context. Recently, Liu et al. (2006) proposed the Spectral Difference (SD) method, which is an efficient high-order approach based on differential form of the governing equation. In their work they show very promising results on triangular grids. Premasuthan et al. (2010) also proposed an artificial viscosity approach to the SD method for high-order computation of compressible fluid flows with discontinuities.

# 1.4 Discontinuous Galerkin discretization and the Compressible Euler equations

## 1.4.1 Compressible Euler equations

Euler equations of gas dynamics express the conservation of mass, momentum and energy in a compressible, inviscid and non-conducting fluid. The strong form of these conservation laws is

$$\begin{aligned} \frac{\partial \rho}{\partial t} + \boldsymbol{\nabla} \cdot (\rho \boldsymbol{v}) &= 0 \\ \frac{\partial \rho \boldsymbol{v}}{\partial t} + \boldsymbol{\nabla} \cdot (\rho \boldsymbol{v} \otimes \boldsymbol{v} + p\mathbf{I}) &= \rho \boldsymbol{b} \\ \frac{\partial \rho E}{\partial t} + \boldsymbol{\nabla} \cdot ((\rho E + p)\boldsymbol{v}) &= \boldsymbol{v} \cdot \rho \boldsymbol{b} \end{aligned} \tag{1.1}$$

where $\rho$ is the density, $\rho \boldsymbol{v}$ is the momentum, $\rho E$ is the total energy per unit volume of the fluid, $p$ is the pressure and $\rho \boldsymbol{b}$ is the external volume force per unit volume, see Donea and Huerta (2003) for more details.

An equation of state, relating the internal energy $e = E - \frac{1}{2} \parallel \boldsymbol{v} \parallel^2$ to pressure $p$ and density $\rho$ is needed to complete the system of nonlinear hyperbolic equations. For a perfect polytropic gas, the equation of state is

$$p = (\gamma - 1)\rho\Big(E - \frac{1}{2} \parallel \boldsymbol{v} \parallel^2 \Big)$$

where $\gamma$ is the ratio of specific heat coefficients (specific heat at constant pressure, $c_p$, over specific heat at constant volume, $c_v$), with value $\gamma = 1.4$ for air.

The speed of sound, $c$, is also common in this formulation. It enters the definition of the Mach number

$$M = \frac{\parallel \boldsymbol{v} \parallel}{c},$$

and it is given by $c = \sqrt{\gamma p / \rho}$.

The system of nonlinear hyperbolic equations (1.1) can be rewritten in vector form as

$$\frac{\partial \mathbf{U}}{\partial t} + \frac{\partial \mathbf{F}_k(\mathbf{U})}{\partial x_k} = \mathbf{B},\ k = 1, \ldots, \mathrm{n_{sd}}, \tag{1.2}$$

where $\mathbf{U}$ is the vector of conservation variables, $\mathbf{F}_k$ are the associated flux vectors for each spatial dimension, with $\mathrm{n_{sd}}$ the number of spatial dimensions, and $\mathbf{B}$ is a source term. They are defined as follows:

$$\mathbf{U} = \begin{pmatrix} \rho \\ \rho \boldsymbol{v} \\ \rho E \end{pmatrix}, \quad \mathbf{F}_k(\mathbf{U}) = \begin{pmatrix} \rho \upsilon_k \\ \rho \boldsymbol{v} \upsilon_k + \mathbf{e}_k p \\ (\rho E + p)\upsilon_k \end{pmatrix},\ k = 1, \ldots, \mathrm{n_{sd}}, \text{ and } \mathbf{B} = \begin{pmatrix} 0 \\ \rho \boldsymbol{b} \\ \boldsymbol{v} \cdot \rho \boldsymbol{b} \end{pmatrix}$$

where $\mathbf{e}_k$ is the unitary vector in the $x_k$ direction.

The chain rule yields an equivalent quasi-linear formulation by rewriting the flux components as

$$\mathbf{F}_k(\mathbf{U}) = \mathbf{A}_k(\mathbf{U})\mathbf{U},$$

where $\mathbf{A}_k(\mathbf{U}) = \partial \mathbf{F}_k / \partial \mathbf{U}$, for $k = 1, \ldots, \mathrm{n_{sd}}$, are the Jacobian matrices. Due to the hyperbolicity of the Euler equations, any linear combination of the Jacobians is diagonalizable with real eigenvalues. However, by considering an arbitrary direction $\mathbf{j} = (j_1, \ldots, j_{\mathrm{n_{sd}}})$ of the space, the projection of Jacobian matrices along this direction admits the following factorization

$$\mathbf{A}_{\mathbf{j}} = \sum_{s=1}^{\mathrm{n_{sd}}} j_s \mathbf{A}_s = \mathbf{R}\boldsymbol{\Lambda}(\mathbf{j})\mathbf{R}^{-1} \tag{1.3}$$

where $\mathbf{R}$ is the matrix of right eigenvectors and $\boldsymbol{\Lambda}(\mathbf{j})$ is the diagonal matrix of eigenvalues.

For the rest of the thesis, the homogeneous form of the Euler equations will be considered, that is $\mathbf{b} = \mathbf{0}$ in Equation (1.1). For a detailed presentation of the Euler equations see classical text books such as Anderson (1984) and Hirsch (1990).

### Boundary conditions

The treatment of boundary conditions of the Euler equations is an issue of relevance. Its influence on the existence and uniqueness of solutions and also on the simulation results should not be underestimated.

In general, Euler equations are defined over a computational domain $\Omega$ delimited by an external boundary. The number of boundary conditions to be imposed at the boundary depends on the pattern of wave propagation. A proper control of characteristic variables is typically sufficient to determine the incoming and outcoming waves in the boundary. By a linearized Riemann analysis in the direction of the outward normal to the contour, the system (1.2) is transformed into its canonical form, which consists on $\mathrm{n_{comp}}$ decoupled convection equations

$$\frac{\partial \omega_k}{\partial t} + \lambda_k \frac{\partial \omega_k}{\partial x} = 0, \quad k = 1, \ldots, \mathrm{n_{comp}} \tag{1.4}$$

where $\mathrm{n_{comp}}$ is the number of components of the solution $\mathbf{U}$, $\omega_k$ are the characteristic variables, also called *Riemann invariants*, and $\lambda_k$ are the eigenvalues of the jacobian matrix of (1.3). Note that the eigenvalues depend on the selected direction. It follows that the evolution of the characteristic variables is described by simple waves propagating independently of one another along the outward normal, with velocities $\lambda_k = v_n, v_n \pm c$. Here, $v_n = \boldsymbol{v} \cdot \mathbf{n}$ stands for the normal velocity. For a pure convection equation, boundary conditions are required only at the inlet (incoming information). Hence, the number of boundary conditions to be prescribed correspond to the number of negative eigenvalues, that is $\lambda_k < 0$. Since $\lambda_k$ depends on the normal velocity $v_n$ and the speed of sound $c$, the direction of wave propagation depends directly on the local Mach number $M = |v_n|/c$. According to the range of values of Mach number different categories of flow regime may be described, see Anderson (1984). However, for the treatment of boundary conditions only two relevant cases have to be considered: supersonic and subsonic flow.

Supersonic flow is considered when the local Mach number is such that $M = (|v_n|/c) \geq 1$

- Supersonic inflow boundary

  At the inlet $v_n < 0$ and all $\lambda_k$ are negative; the values of all characteristic variables must be specified.

- Supersonic outflow boundary

  At the outlet $v_n > 0$ and all $\lambda_k$ are positive; no physical boundary conditions may be imposed.

Analogously, subsonic flow is considered when $M = (|v_n|/c) < 1$

- Subsonic inflow boundary

  At the inlet $v_n < 0$ so that only the velocity associated to the last characteristic variable, $\lambda_{\mathrm{n_{sd}}+2} = v_n + c$ is positive; the first $\mathrm{n_{sd}} + 1$ Riemann invariants must be specified.

- Subsonic outflow boundary

  At the outlet $v_n > 0$ and only the first eigenvalue $\lambda_1 = v_n - c$ is negative; just one condition is to be prescribed.

Finally, at solid wall boundary, which corresponds to the case of $v_n = 0$, all eigenvalues, except the first one, $\lambda_1 = -c$, are nonnegative; thus, only the first characteristic variable must be specified. The constraint $v_n = 0$ is nothing than a free slip condition, imposing that there is no convective flux through the boundary.

### 1.4.2 Discontinuous Galerkin Finite Elements

In order to apply the DG method the computational domain $\Omega$ is partitioned into $\mathrm{n_{el}}$ disjoint subdomains with characteristic size $h$, that is

$$\bar{\Omega} = \bigcup_{e=1}^{\mathrm{n_{el}}} \bar{\Omega}_e \quad \text{such that} \quad \Omega_e \cap \Omega_l = \emptyset \quad \text{for } e \neq l \tag{1.5}$$

Also, define a vector-valued function space of discontinuous, piecewise-polynomials of degree $p$,

$$\mathcal{V}^h = \{v \in \mathcal{L}^2(\Omega) |\, v_{|_{\Omega_e}} \in \mathcal{P}^p(\Omega_e), \forall \Omega_e\}$$

where $\mathcal{P}^p(\Omega_e)$ is the space of polynomial functions of degree at most $p$ in $\Omega_e$.

Consider test functions $\mathbf{W} \in [\mathcal{V}^h]^{\mathrm{n_{comp}}}$. Recall that $\mathrm{n_{comp}}$ is the number of components of the solution $\mathbf{U}$. For Euler equations, $\mathrm{n_{comp}} = \mathrm{n_{sd}} + 2$. An approximation $\mathbf{U}_h \in [\mathcal{V}^h]^{\mathrm{n_{comp}}}$ to the solution of (1.2) is obtained if, for all $\mathbf{W} \in [\mathcal{V}^h]^{\mathrm{n_{comp}}}$,

$$\int_{\Omega_e} \mathbf{W}^T \frac{\partial \mathbf{U}_h}{\partial t}\, d\Omega - \int_{\Omega_e} \frac{\partial \mathbf{W}^T}{\partial x_k} \mathbf{F}_k(\mathbf{U}_h)\, d\Omega + \int_{\partial\Omega_e} \mathbf{W}^T \mathbf{F}_{\mathbf{n}_e}(\mathbf{U}_h)\, d\Gamma = 0,$$

where $\mathbf{n}_e$ is the outward unit normal vector on $\partial\Omega_e$ and $\mathbf{F}_{\mathbf{n}_e}(\mathbf{U}_h)$ is the normal flux function, defined as

$$\mathbf{F}_{\mathbf{n}_e}(\mathbf{U}_h) = \mathbf{F}_k(\mathbf{U}_h) n_k \quad k = 1, \ldots, \mathrm{n_{sd}} \tag{1.6}$$

with $n_k$ the $k$th component of $\mathbf{n}_e$. In these expressions Einstein summation convention is used. As standard in DG methods, in order to take into account the discontinuous nature of the approximation, the flux function $\mathbf{F}(\mathbf{U}_h)$ is not uniquely defined in the interfaces $\partial\Omega_e$ that are not boundaries ($\partial\Omega_e \neq \partial\Omega$). The normal flux function at the elements boundary is replaced by a numerical one, $\widehat{\mathbf{F}}_{\mathbf{n}_e}(\mathbf{U}_h, \mathbf{U}_h^{\mathrm{out}})$ , which is evaluated in terms of the solution in the current element $\Omega_e$, $\mathbf{U}_h$, and the solution at neighboring elements,

$$\mathbf{U}_h^{\mathrm{out}} = \lim_{\epsilon \to 0^+} \mathbf{U}_h(\boldsymbol{x} + \epsilon \mathbf{n}_e) \quad \text{for } \boldsymbol{x} \in \partial\Omega_e$$

This interface flux function, $\widehat{\mathbf{F}}_{\mathbf{n}_e}$ is determined using any of the standard *Riemann solvers* of Finite Volume methods, see Toro (1999). Introducing the numerical flux, the resulting DG formulation for element $\Omega_e$ becomes: find $\mathbf{U}_h \in [\mathcal{V}^h]^{\mathrm{n_{comp}}}$ such that,

for all $\mathbf{W} \in [\mathcal{V}^h]^{\mathrm{n_{comp}}}$ ,

$$\int_{\Omega_e} \mathbf{W}^T \frac{\partial \mathbf{U}_h}{\partial t}\, d\Omega - \int_{\Omega_e} \frac{\partial \mathbf{W}^T}{\partial x_k} \mathbf{F}_k(\mathbf{U}_h)\, d\Omega + \int_{\partial\Omega_e} \mathbf{W}^T \widehat{\mathbf{F}}_{\mathbf{n}_e}(\mathbf{U}_h, \mathbf{U}_h^{\mathrm{out}})\, d\Gamma = 0, \qquad (1.7)$$

Boundary conditions are enforced weakly, by appropriately setting $\widehat{\mathbf{F}}_{\mathbf{n}_e}$ when $\partial\Omega_e$ coincides with $\partial\Omega$. By assembling all the elemental contributions, this induces a system of ordinary differential equations (ODEs) of the form

$$\mathbf{M}\frac{d\boldsymbol{U}_h}{dt} + \mathbf{R}(\boldsymbol{U}_h) = \mathbf{0} \qquad (1.8)$$

where $\boldsymbol{U}_h$ is the vector of approximation coefficients, $\mathbf{M}$ is the mass matrix, which is block diagonal, and $\mathbf{R}(\boldsymbol{U}_h)$ is the discrete spatial residual vector. The ODE system (1.8) can be solved with any time integration scheme. For the examples presented in this thesis an explicit Runge-Kutta method is used, see Donea and Huerta (2003). The time-step is determined by the stability condition which limits the Courant number as follows

$$CFL = |\lambda_{\max}|\frac{\Delta t}{h} \leq \frac{1}{2p+1}$$

where $h$ is the element size and $p$ the degree of the functional approximation. The scalar value $\lambda_{\max}$ is the maximum eigenvalue of the Jacobi matrix of the flux, see factorization (1.3).

# Chapter 2

# A continuous-discontinuous DG method

In this chapter a novel shock-capturing technique for the Discontinuous Galerkin method is presented, see Casoni et al. (2011a). This is the first of the two methods presented in this thesis. The method is inspired in the Finite Volume technology, in the sense of possessing inherent stabilizing properties, but it also maintains the advantages of high-order methods.

The inherent structure of standard DG methods seems to suggest that they are specially adapted to capture shocks because of the numerical fluxes based on suitable Riemann solver, which, in practice, introduces some stabilization, see Chavent and Cockburn (1989). However, the usual numerical fluxes are not sufficient to stabilize the solution in the presence of shocks for large high-order elements.

Here, a new basis of shape functions is introduced. A new approximation space is defined in Section 2.1. In particular, the basis of shape functions, which is a convex combination between piecewise constant shape functions and continuous standard ones of Lagrange type, is defined in detail. This basis allows to switch from a piecewise constant to a continuous representation of the solution within each element. Many alternative representations are possible in order to define constant shape functions, see for instance the standard Finite Volume approaches by Godunov (1959) or the monograph by LeVeque (2002). Here, they are defined to ensure a conservative scheme (LeVeque (1992)). Here, they are defined such that a conservative scheme is ensured,

LeVeque (1992).

The exact form of the basis is governed by a discontinuity control parameter, which, in turn, depends linearly on a discontinuity sensor. Here the discontinuity sensor by Persson and Peraire (2006) is used. The sensor has been proven to be especially reliable for high-order approximations. Finally, numerical examples show the applicability and accuracy of the proposed method, enhancing the sub-cell resolution.

## 2.1 Definition of the approximating space

### 2.1.1 From continuous to discontinuous

Consider the general form of a system of hyperbolic conservation laws in two-space dimensions,

$$\frac{\partial \mathbf{U}}{\partial t} + \frac{\partial \mathbf{F}_k(\mathbf{U})}{\partial x_k} = \mathbf{0} \tag{2.1}$$

where $k$ ranges from 1 to $\mathrm{n_{sd}}$ (here, $\mathrm{n_{sd}} = 2$), $\mathbf{U}$ is the vector of conservation variables, and $\mathbf{F}_k(\mathbf{U})$ is the flux vector for each spatial dimension $x_k$. Recall the system of the compressible Euler equations defined in Chapter 1. A DG formulation is used for the discretization of the problem.

In the bounded domain $\Omega$, a partition of $\mathrm{n_{el}}$ disjoint elements $\bar{\Omega} = \bigcup_{e=1}^{\mathrm{n_{el}}} \bar{\Omega}_e$ is assumed, such that $\Omega_e \cap \Omega_f = \emptyset$ for $e \neq f$. Then, an element by element discontinuous approximation is considered. The strong form is multiplied by a vector of test functions $\mathbf{W} \in [\mathcal{P}^p(\Omega_e)]^{\mathrm{n_{comp}}}$, with $\mathcal{P}^p(\Omega_e)$ being the space of polynomials of total degree $\leq p$ defined over $\Omega_e$.

The resulting DG formulation for element $\Omega_e$ ($e = 1, \ldots, \mathrm{n_{el}}$) becomes find $\mathbf{U}^h \in [\mathcal{P}^p(\Omega_e)]^{\mathrm{n_{comp}}}$ such that, for all $\mathbf{W} \in [\mathcal{P}^p(\Omega_e)]^{\mathrm{n_{comp}}}$,

$$\int_{\Omega_e} \mathbf{W}^T \frac{\partial \mathbf{U}^h}{\partial t}\, d\Omega - \int_{\Omega_e} \frac{\partial \mathbf{W}}{\partial x_k}^T \mathbf{F}_k(\mathbf{U}^h)\, d\Omega + \int_{\partial\Omega_e} \mathbf{W}^T \hat{\mathbf{F}}_{\mathbf{n}_e}(\mathbf{U}^h, \mathbf{U}^h_{\mathrm{out}})\, d\Gamma = 0, \tag{2.2}$$

where $\mathbf{n}_e$ is the outward unit normal vector on $\partial\Omega_e$ and $\hat{\mathbf{F}}_{\mathbf{n}_e}(\mathbf{U}^h, \mathbf{U}^h_{\text{out}})$ is the normal flux function. See Section 1.4.2 in Chapter 1 for the details.

The solution $\mathbf{U}^h$ of equation (2.2) is sought in $[\mathcal{P}^p(\Omega_e)]^{\text{n}_{\text{comp}}}$ which is characterized by a complete basis of polynomials; that is,

$$\mathcal{P}^p(\Omega_e) = \text{span}\{N_1(\boldsymbol{x}), N_2(\boldsymbol{x}), \ldots, N_{\text{n}_{\text{en}}(p)}(\boldsymbol{x})\} \quad \text{for } \boldsymbol{x} \in \Omega_e$$

where $\text{n}_{\text{en}}(p)$ is the number of element nodes (i.e, the number of degrees of freedom for each element), which depends on the degree $p$ of the basis.

Here, in order to capture discontinuities, the polynomial space is modified. The new shape functions, $\bar{N}_i(\boldsymbol{x};\alpha)$ , are defined as a convex combination of standard polynomials, $N_i(\boldsymbol{x})$ , and a set of piecewise constant functions within each sub-cell of the element, $\phi_i(\boldsymbol{x})$ . That is, the approximation is now characterized by

$$\mathbf{U}^h = \sum_{i=1}^{\text{n}_{\text{en}}(p)} \bar{N}_i(\boldsymbol{x};\alpha)\, \mathbf{U}^h_i \quad \text{for } \boldsymbol{x} \in \Omega_e,$$

and the shape functions are defined as follows

$$\bar{N}_i(\boldsymbol{x};\alpha) := \alpha N_i(\boldsymbol{x}) + (1-\alpha)\phi_i(\boldsymbol{x}) \quad \text{for} \quad i = 1, \ldots, \text{n}_{\text{en}}(p) \tag{2.3}$$

where $\alpha \in [0,1]$ is a parameter that depends on the smoothness of the solution.

In order to determine the piecewise constant functions $\phi_i(\boldsymbol{x})$ each element $\Omega_e$ is arbitrarily partitioned into a set of $\text{n}_{\text{en}}(p)$ non-overlapping sub-cells

$$\bar{\Omega}_e = \bigcup_{k}^{\text{n}_{\text{en}}(p)} \bar{\Omega}^k_e \quad \text{such that} \quad \Omega^l_e \cap \Omega^m_e = \emptyset \text{ for } l \neq m$$

where each sub-cell $\Omega^k_e$ contains only one elemental node. Figure 2.1 depicts typical partitions for a first order and second order element. Notice that the cell interfaces form a non-structured mesh. Given the sub-cell partition, each function

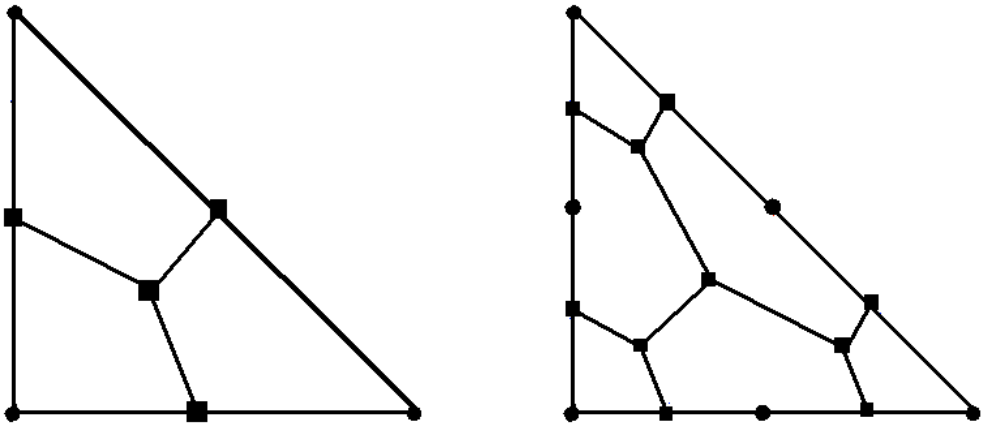

Figure 2.1: Cell partition of $\Omega_e$, $p = 1$ (left) and $p = 2$ (right). Circle marks correspond to node positions and square marks are the sub-cell vertices.

$\phi_i(\boldsymbol{x}) : \Omega_e \longrightarrow \mathbb{R}$ is defined as piecewise constant over each sub-cell. That is,

$$\forall \boldsymbol{x} \in \Omega_e \qquad \phi_i(\boldsymbol{x}) = \phi_i^k = \text{cst} \quad \text{if } \boldsymbol{x} \in \Omega_e^k, \quad \text{for } k = 1, \ldots, \mathrm{n_{en}}(p) \tag{2.4}$$

where $\phi_i^k$ are defined in the next subsection.

**Remark 2.1.** *The partition of $\Omega_e$ into control volumes is not unique. Here, a simple procedure is considered: given a triangulation of the element, obtained by joining its nodes, the centroid of each subtriangle and the midpoints of the edges form a set of $n_{en}(p)$ polygons such that each of them contains only one elemental node.*

A major advantage of DG methods is the intrinsic stabilization introduced by numerical fluxes, see for instance Chavent and Cockburn (1989) or Cockburn and Shu (2001). For values of $\alpha \in [0, 1[$ the proposed basis of approximation functions, namely

$$\text{span}\{\bar{N}_1(\boldsymbol{x}; \alpha), \bar{N}_2(\boldsymbol{x}; \alpha), \ldots, \bar{N}_{\mathrm{n_{en}}(p)}(\boldsymbol{x}; \alpha)\} \quad \text{for } \boldsymbol{x} \in \Omega_e,$$

introduces interelement discontinuities due to the piecewise constant contribution of each $\phi_i(\boldsymbol{x})$. Thus numerical fluxes are accounted for inside the elements and their

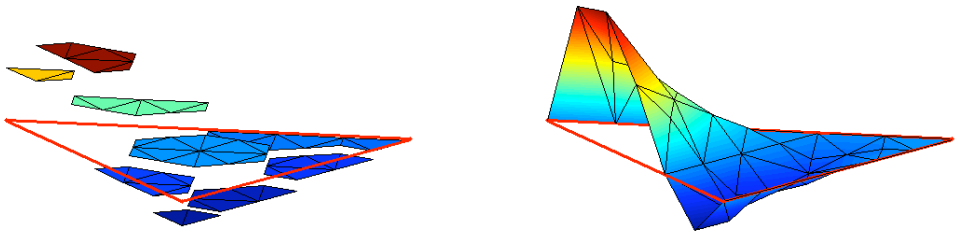

(a) $\alpha = 0$ (b) $\alpha = 1$

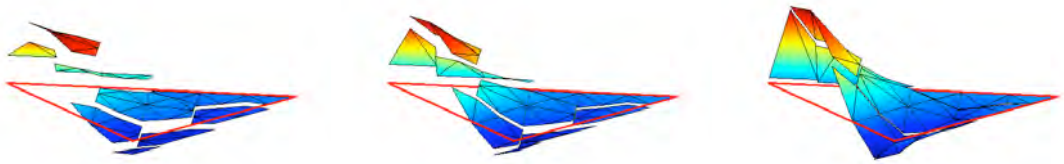

(c) $\alpha = 0.25$ (d) $\alpha = 0.5$ (e) $\alpha = 0.85$

Figure 2.2: Shape function of degree $p = 3$ for different values of $\alpha$.

influence on stability will preclude spurious oscillations. Obviously, the order of the approximation is reduced to one in the element when $\alpha \in [0, 1[$ and, as described below, the shock resolution is $\mathcal{O}(h/p)$. Whereas high-accuracy, of order $h^p$, is retained in the elements with $\alpha = 1$, which define the large majority of the domain as it will be shown in the examples.

Figure 2.2 shows a typical third order shape function $\bar{N}_i$ for different values of $\alpha$. The particular cases $\bar{N}_i = \phi_i$ and $\bar{N}_i = N_i$ correspond to Figures 2.2(a) and 2.2(b), respectively .

Parameter $\alpha$ can vary in space and time depending on the regularity of the solution. Consequently, although the number of degrees of freedom and the topology of the mesh is unchanged the interpolation is adapted (in space and time) to the smoothness of the solution by means of $\alpha$ and its influence in the approximation basis, see (2.3).

### 2.1.2 Piecewise constant sub-cell shape functions

In the limit case of $\alpha = 0$ the discontinuous functions $\phi_i$ induce a standard Finite Volume approach over the sub-cells van Leer (1979), LeVeque (2002) or Cueto-Felgueroso and Colominas (2008). Thus, conservation is also imposed for each sub-cell for any value of $\alpha$. Thus, to design functions $\phi_i$ standard zero-order reproducibility is imposed. Namely,

$$\sum_{i=1}^{\mathrm{n_{en}}(p)} \phi_i^k = 1 \quad \text{for each } k = 1, \ldots, \mathrm{n_{en}}(p). \tag{2.5}$$

Recalling that

$$\sum_{i=1}^{\mathrm{n_{en}}(p)} N_i(\boldsymbol{x}) = 1 \quad \forall \boldsymbol{x} \in \Omega_e,$$

equation (2.5) implies

$$\sum_{i=1}^{\mathrm{n_{en}}(p)} \bar{N}_i(\boldsymbol{x}; \alpha) = 1 \quad \forall \boldsymbol{x} \in \Omega_e \text{ and } \forall \alpha \in [0, 1].$$

There are several options to define $\phi_i^k$ in order to satisfy Eq. (2.5), but it is important to recall that piecewise discontinuous functions are sought. Thus, although $\phi_i^k = 1/\mathrm{n_{en}}(p)$ for all $k = 1, \ldots, \mathrm{n_{en}}(p)$ complies with Eq. (2.5), it is not valid. An obvious choice is to impose $\phi_i^k = \delta_{ik}$, but it is independent of the sub-cell size. Here, the following definition is imposed

$$\phi_i^k = \frac{1}{\mathrm{meas}(\Omega_e^k)} \int_{\Omega_e^k} N_i(\boldsymbol{x})\, d\Omega \quad \text{for every } i \text{ and } k = 1, \ldots, \mathrm{n_{en}}(p). \tag{2.6}$$

Note that with this definition the contribution to node $\boldsymbol{x}_i$ of the piecewise constant shape function $\phi_i(\boldsymbol{x})$ from sub-cell $\Omega_e^k$ is equivalent to the contribution of the standard shape function $N_i(\boldsymbol{x})$.

### 2.1.3 Construction of the basis functions

A major advantage of DG methods is their flexibility in modifying the approximation space element by element. In steady state problems such as the ones studied here, the value of $\alpha$ is adapted to adequately capture the different discontinuities in the solution. Moreover, in transient problems, also studied here, the parameter $\alpha$ adapts its value in space and in time to accurately capture strong variations of the solution. Thus without modifying the mesh topology, nor the number of degrees of freedom, nor the node position, nor the structure of the matrices, in a very simple manner (a linear variation) the space of approximations is adapted in space and time to the regularity of the solution.

It is clear from Eq. (2.3) that extreme values of $\alpha$ ($\alpha = 0$ or 1) give the well-known cases of a Finite Volume approximation and a standard continuous DG approximation, respectively. For intermediate values of $\alpha$, the shape functions introduce jumps of different magnitude across the subelement interfaces. The jump size on the sub-cell interface is controlled by $\alpha$. Thus, $\alpha$ allows to calibrate the amount of stabilization introduced by the Riemann solvers inside the element. Therefore, $\alpha$ is a function of a discontinuity sensor proposed by Persson and Peraire (2006) and briefly recall in multi-dimensions in the next section.

The parameter $\alpha$ can take many forms. The first simplest choice is to model it as a *switch* function. That is, $\alpha = 1$ if the discontinuity sensor does not detect a discontinuity and $\alpha = 0$ when a discontinuity is detected. Thus, functions $\bar{N}_i$ are prescribed to be either piecewise constant or smooth $p$th-order approximations. Despite the fact that this option combines perfectly a $p$th-order DG method with a Finite Volume approximation where needed, it is not proposed here. The discontinuity sensor used here is very accurate and efficient but it does not have the precision to switch drastically from DG to Finite Volumes. Moreover, Barth and Jespersen (1989) and Venkatakrishnan (1995) discuss the use of discontinuous functions can severely hamper the convergence of Euler and Navier-Stokes codes to steady state.

In fact, a linear variation is proposed. This improves convergence to steady state and also introduces a smooth transition between DG and Finite Volumes. In this

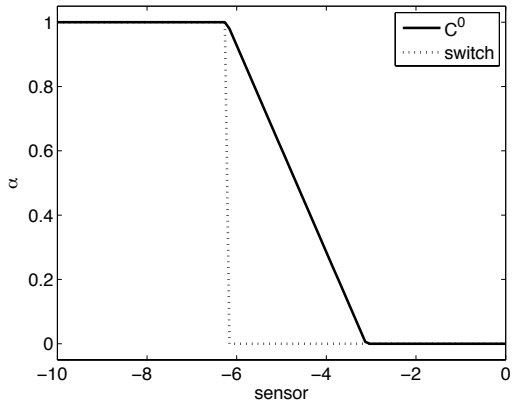


Figure 2.3: Variation of parameter $\alpha$ with the discontinuity sensor.

manner when the discontinuity sensor clearly detects a discontinuity $\alpha = 0$ and when the solution is clearly smooth $\alpha = 1$. In between a linear variation progressively introduces larger discontinuities. Note however, that a $p$th-order approximation is only recovered for values of $\alpha = 1$. Figure 2.3 shows both choices.

## 2.2 Discontinuity sensor

The discontinuity sensor defined element by element to determine the parameter $\alpha$, is proposed by Persson and Peraire (2006) and Nguyen et al. (2007). It only depends on a physical quantity, the Mach number appears to be a reliable sensing variable compared to other physical quantities like the entropy or density, as suggested by Persson and Peraire (2006) and Krivodonova (2007). Obviously, other choices are possible. It is an element-based projection leading to a single, scalar measure of the smoothness of the numerical approximation. This indicator is a non-linear operator $S^e(s) : \Omega_e \longrightarrow \mathbb{R}$, depending on the sensing variable $s$, which here is the Mach number, i.e. $s = M = \| \boldsymbol{v} \| / c$.

In order to determine a suitable sensor for discontinuities, the solution is written within each element in terms of a hierarchical family of orthonormal polynomials. In 1D, orthonormal Legendre polynomials are used, whereas in 2D, an orthonormal

Koornwinder (1992) basis is employed. For simplicity the sensor is first presented in 1D before it is generalized to higher dimensions. Let $\{P_i, i = 1, \ldots, p+1\}$ be the set of orthonormal Legendre polynomials of degree $p$. The sensing variable $s$ on a 1D element $\Omega_e$ is approximated with this basis as

$$s(x) = \sum_{i=1}^{\mathrm{n_{en}}(p)} s_i P_i(x).$$

A truncation of the same sensor on $\Omega_e$ to order $p-1$ in this hierarchical basis is given by

$$\hat{s}(x) = \sum_{i=1}^{\mathrm{n_{en}}(p-1)} s_i P_i(x).$$

For element $\Omega_e$, the following smoothness indicator is defined (in 1D),

$$S^e(s) = 2\log_{10}\big(\parallel s - \hat{s} \parallel_2 / \parallel s \parallel_2\big) \tag{2.7}$$

where $\| \cdot \|_2$ is the standard $L_2(\Omega_e)$ norm. Note that, in the above expression

$$(s - \hat{s}) \in \mathcal{P}^p(\Omega_e) \setminus \mathcal{P}^{p-1}(\Omega_e) \tag{2.8}$$

and it is a measure of the highest frequencies in the polynomial approximation; in fact, it only contains the higher-order terms of the expansion of $s(x)$.

In what follows the orthonormality of the basis is exploited to simplify Eq. (2.7) and to further obtain an expression generalizable to multiple dimensions. Note that because of the orthonormality of the Legendre polynomials, the $L_2(\Omega_e)$ norm of $s(x)$ becomes $\parallel s \parallel_2 = \sqrt{\mathbf{s}^T\mathbf{s}}$, where vector $\mathbf{s}$ is defined by the coefficients of the polynomial expansion, i.e. $\mathbf{s}^T = (s_1, \ldots, s_{\mathrm{n_{en}}(p)})$. Thus, given the hierarchy of the polynomial basis, Eq. (2.7) can be rewritten as

$$S^e(s) = \log_{10}\big(s^2_{\mathrm{n_{en}}(p)}/\mathbf{s}^T\mathbf{s}\big) \tag{2.9}$$

The discontinuity sensor in higher dimensions works analogously. The orthonormal Legendre basis is replaced by the orthonormal Koornwinder one. As noted previously, see (2.8), $(s-\hat{s})$ is the projection of the high-order approximation $s(\boldsymbol{x})$ on the space of monomials of degree equal to $p$. Thus Eq. (2.7), or equivalently the multidimensional generalization of (2.9), becomes

$$S^e(s) = \log_{10}\left(\mathbf{s}^T\mathbf{P}_{\mathrm{H}}\,\mathbf{s}/\mathbf{s}^T\mathbf{s}\right) \tag{2.10}$$

where $\mathbf{P}_{\mathrm{H}}$ is an orthogonal projection matrix onto the space of monomials of degree $p$. If the orthonormal Koornwinder basis is properly ordered

$$\mathbf{P}_{\mathrm{H}} = \mathrm{diag}(\overbrace{0\cdots 0}^{\mathrm{n_L}}\,\overbrace{1\cdots 1}^{\mathrm{n_H}}),$$

where $\mathrm{n_L}$ is the number of lower modes, i.e. the number of degrees of freedom for polynomials of degree $p-1$ (ex.: $\mathrm{n_L} = p(p+1)/2$ in 2D), and $\mathrm{n_H}$ is the number of remaining high order modes, i.e. the number of monomials of degree $p$ (ex.: $\mathrm{n_H} = p+1$ in 2D). See Remark 2.2 if, instead of an orthonormal basis, a more usual nodal basis is used.

This indicator, either Eq. (2.9) for the 1D case or Eq. (2.10) in multi-dimensions, treats higher-order solution as thought it were comprised of a sequence of Fourier modes. For smooth flows, the coefficients of increasing Fourier modes are expected to decay very quickly, according to $1/p^2$. However, a slower rate of decay indicates the presence of a non-smooth solution feature. This idea is strongly related to the error indicators used in spectral *hp*-methods, see Mavriplis (1994). Moreover, the strength of the discontinuity dictates the rate of decay of the expansion coefficients, see for instance Gottlieb and Hesthaven (2001). Figure 2.4 shows the decay rate of the expansion coefficients for functions a step function and a smooth one, namely: $f(\boldsymbol{x}) = \sin(x+y)$ for $(x,y) \in [-\pi,\pi]\times[-\pi,\pi]$.

In fact, the expected decay defines the threshold for non-smooth solutions. If the decay of consecutive orders is larger then $1/p^2$, i.e. if $S^e(s) > S_0 = -4\log_{10}(p)$, the

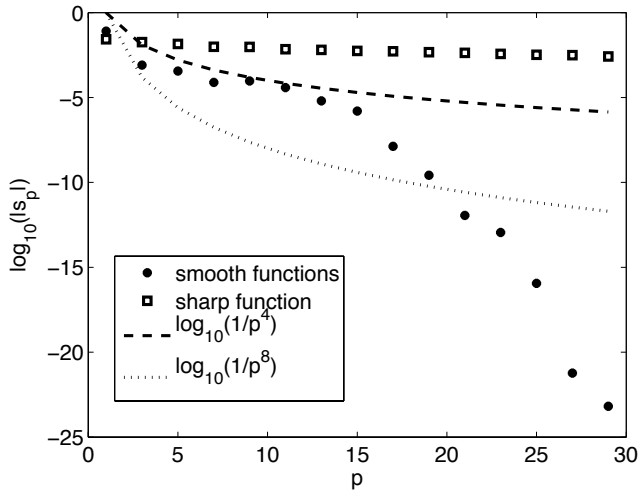


Figure 2.4: Decay rate of the expansion coefficients for a step and a smooth 2D functions and thresholds $S_1 = \log_{10}(1/p^8)$ and $S_0 = \log_{10}(1/p^4)$.

solution is assumed non-smooth and $\alpha = 0$. When the decay is clearly below the theoretical one, i.e. if $S^e(s) < S_1 = -4C\log_{10}(p)$, the solution is assumed smooth and $\alpha = 1$. When $C = 1$ a switch $\alpha$-function is used, see Figure 2.3. If a linear variation between $\alpha = 1$ and $\alpha = 0$ is sought $C$ is chosen larger than one. Since results are very robust for small variations of $C$, in practice, i.e. for the all examples shown, $C = 2$ is imposed with good results. These two thresholds are also depicted in Figure 2.4 .

Finally, it must be noticed, that this discontinuity sensor, originally proposed by Persson and Peraire (2006), has been found to be extremely reliable for the Euler equations and medium to high orders of approximation (i.e. $p \geq 2$).

**Remark 2.2.** *Nodal basis are usually implemented in computer codes (Lagrange polynomials). If this is the case, equation* (2.10) *is simply*

$$S^e(s) = \log_{10}\left(\frac{\mathbf{s}^T\mathbf{V}^{-T}\mathbf{P}_H\mathbf{V}^{-1}\mathbf{s}}{\mathbf{s}^T\mathbf{V}^{-T}\mathbf{V}^{-1}\mathbf{s}}\right),$$

*where* $\mathbf{V}$ *is the Vandermonde matrix whose inverse maps the Lagrange basis onto the orthonormal one. See Section 3.1 by Sevilla et al. (2008) and references therein for a*

*detailed discussion on these transformations.*

## 2.3 Numerical tests

This section presents several numerical examples of compressible flow for both, transonic and supersonic flow regimes as well as transient and steady-state problems. In order to assess the performance of the proposed methodology coarse meshes and high-order approximations are used. Moreover, the locality of this approach is also shown. All the tests are performed with triangular meshes and with an explicit Runge-Kutta time integration scheme. For steady-state solutions, the relative $L_2$ norm of the density residual is taken as a criterion to test convergence.

### 2.3.1 One-dimensional tests

#### The one-dimensional Burgers' equation

The classical non-linear inviscid Burgers' equation with periodic boundary conditions is first presented.

$$\begin{cases} u_t + f_x(u) = 0 & \text{in } [0,1],\ t > 0, \\ u(x,0) = \frac{1}{2} + \sin(2\pi x). \end{cases}$$

The solution of this problem forms a shock at time $t = 0.25$ that moves to the right. Solutions are computed over a uniform grid of 10 element and shown at time $t = 0.5$, when the shock is fully formed.

In order to analyze the diffusive effect of the piecewise constant shape functions the solution is computed setting $\alpha = 0$ in all the elements and with $\alpha$ varying between 0 and 1 as a function of the discontinuity sensor. Recall that shape functions with $\alpha < 1$ introduce jumps within the element. The complete basis of shape functions corresponding to $\alpha = 0$ for degree $p = 5$ is shown in Figure 2.5. Note that, the oscillating character of continuous standard shape functions is damped.

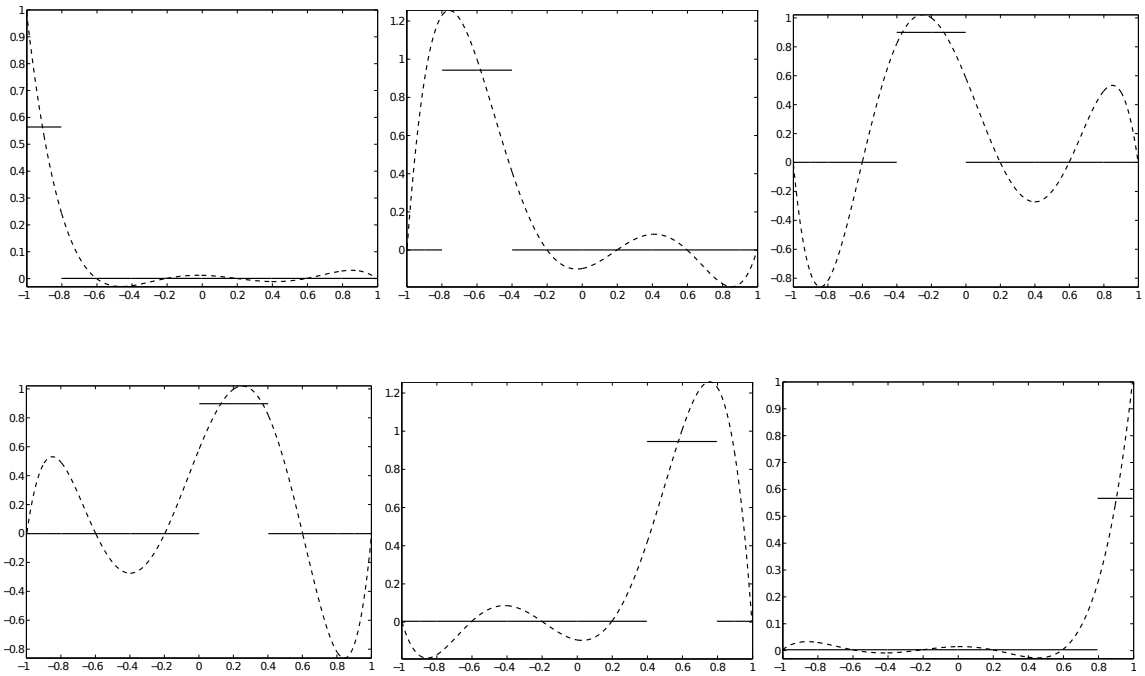

Figure 2.5: Fifth order shape functions for $\alpha = 1$ (dashed line) and $\alpha = 0$ (continuous line).

Figures 2.6 show a comparison between the approximations with $\alpha = 0$ and $\alpha$ variable, with degrees $p = 5$ (left) and $p = 10$ (right). The dissipative effect of the piecewise constant approximation is clearly enhanced not only along the shock front but also in the surrounding elements. It is especially highlighted the peak of the shock around $x = 0.7$, which decreases significantly. Moreover, the piecewise constant approximation also introduces an important dispersion error. This dispersion error is not sensitive to the number of subcells of the piecewise constant functions, since it is not reduced by increasing $p$ from 5 to 10. The value of parameter $\alpha$ within each element is also plotted in Figures 2.7 for each approximation. Notice that despite using a discontinuous basis in the element containing the shock, the solution is continuous within it, providing a smooth but sharp profile.

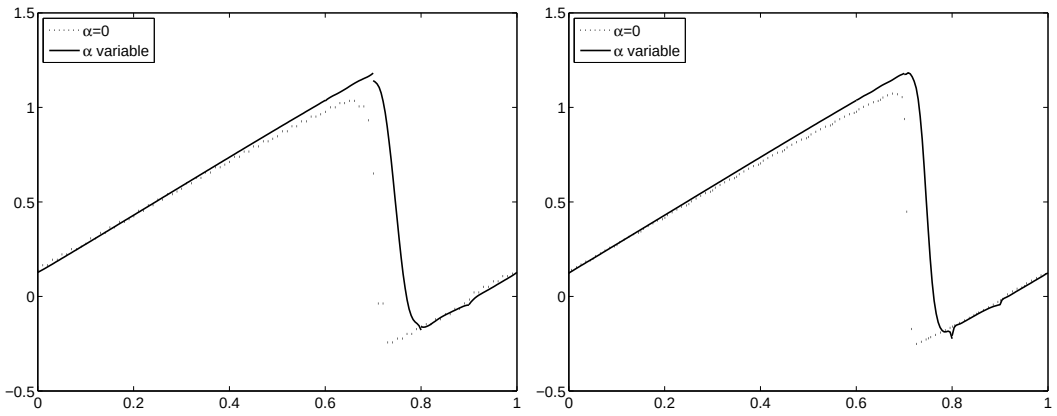


Figure 2.6: Burgers' equation at time $t = 0.5$ for degree $p = 5$ (left) and $p = 10$ (right).

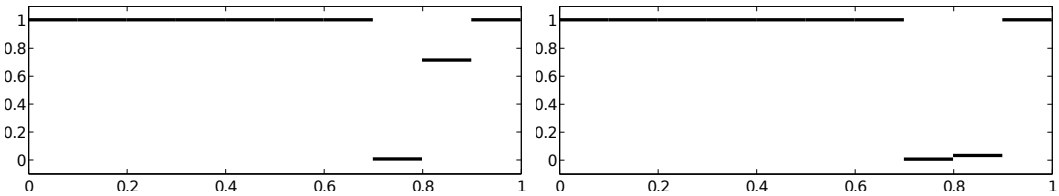

Figure 2.7: Value of $\alpha$ within each element.

### The shock tube problem

The classical shock tube problem proposed in Sod (1978), for which there exists an exact solution to the 1D Euler equations, is next proposed to validate the method. The problem involves a shock wave, a contact discontinuity and an expansion fan. The problem is solved in a 2D setting with a computational domain of dimensions $\Omega = ]0, 1[\times]0, 0.4[$. The following initial data are used:

| $0 < x_1 \leq 1/2$ | $1/2 < x_1 \leq 1$ |
|---|---|
| $\rho = 1.0$ | $\rho = 0.125$ |
| $\rho \boldsymbol{v} = \mathbf{0.0}$ | $\rho \boldsymbol{v} = \mathbf{0.0}$ |
| $\rho E = 2.5$ | $\rho E = 0.25$ |

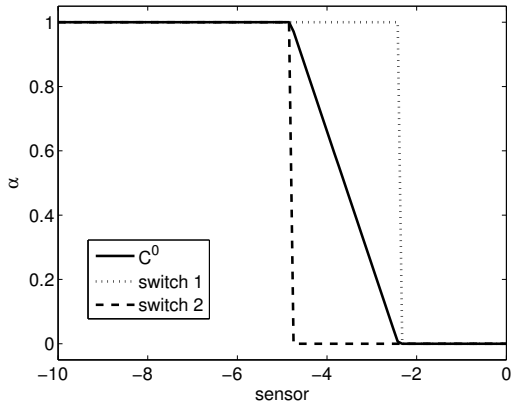


Figure 2.8: Shock tube problem, $\alpha$ functions tested.

The initial density and pressure difference are maintained by a diaphragm which is ruptured at $t = 0$. A uniform mesh with $p = 6$ and equilateral triangles of characteristic size $h = 1/10$ is used. As noted earlier, this is a coarse high-order mesh, which results in less degrees of freedom compared to other computations using linear elements of characteristic size as low as $h = 1/200$, see for instance Burbeau et al. (2001) or Krivodonova (2007).

The purpose of this example is to demonstrate applicability of this method in a transient problem and to show the advantages of the linear variation of parameter $\alpha$. The evolution of the solution is computed upto $t = 0.2$ when the shock wave, the contact discontinuity and the expansion fan are clearly developped. Note that in a transient problem, such as this example, the elements where $\alpha \neq 1$ evolve with time. Capturing the correct wave speeds shows a good performance of this technique. Moreover, this is done for three different choices of the variation of $\alpha$ with respect to the discontinuity sensor. Figure 2.8 shows the three different choices, namely, a linear variation between $S_0$ and $S_1$,

$$\alpha_0(S) = \begin{cases} 1 & \text{if } S < S_1, \\ (S_0 - S)/(S_0 - S_1) & \text{if } S_1 \leq S < S_0, \\ 0 & \text{if } S_0 \leq S, \end{cases} \tag{2.11}$$

and two switch functions,

$$\alpha_1(S) = \begin{cases} 1 & \text{if } S < S_0, \\ 0 & \text{if } S_0 \leq S, \end{cases} \text{ and } \alpha_2(S) = \begin{cases} 1 & \text{if } S < S_1, \\ 0 & \text{if } S_1 \leq S. \end{cases} \tag{2.12}$$

To analyze the results density and pressure are shown along a section following the flow direction (i.e. projecting the solution on the plane $x_2$ and the corresponding variable). Figures 2.9 to 2.11 show the results for the different choices of the $\alpha$-function. Velocity and energy results produce similar conclusions.

These figures show that the position of the flow discontinuities is well predicted in the three cases. Nevertheless, the $\alpha_2$ switch, see Eq. (2.12), clearly introduces excessive numerical diffusion, see Figure 2.11. Whereas oscillations in Figure 2.10 clearly indicate that the $\alpha_1$ switch, on the contrary, is under-diffusive. These oscillations are more obvious in the $x_1$ component of the velocity, see Figure 2.12.

In order to better compare the impact of the approaches on the solution, Figure 2.13 displays the maximum local error for the continuous $\alpha$-function and the switch 2 (that is, the more restrictive) for density (left) and velocity (right). Errors for switch 1 are not computed because of the lack of physical meaning of the solution. Errors for the rest of the variables have the same behavior. As expected, the error obtained with the continuous approach of $\alpha$ is smaller in all the domain. Let's just enhance the peak around $x = 0.9$ in the velocity profile, consequence of the excessive smearing in the shock wave. For a detailed error analysis between the different switches, see Casoni et al. (2011b).

In summary, imposing piecewise constant approximations when the decay in the last polynomial order is not below $1/p^4$, introduces excessive numerical diffusion. While oscillations are present when a $p$-th order continuous approximation is assumed if the decay is just $1/p^2$ or larger. The linear variation determined by $\alpha_0$, see Eq. (2.11), induces accurate results as shown in Figure 2.9. It is important to recall in that these solutions are obtained with a coarse ($h = 1/10$) high-order ($p = 6$) mesh.

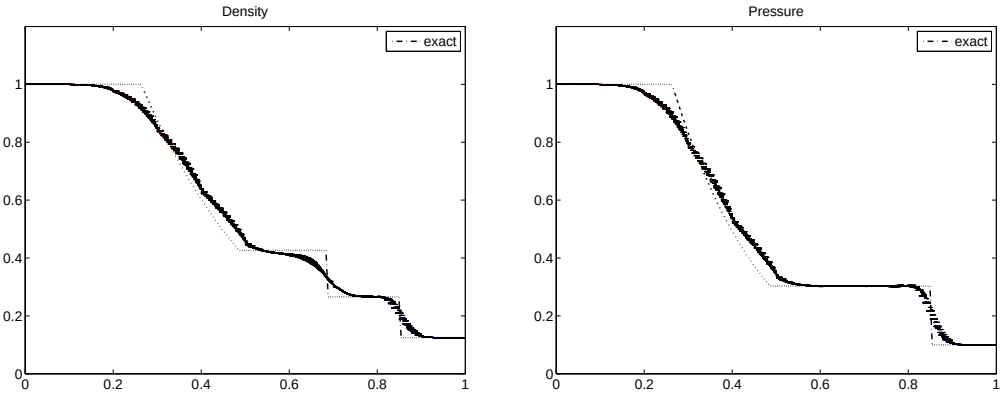


Figure 2.9: Shock tube profiles for $\alpha_0$.

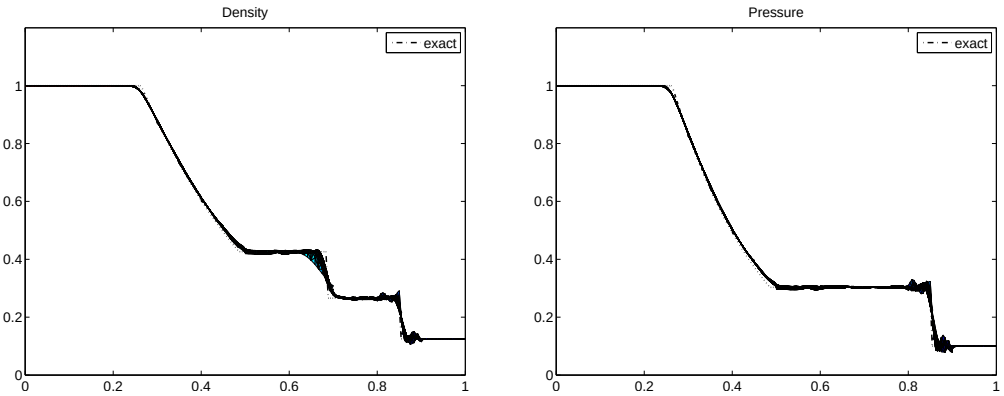


Figure 2.10: Shock tube profiles for the first switch: $\alpha_1$.

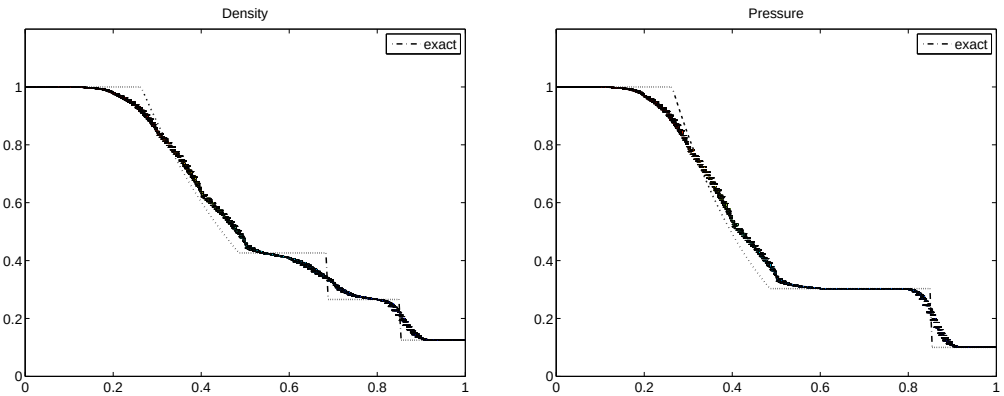


Figure 2.11: Shock tube profiles for the second switch: $\alpha_2$.

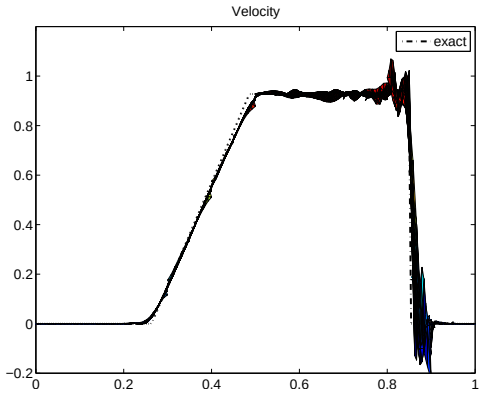


Figure 2.12: Shock tube $v_1$ profile for the first switch: $\alpha_1$.

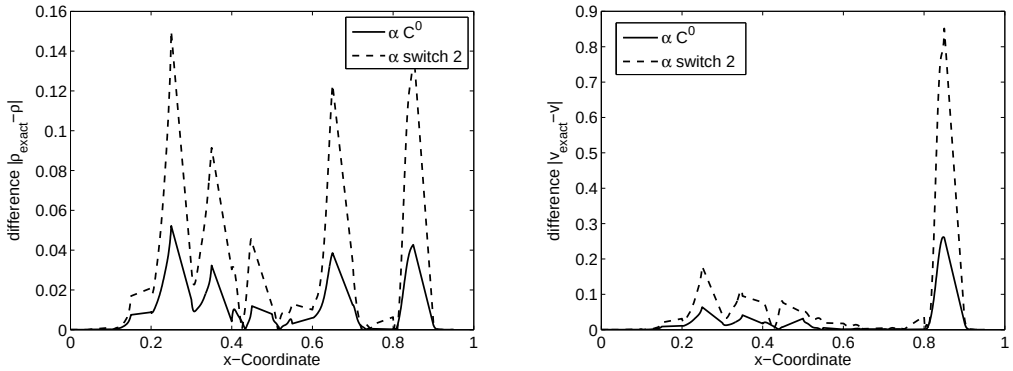


Figure 2.13: Shock tube maximum errors of the density (left) and velocity (right), between the continuous approach of $\alpha$ and the restrictive switch.

### 2.3.2 Multi-dimensional problems

#### Supersonic flow past a bump

This is a well-known benchmark test for steady-state simulation at different Mach numbers, see for instance Moukalled and Darwish (2001), Dolejší (2004) or Luo et al. (2007). It consists of inviscid flow in a channel with a 4% thick circular bump on the bottom. The channel is 3 units length and 1 unit height. The bump is located in the middle of the channel with chord length equal to 1. Inflow boundary condition is applied on the left, and outflow boundary condition on the right. At the top and bottom of the domain, solid wall boundary conditions are considered. The inlet Mach

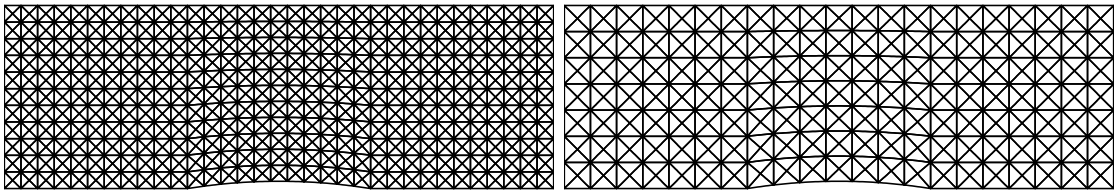

Figure 2.14: Supersonic flow past a bump with $M = 1.4$: computational meshes. On the right, a fine mesh of 1 452 elements and on the left a coarse one of 588 elements.

number is $M = 1.4$. In this case the steady-state solution is characterized by two stagnation points and a change in the direction of the shock due to the reflexion on the right boundary.

Common approaches use FV schemes combined with an adaptive unstructured mesh refinement (Moukalled and Darwish (2001)). Here, in order to show the applicability of the proposed methodology, high-order approximations with relative coarse, uniform and structured meshes are used. The first approximation is computed over a fine computational mesh of 1 452 elements and degree $p = 3$ (total number of degrees of freedom –dof– 58 080) and the second one is computed over a coarse mesh of 588 elements with degree $p = 5$ (total number of dof 49 392). Both meshes are depicted in Figure 2.14.

Figures 2.15 and 2.16 depict the Mach number obtained with both discretizations, respectively. Qualitatively, the solutions are similar, showing stable approximations with sharp shock profiles free of spurious oscillations. A detail of the oblique shock behind the duct is also shown in order to show that shocks are captured essentially inside one element, with independence of the mesh geometry. This is specially relevant for the fifth order approximation, where the element size doubles the size of the third order mesh and the shock is not aligned with edges. Moreover, in this case, it is clear that the shock width is far more thinner than the element size.

In order to compare the different solutions in more detail, an horizontal section along $y = 0.4$ is shown in Figure 2.17. The solutions for $p = 3$ and $p = 5$ are also compared with a linear approximation on a very fine mesh. The linear mesh requires 14 000 elements, i.e. triple number of degrees of freedom, to obtain similar accuracy of the $p = 5$ mesh. The comparison reveals that a sharper profile is obtained

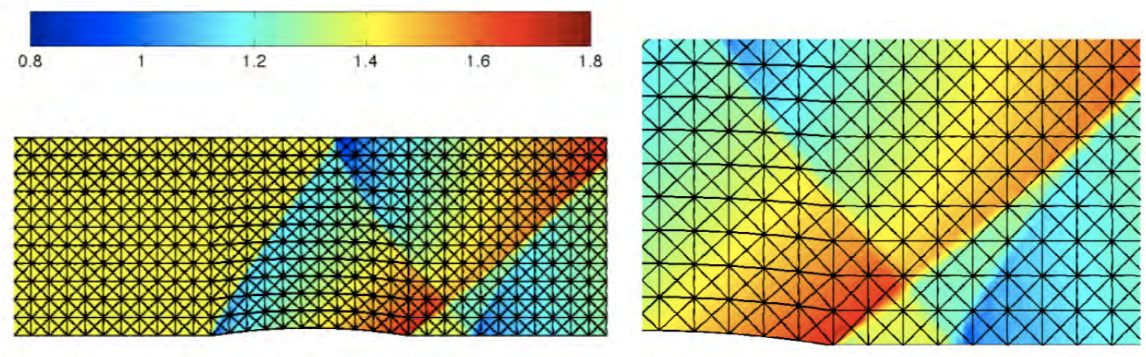


Figure 2.15: Supersonic flow past a bump with $M = 1.4$: Mach number for $p = 3$ and 1 452 elements.

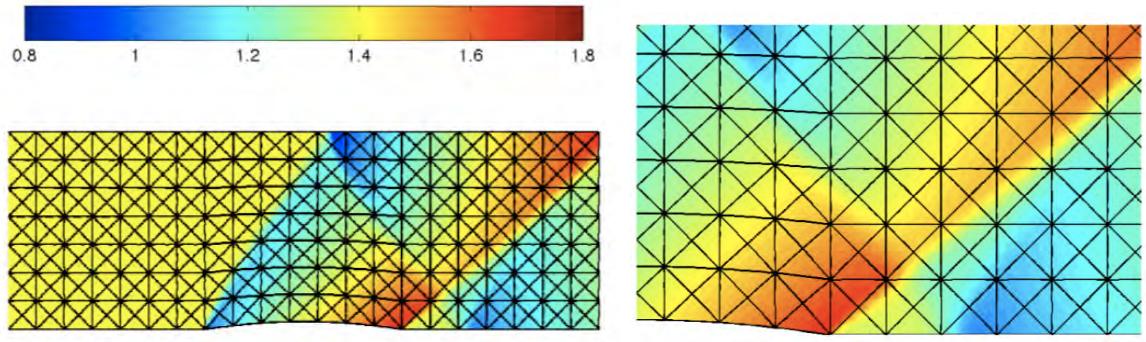


Figure 2.16: Supersonic flow past a bump with $M = 1.4$: Mach number for $p = 5$ and 588 elements.

with the high-order solution of degree $p = 5$ and a coarse mesh than with the low-order one of $p = 3$ and fine mesh. Hence, using large elements and increasing the degree of approximation (not the number of degrees of freedom) accuracy is improved. Compared to other high-order techniques that also use coarse meshes, see for instance Premasuthan et al. (2010), the present approximation is able to obtain accurate results with uniform coarse meshes and less degrees of freedom, avoiding adaptativity of the mesh along the shock regions.

The distribution of parameter $\alpha$ at steady-state is shown in Figure 2.18 . Elements in blue correspond to $\alpha \neq 1$ and consequently elements where accuracy is reduced

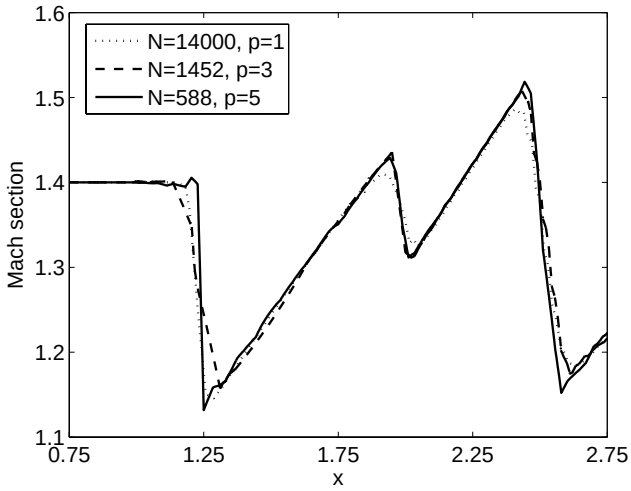


Figure 2.17: Supersonic flow past a bump with $M = 1.4$: distribution of the Mach number along section $y = 0.4$.

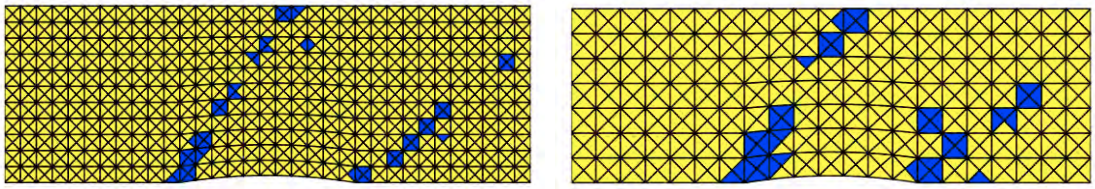

Figure 2.18: Supersonic flow past a bump with $M = 1.4$: distribution of $\alpha$ for $p = 3$ and 1 452 elements (left) and $p = 5$ and 588 elements, yellow for $\alpha = 1$, blue for $0 < \alpha < 1$, and red for $\alpha = 0$

to order $h/p$. Note that these areas coincide, as expected, with sharp gradients in Mach number; that is, along the shock front. Notice that in contrast with standard approaches, the mesh is not modified neither refined along the shock region. Hence, the computational cost of recomputing the mesh within each iteration is avoided.

### Transonic flow in a converging-diverging nozzle

The converging-diverging nozzle is another standard benchmark test involving flow of inviscid non-heat-conducting air through a nozzle, see Anderson (1984) or Demirdzic et al. (1993). Here the 2D (planar) case proposed by Hartmann and Houston (2002)

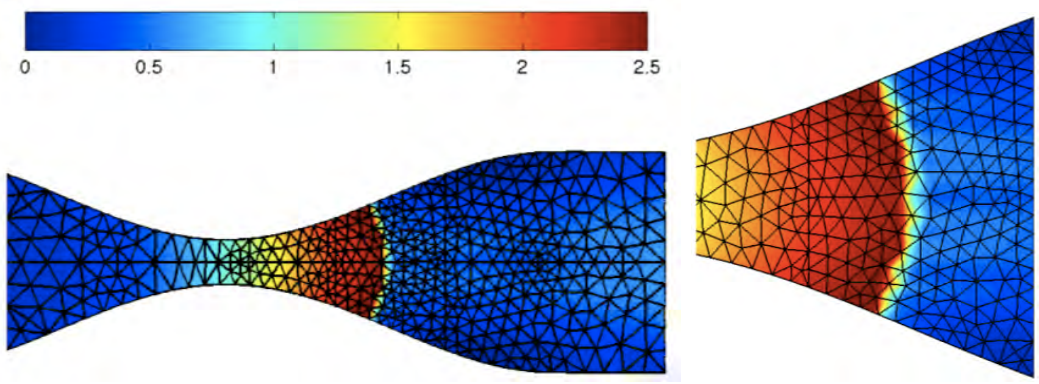


Figure 2.19: Transonic nozzle: Mach number for a solution computed with $p = 3$ and a mesh of 916 elements. Detail of the shock on the right.

is considered. The computational domain $\Omega$ is in $]0, 3[\times]0, 1[$ and presents a variable section defined by a sinusoidal profile. Inviscid wall boundary conditions are imposed on the lower and upper edges of the domain. Inflow conditions impose the Mach number, $M = 0.5$, density and pressure, both equal to 1. At the supersonic outflow a pressure condition, the ratio between the stagnation and the free-stream pressure is prescribed equal to 0.67. Under these circumstances supersonic flow with a normal shock in the diffusing section is created.

Two different discretizations are considered: 916 elements and degree $p = 3$ (36 640 dof) and 278 elements with degree $p = 5$ (23 352 dof). Note that both discretizations use uniform meshes and a reduced number of degrees of freedom, for instance an order of magnitude lower than the mesh used by Hartmann and Houston (2002).

Figure 2.19 depicts Mach number for the third order approximation. In spite of the coarse approximation and the uniform mesh steady state is reached and the shock is captured avoiding spurious oscillations. However, a closer look reveals some lack of accuracy: the shock loses its typical bow shape and it is influenced by the discretization.

Obviously, mesh adaption near the shock would alleviate this inaccuracies. However, high-order approaches may also be an alternative thanks to the discontinuous basis proposed here. In fact, the solution with $p = 5$, shown in Figure 2.20, presents accurate results and a clearly defined bow shock independent of the discretization.

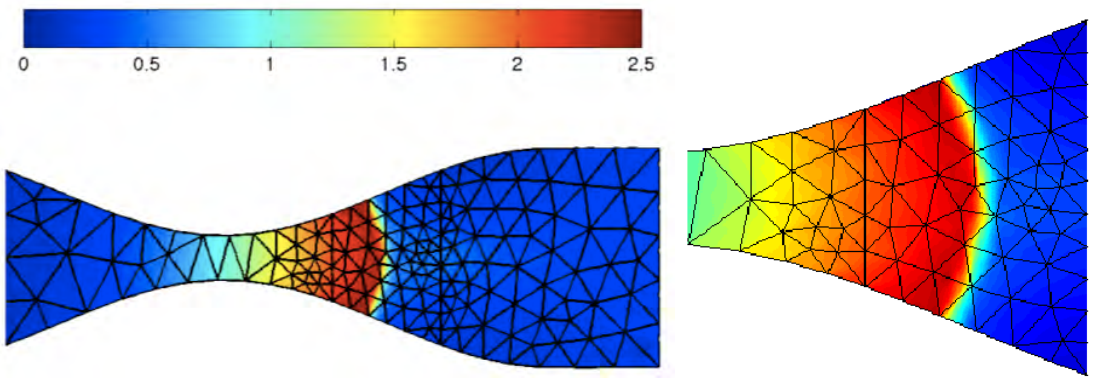


Figure 2.20: Transonic nozzle: Mach number for a solution computed with $p = 5$ and a mesh of 278 elements. Detail of the shock on the right.

The shock is clearly captured inside the elements and with thickness less than the element size. Note also, that the higher order approach requires a reduced number of dof.

In Figures 2.21 and 2.22 the Mach number distributions along an horizontal (at $y = 0.5$) and vertical (at $x = 2$) section are depicted. Moreover, the high-order solutions are further compared with a FV computation. In order to do a fair comparison a uniform mesh is also employed for the FV case. More than twice the number of dof has been used (19 200 elements, i.e. 76 800 number of dof) and as shown they are not sufficient. Figure 2.21 clearly shows that the $p = 5$ solution, which is the one with lower dof, presents the sharpest shock. The FV and $p = 3$ solutions are rather coincident, but the $p = 3$ solution presents a small oscillation behind the shock. However, Figure 2.22 reveals interesting conclusions. The FV approximation results in non-physical variations of the Mach number, although the transversal shock profile was smooth, the $p = 3$ solution has lost its symmetry, and the $p = 5$ results are the expected ones.

### The forward-facing step problem

A challenging test for computing unsteady shock waves is the numerical simulation of a wind tunnel with a flat faced step, originally introduced by Emery (1968) to compare

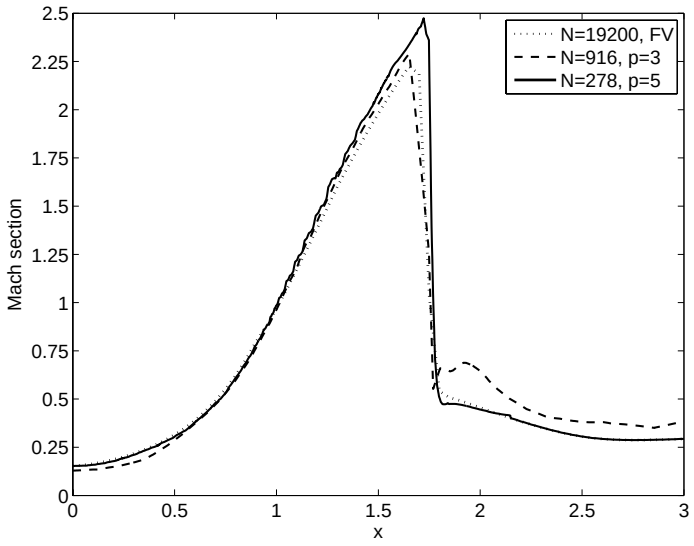


Figure 2.21: Transonic nozzle: Mach number profiles along $y = 0.5$ for $p = 0, 3$ and 5

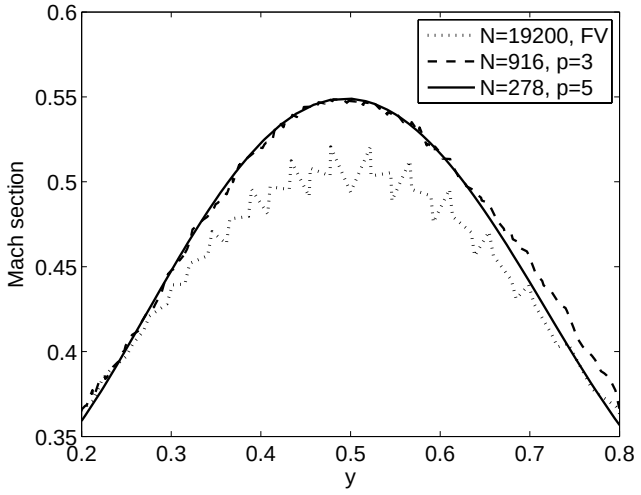


Figure 2.22: Transonic nozzle: Mach number profiles along $x = 2$ for $p = 0, 3$ and 5

several difference schemes in classical fluid dynamics. It is now a standard numerical benchmark used by several authors, see among others Woodward and Colella (1984), Holden et al. (1999), Cockburn and Shu (2001), Zhu et al. (2008) or Xu and Liu (2011). The problem under consideration is a Mach 3 flow in a wind tunnel of 3 units long and 1 unit wide. The step is 0.2 units high and it is located at 0.6 units from

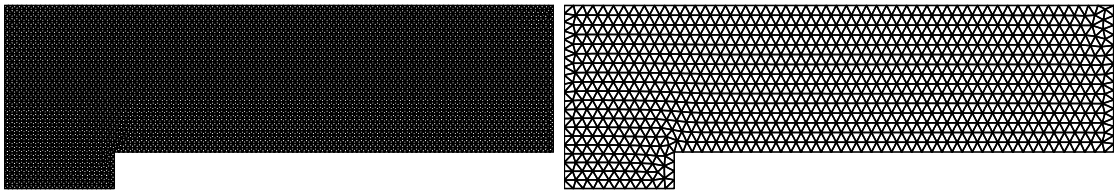

Figure 2.23: Forward-facing step with Mach 3: computational meshes of 10 677 elements (left) and 1 728 elements (rigth).

the left-hand end of the tunnel. Initially the tunnel is filled with a gas, with adiabatic coefficient $\gamma = 1.4$, which everywhere has density $\rho = 1.4$, pressure $p = 1$, and velocity $\boldsymbol{v} = (3, 0)^T$. Solutions are shown at time $t = 4$ of the computations, where a special and complicated shock configuration is showed.

An inflow boundary condition is applied at the left end of the computational domain and outflow boundary condition at the right end. Along the walls of the tunnel, as well as on the boundary marked by the step, inviscid wall boundary conditions are applied. The corner of the step is the center of a rarefaction fan and, thus, a singular point of the flow. It is well known that this singularity leads to an erroneous entropy layer at the downstream bottom wall, as well as spurious Mach oscillations at the top wall next to the Mach stem. Unlike Woodward and Colella (1984) and many other references, here the scheme is not modified near the corner, neither the mesh is refined. This will allow to see the influence of large elements with high-order approximation in the entropy layer. Note that results are very reasonable although no modification near this corner is introduced.

Two meshes with different approximations are compared: a very fine mesh of 10 677 elements and $p = 2$, and a coarse mesh of 1 728 elements and degree $p = 6$. Both meshes are depicted in Figure 2.23. Notice that both are uniform with no special refinement around the corner or at the shocks.

Figure 2.24 shows the computed density profiles at time $t = 4$ for both meshes. The location and shape of the shocks are consistent in both computations. The shocks and the rarefaction fan, which is created around the corner, are well-captured without generating relevant noise. This is specially remarkable around the upper slip line from the triple point and behind the Mach stem, compared to other results, for instance

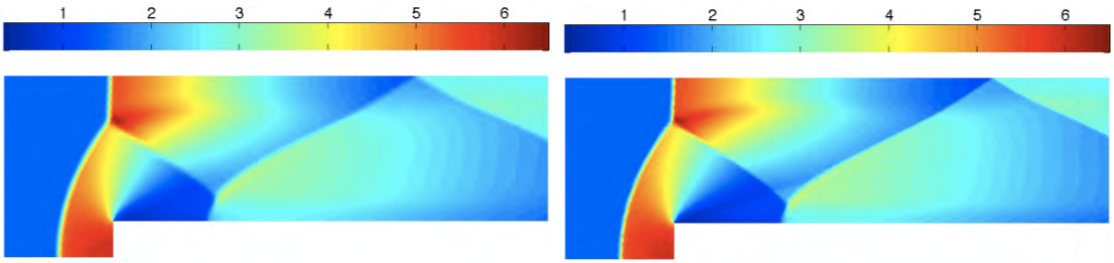


Figure 2.24: Forward-facing step with Mach 3: density profile for $p = 2$ and 10 677 elements (left) and $p = 6$ and 1 728 elements (rigth).

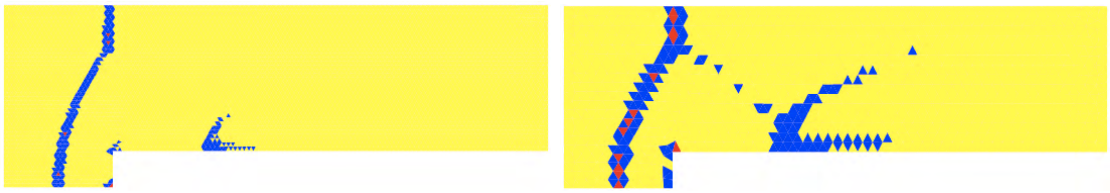

Figure 2.25: Forward-facing step with Mach 3: $\alpha$ values for $p = 2$ and 10 677 elements (left) and $p = 6$ and 1 728 elements (rigth), yellow for $\alpha = 1$, blue for $0 < \alpha < 1$, and red for $\alpha = 0$.

Cockburn and Shu (2001) or Zhu et al. (2008). The contact discontinuity arising from the triple point is slightly better resolved with the high-order approximation despite less degrees of freedom are involved.

Figure 2.25 shows the map of $\alpha$, which controls the discontinuities inside each element, for each element and both approximations. Again, the results are consistent: the detection is aligned with the major shocks and clearly identifies the sharp $\lambda$-type shock. Since the elements in the $p = 6$ mesh are coarser than the $p = 2$ mesh, the thickness of the detected region is bigger for the high-order approximation. This fact is consequence of the element-by-element behavior of the sensor and the parameter $\alpha$. Nevertheless, as shown next, this does not imply that the shock width is larger for the coarser mesh ($p = 6$).

In order to better compare both solutions as well as their accuracy, density along $y = 0.2$ is shown in Figure 2.26. Both cases locate the bow shock at $x = 0.3$ approximately. However, a sharper front is observed for $p = 6$; that is, although the $p = 6$ has a coarser mesh size the shock profile is thinner. Moreover, the $p = 6$ solution

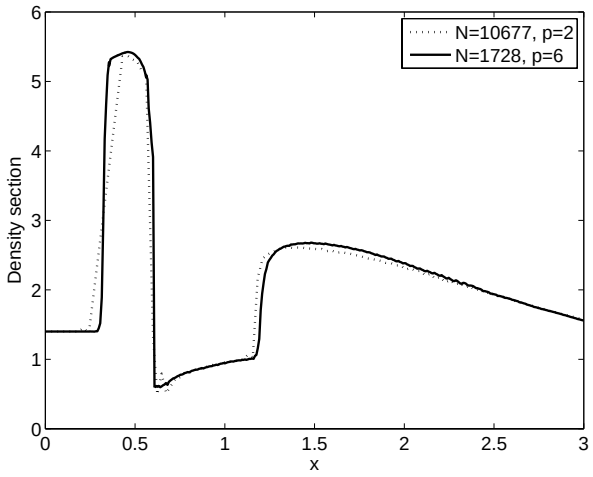


Figure 2.26: Forward-facing step with Mach 3: section along $y = 0.2$ of the density profile.

does not present oscillations, while the $p = 2$ shows small oscillations near the outflow boundary and bigger ones just after the shock, at $x = 0.6$, where the density drops by a factor of 5.

The entropy production in the vicinity of the step corner, caused by the singular point is a clear indicator of the noise introduced by the scheme and also its ability to deal with singularities. In order to obtain more accurate solutions (with less entropy production) several authors use adaptive refinement near the singular point, see Cockburn and Shu (2001) or Holden et al. (1999). Other alternatives are possible using a specific numerical treatment on the singular point, see Woodward and Colella (1984). Here, in order to see the influence of high-order approaches no adaptivity or entropy manipulation is done. The adiabatic constant, $A = p/\rho^{\gamma}$ , which is a function of entropy, is plotted in Figure 2.27. Note that the amount of entropy generation along the downstream boundary is not excessive and moreover that it is drastically reduced for $p = 6$.

To get a better inside in the performance of the proposed method, solutions with a sequence of four uniform meshes, shown in Figure 2.28, are computed with the same order of approximation, $p = 4$. Figure 2.29 shows density along $y = 0.2$. Obviously,

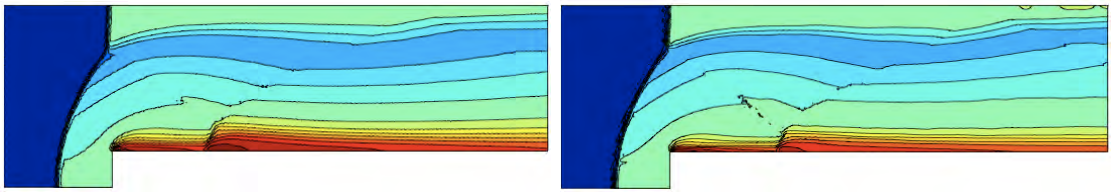

Figure 2.27: Forward-facing step with Mach 3: contours of adiabatic constant $A = p/\rho^\gamma$ for $p = 2$ and 10 677 elements (left) and $p = 6$ and 1 728 elements (rigth).

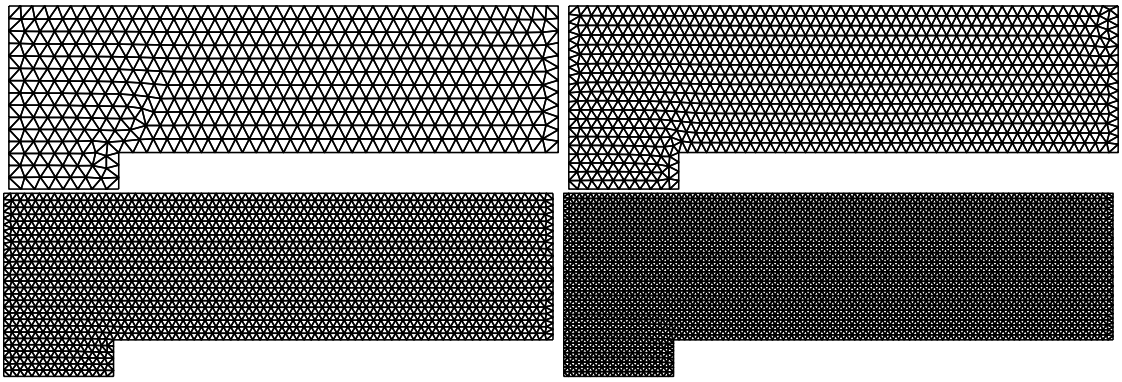

Figure 2.28: Forward-facing step with Mach 3: computational meshes. From left to right and top to bottom: 915, 1 728, 3 457 and 6 286 elements.

accuracy improves as the mesh is refined and a sharper shock is obtained with finer meshes. Nevertheless, even for the coarse mesh results are reasonable. But it is important to note that results converge as the mesh is refined.

### Supersonic NACA0012

The next test case is the inviscid solution of a NACA 0012 airfoil with a freestream Mach number of $M = 1.2$ at an angle of attach $\beta = 0°$. The inflow is specified by the total temperature, total pressure and flow angle and the outflow is specified to be the atmospheric static pressure. A fourth order approximation, $p = 4$, is performed over an unstructured mesh of 450 elements, with only 14 elements describing the airfoil surface. The mesh is depicted in Figure 2.30.

The Mach number profile is shown in Figure 2.31 (left). A detail around the airfoil is also shown with the mesh (right) in order to enhance sub-cell resolution. Note that

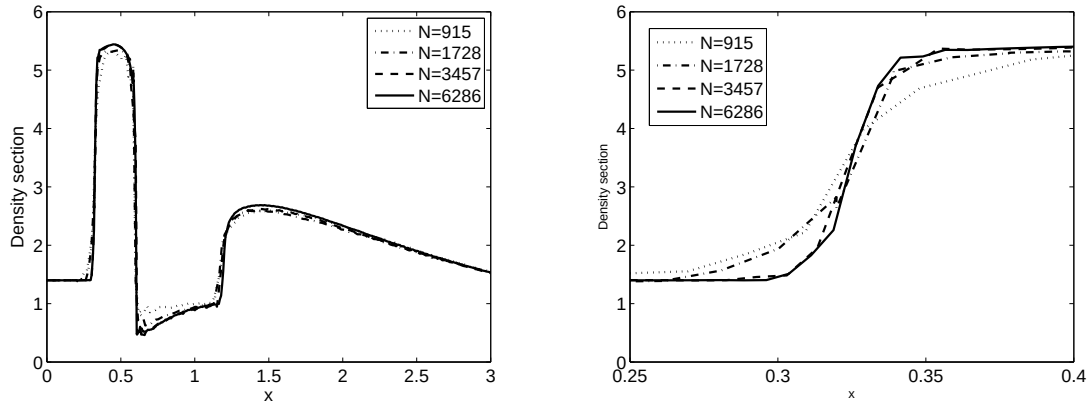


Figure 2.29: Forward-facing step with Mach 3: section along $y = 0.2$ of the density profile and detail of the first shock.

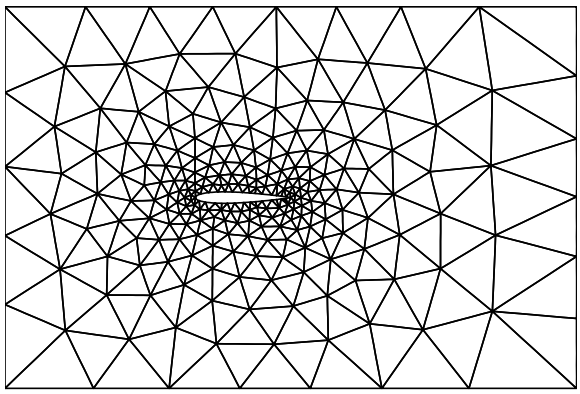

Figure 2.30: Supersonic flow past a NACA 0012 airfoil: computational mesh of 450 elements.

a very coarse mesh (except at the tip of the airfoil) is used, and any h-adaptation procedure around the shock has been applied. Although the coarseness of the mesh (compare with other approaches that use meshes of two orders of magnitude bigger, see for instance Arias et al. (2007)), the shock is well-resolved within a single element.

Figure 2.32 depicts the distribution of parameter $\alpha$. The sensor remains inactive in almost the whole domain, in contrast with other methods, where not only the elements containing the shock are detected, but also their neighbors, see Persson and Peraire (2006) and Nogueira et al. (2009). Notice that only at the tip of the airfoil

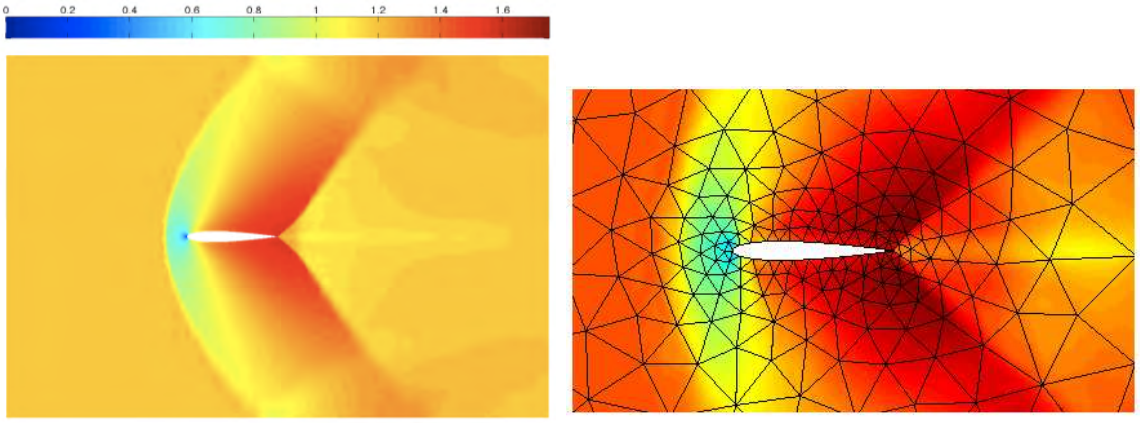


Figure 2.31: Supersonic flow past a NACA 0012 airfoil: Mach number for $p = 4$ and 450 elements.

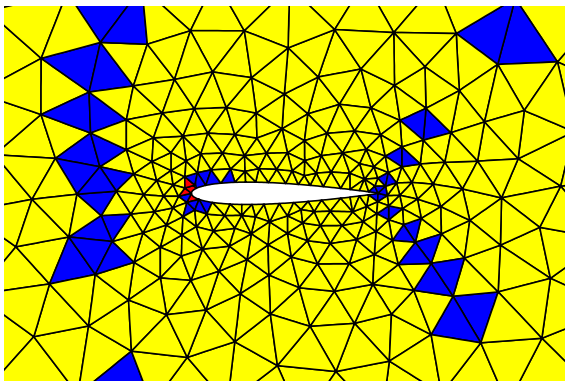

Figure 2.32: Supersonic flow past a NACA 0012 airfoil: distribution of $\alpha$, yellow for $\alpha = 1$, blue for $0 < \alpha < 1$ and red for $\alpha = 0$

.

$\alpha$ takes the limit value equal to 0 (that is, piecewise constant shape functions within each sub-cell), since that point is an stagnation point.

Since no analytical solution is available, solution with a very refined mesh and the Finite Volume method is also presented in order to validate the results. A mesh of 46 131 elements (i.e, 184 524 total number of dof) is used. Note that the number of degrees of freedom with the $p = 4$ and 450 elements was only 27 000. A detail of the tip and the tail of the airfoil is plotted in Figure 2.33. The shock is well-resolved

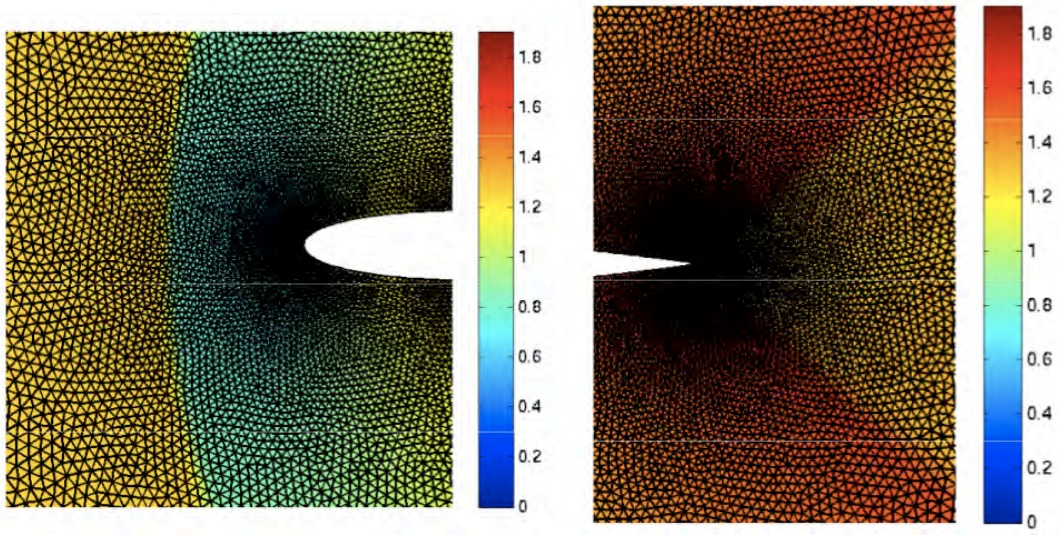


Figure 2.33: Supersonic flow past a NACA 0012 airfoil: Mach number detail on the tip and on the tail of the airfoil, for FV approximation.

.

but it is specially highlighted the extremely smaller element size required in order to achieve high accuracy in the shock regions.

Finally, the pressure coefficient along the surface of the airfoil is shown in Figure 2.34. This coefficient is a reliable measure to validate the accuracy of the method. Both shapes are in good agreement except at the center of the airfoil where the DG method slightly loses the curvature.

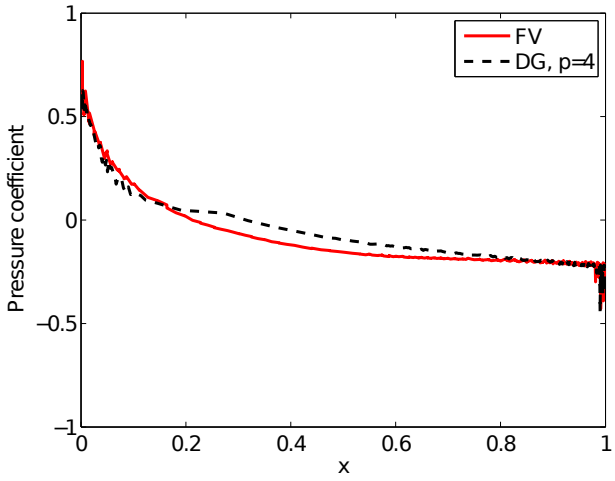


Figure 2.34: Supersonic flow past a NACA 0012 airfoil: pressure coefficient along the airfoil.

# Chapter 3

# The artificial diffusion method

Two shock-capturing approaches for Discontinuous Galerkin methods have been explored in this thesis: the continuous-discontinuous shape function approach, introduced in Chapter 2, and a high-order artificial diffusion method. This chapter describes the artificial diffusion approach, first developed for the one-dimensional case by Casoni et al. (2009) and later extended to higher dimensions.

Early methods for the numerical treatment of shocks and other flow discontinuities consist on adding dissipation to near sharp solution gradients to obtain stable solutions. The goal of this technique is to produce a local smoothing of the solutions by introducing a suitable amount of artificial diffusion. However, reincorporating the relevant physics of dissipation (Cockburn (2001)) in nonlinear hyperbolic conservation is not trivial. That is, the inherent difficulties in determining where and how much viscosity must be introduced to avoid oscillations without causing unnecessary smearing have deterred the extensive use of this approach.

Limiting techniques have emerged as an alternative for stabilizing high-order DG approximations, for instance, Runge-Kutta Discontinuous Galerkin (RKDG) methods, see Cockburn and Shu (2001). They are a special class of explicit RK schemes, see for instance Shu (1988); Shu and Osher (1988) and Gottlieb et al. (2001), that combine with approximate Riemann solvers and nonlinear operators to satisfy stability.

Here, the extensive experience in limiting techniques is used to define an artificial diffusion method. The introduction of dissipation in the equation does not hinder the

use of high-order and implicit schemes, in contrast with RKDG methods. Introducing an artificial viscosity that scales with the DG resolution length scales, $h/p$, makes the shock width also scale in the same manner. In this chapter an highly accurate artificial diffusion method is presented. The viscosity scales like $h^k$ for some $1 \leq k \leq p$, which in general is smaller than $h/p$, as numerical tests consistently show. The necessary background regarding limiting techniques is explained in Appendix A.

The introduction of artificial viscosity term requires the discretization of second order derivatives with DG methods. Here, for simplicity, the Local Discontinuous Galerkin (LDG) approach by Cockburn and Shu (1998a) is used, but other methods can also be employed, see for instance Peraire and Persson (2008). Particular formulation for the one-dimensional case, applied to a scalar hyperbolic conservation law with artificial viscosity, is exposed in this chapter. The method is complemented with the general formulation and technical details in Appendix B.

Shock width is directly related to the resolution length scale of the mesh. Keeping $h$ fixed, the higher the degree of the approximation, the thinner the shock. However, for very large elements, where the real shock width is far more thinner than the element size, the introduction of constant viscosity within the element results in an oversized viscosity footprint, which, in turn, doesn't make any qualitative improvement to the solution, as Barter and Darmolfal (2007) shows. To overcome this shortcoming and exploit sub-cell resolution, an extension of the artificial viscosity to sub-cells is proposed. The extension is focused on the sub-cell detection of the shock. Thus piecewise constant viscosity within regular partitions of the element can be defined, reducing the total area of viscosity amplitude.

The extension of the artificial diffusion to two-dimensions in triangular meshes is presented in Section 3.2. In contrast with the one-dimensional approach, multi-dimensional diffusion can no longer rely on slope limiters, since the extension of slope limiters in triangular meshes doesn't ensure high-order reconstructions, see for instance Cockburn and Shu (1998b) or Burbeau et al. (2001). The contribution of the procedure here presented is inspired by the computation of multi-dimensional limiters for rectangular elements, see for instance the extension by Biswas et al. (1994), where

the one-dimensional limiter is applied over each cartesian direction. Here, three characteristic directions on the triangle are defined and the solution is projected over each one of them in order to apply the one-dimensional artificial diffusion. In the following sections the formulation for the one-dimensional and two-dimensional artificial viscosity is developed, the main properties are highlighted and a couple of numerical tests for the scalar convection equation and for the Euler equations of gas dynamics are presented in order to illustrate the applicability of the method.

A particular problem of interest is the transport of solute through an homogeneous and highly adsorbent media. This problem is modeled with a convection-diffusion equation, which also includes a reaction term. The equation is coupled with a system of ODEs, giving rise to a possibly highly nonlinear PDE. Relationships between the physical parameters involved lead to different behaviors of the equation, depending on the dominant term. Under this rationale, shocks may arise from three different situations. First, because of a purely convective equation that transports sharp fronts. Second, because of non-linear convection terms. And third, because of the presence of reaction terms, which may be also highly non-linear. Standard discretization methods are not able to deal with these situations and hence, simplifications of the model are required in order to simulate all the cases, obtaining physically acceptable solutions, see Pérez-Foguet and Huerta (2005).

Here, artificial diffusion method is proposed to overcome these difficulties. The applicability of the method for problems involving discontinuities and shocks of different nature is hence demonstrated, avoiding the use of simplified formulations of the adsorption model. Consequently, an extensive analysis on adsorption modeling can be developed. This issue is addressed in detail in Appendix D, following the work started by Pérez-Foguet and Huerta (2005).

## 3.1 One-dimensional artificial viscosity

### 3.1.1 The Basics of LDG in 1D

Consider a scalar conservation law

$$u_t + f_x(u) = 0, \qquad x \in ]0,1[,\ t > 0 \tag{3.1}$$

and introduce a dissipative term, the artificial viscosity, of the form

$$u_t + f_x(u) - (\varepsilon(u)u_x)_x = 0, \qquad x \in ]0,1[,\ t > 0. \tag{3.2}$$

Here, $\varepsilon(u)$ is a non-negative quantity which models the artificial diffusion as a non-linear coefficient depending on the solution $u$. Notice that adding viscosity to the original equations introduces second order derivatives, which require special attention in discontinuous approximations. Several methods have been proposed to deal with this situation; here, the Local Discontinuous Galerkin method (LDG) by Cockburn and Shu (1998a) has been used.

In order to apply the LDG method, eq. (3.2) is written as a system of first order hyperbolic equations, typical of mixed methods

$$u_t + f_x(u) - \sigma_x = 0, \qquad x \in ]0,1[,\ t > 0 \tag{3.3a}$$

$$\sigma - \varepsilon(u)u_x = 0, \qquad x \in ]0,1[. \tag{3.3b}$$

where the auxiliary variable $\sigma$ has been introduced. In order to simplify the developments and following Cockburn and Shu (1998a) the new variable $g(u) = \int^u \varepsilon(s)\,ds$ is introduced, directly relate to $\sigma$; note, that using Leibniz rule it is easily demonstrated that $\sigma = g_x(u)$.

Let $\{I_e\}_{e=1,\ldots,\mathrm{n_{el}}}$ with $I_e = ]x_e, x_{e+1}[$ be a partition of the interval $]0,1[$ into $\mathrm{n_{el}}$ subintervals (or elements), with $0 = x_1 < x_2 < \cdots < x_{\mathrm{n_{el}}+1} = 1$. The weak formulation of

problem (3.3) is

$$\int_{I_e} u_t v\,dx - \int_{I_e} \big(f(u)-\sigma\big)v_x\,dx + \big[\hat{f}_{e+1}v(x_{e+1}^-) - \hat{f}_e v(x_e^+)\big] - \big[\hat{\sigma}_{e+1}v(x_{e+1}^-) - \hat{\sigma}_e v(x_e^+)\big] = 0 \tag{3.4a}$$

$$\int_{I_e} \sigma\tau\,dx + \int_{I_e} g(u)\tau_x\,dx - \big[\hat{g}_{e+1}\tau(x_{e+1}^-) - \hat{g}_e\tau(x_e^+)\big] = 0 \tag{3.4b}$$

for every element $e = 1, \ldots, \mathrm{n_{el}}$ and $t > 0$.

As standard in DG methods, the nonlinear flux $f(u)$ has been replaced by numerical one $\hat{f} = \hat{f}(u)$ which it is typically chosen as the Roe or Lax-Friedrichs flux. For implementation details see Cockburn and Shu (2001). There are two other fluxes due to LDG methods, $\hat{\sigma}$ and $\hat{g}$, which can be seen as approximations of the numerical traces of $\sigma$ and $g(u)$ on the boundaries. Standard numerical fluxes are used here, see Cockburn and Shu (1998a). Note that at interfaces the following notation is used:

$$x_e^{\pm} = \lim_{\epsilon \longrightarrow 0} x_e \pm \epsilon$$

It is usual to assume $\varepsilon(u)$ constant element by element, see Persson and Peraire (2006). Here the same assumption is used and, thus, for element $e$, $g(u) = \varepsilon_e u$; that is, eq. (3.4b) becomes

$$\int_{I_e} \sigma\tau\,dx + \int_{I_e} \varepsilon_e u\tau_x\,dx - \varepsilon_e\big[\hat{u}_{e+1}\tau(x_{e+1}^-) - \hat{u}_e\tau(x_e^+)\big] = 0$$

**Remark 3.1.** *Other assumptions for the distribution of $\varepsilon(u)$ are possible. In particular, assuming continuous $\varepsilon(u)$ precludes incoherences in* (3.2) *due to a discontinuous diffusion. For instance, assuming that only one shock is present per element an attractive numerical diffusion can be*

$$\varepsilon(u) = C\Big[1 - \tanh^2\Big(\frac{u-\Delta/2}{\nu}\Big)\Big],\ \textit{i.e.}\ g(u) = C\nu\tanh\Big(\frac{u-\Delta/2}{\nu}\Big),$$

*where $\Delta$ is the average of $u$ at left and right of the shock. Note that $\nu$ localizes more or less the artificial diffusion around the area where $u = \Delta/2$.*

### 3.1.2 Proposed approach for the artificial diffusion

The computation of the amount of artificial viscosity is performed combining the ideas of slope limiters and shock-capturing methods. The popular RKDG method (Cockburn and Shu (2001)) and the generalization of the classical slope limiter (Cockburn and Shu (1989)), $\Lambda\Pi_h$ , proposed by Biswas et al. (1994) provide a frame of reference for the present work. The objective of this section is, first, to briefly describe the construction of RKDG method, and second, to explain in detail how to compute the amount of artificial diffusion to introduce in (3.2).

#### RKDG methods

RKDG methods provide stable and high-order accurate schemes for nonlinear convection-dominated problems. The DG space discretization, the special strong stability preserving Runge-Kutta time discretizations (SSP-RK time discretizations) and the generalized slope limiters $\Lambda\Pi_h$ are intertwined just in the right way to achieve nonlinear stability. Note that $h$ is a characteristic measure of the elements.

Consider the conservation law (3.1) and approximate $-f_x(u)$ by a DG space discretization. A system of ordinary differential equations of the form $u_t = L(u)$ is obtained. The Total Variation Dimininish RK (TVD RK) time discretization scheme introduced by Shu (1988) is used to integrate the ODE system in time. Let $\{t^n\}_{n=0,\ldots,N}$ be a partition of $[0, T]$. The general form for an $m$-stage scheme reads as:

- Set $u^0 = \Lambda\Pi_h(u_0)$, where $u_0$ is the initial data for (3.1).
- For $n = 0, \ldots, N-1$ compute $u^{n+1}$ from $u^n$ as:
  - Set $u^{(0)} = u^n$

– For $\ell = 1, \ldots, m$ compute the intermediate functions:

$$u^{(\ell)} = \Lambda\Pi_h(u^{n+k_\ell}), \quad u^{n+k_\ell} = \sum_{i=0}^{\ell-1} \alpha_{\ell i} w^{\ell i}, \quad w^{\ell i} = u^{(i)} + \frac{\beta_{\ell i}}{\alpha_{\ell i}} L(u^{(i)})$$

- Set $u^{n+1} = u^{(m)}$

where the coefficients $\alpha_{\ell i}$ and $\beta_{\ell i}$ must satisfy typical RK conditions. This is the general form of the RKDG methods. They are stable under a CFL condition, see Cockburn and Shu (2001), in the seminorm $|\cdot|_{\mathrm{TV}}$ . That is, $|\bar{u}^{n+1}|_{\mathrm{TV}} \leq |\bar{u}^n|_{\mathrm{TV}}$ where $|\bar{u}|_{\mathrm{TV}} = \sum_e |\bar{u}_{e+1} - \bar{u}_e|$, with $\bar{u}$ being the average of $u$ in the element.

Notice that limiting techniques are implemented in two steps for each stage of the RKDG scheme. First, the conservation law (3.1) is solved, and second, the limiting operator $\Lambda\Pi_h$ is applied.

Assuming time integration under enough regularity, the weak formulation for the $k_\ell-$stage can also be symbolically written as

$$\begin{aligned} \int_{I_e} u^{n+k_\ell} v \, dx = \int_{I_e} u^n v \, dx + \\ \int_{t^n}^{t^{n+k_\ell}} \Big\{ \int_{I_e} f(u) v_x \, dx - \big[ \hat{f}_{e+1} v(x_{e+1}^-) - \hat{f}_e v(x_e^+) \big] \Big\} dt \end{aligned} \tag{3.5a}$$

and the limiting step is then applied

$$u^{(\ell)} = \Lambda\Pi_h\big(u^{n+k_\ell}\big) \tag{3.5b}$$

for all $e = 1, \ldots, \mathrm{n_{el}}$ and $t > 0$.

### The nonlinear limiting operator

Slope limiting techniques rely on the construction of a nonlinear local projection operator $\Lambda\Pi_h$ whose aim is to enforce nonlinear stability of the approximate solution.

For simplicity the approximate solution is expanded in terms of orthogonal Legendre polynomial, within each element $I_e$ (for all $e = 1, \ldots, \mathrm{n_{el}}$) the approximation of $u$ may be written as

$$u^e(x,t) = \sum_{i=0}^{p} c_i^e(t)\ P_i(x) \tag{3.6}$$

where the $P_i$ are the Legendre polynomials, normalized such that $P_i(1) = 1$, and the degrees of freedom $c_i^e$ are the so called modal coefficients.

Biswas et al. (1994) define a high-order slope limiter relying on the TVDM version of the generalized one proposed by Cockburn and Shu (1989), which is designed for linear approximations, i.e. $p = 1$. It is explained in detail in Appendix A. The idea is to limit the solution by limiting its coefficients. Beginning with the coefficient associated with the highest polynomial degree (i.e. for $i = p, p-1, \ldots, 1$), the coefficient $c_i^e$ of (3.6) is replaced by

$$\tilde{c}_i^e = \mathrm{minmod}\big(c_i^e, (c_{i-1}^{e+1} - c_{i-1}^e)/(2i-1), (c_{i-1}^e - c_{i-1}^{e-1})/(2i-1)\big),$$

with the usual definition of minmod function, see Appendix A for details. The limiter is active when $\tilde{c}_i^e \neq c_i^e$ for any $i$. Thus, the reconstructed coefficient $\tilde{c}_i^e$ limits $c_i^e$, which, in the absence of discontinuities, is proportional to the $i$th derivative of the approximation. Obviously, to preclude spurious oscillations higher order derivatives are limited first. The reconstructed solution has typically the following structure

$$\Lambda\Pi_h(u^e)(x,t) = \sum_{i=0}^{k} c_i^e(t)\ P_i(x) + \sum_{i=k+1}^{p} \tilde{c}_i^e(t)\ P_i(x). \tag{3.7}$$

A major improvement of this reconstruction is that rarely $k$ is as low as 0, which is the default value for the limiter proposed by Cockburn and Shu (1989).

In the next section the proposed artificial viscosity approach is presented. Note that, the superscript $^e$ indicating the element number is dropped to simplify the presentation. The nonlinear convection-diffusion equation, see (3.2), is solved instead of applying slope limiters to the numerical solution of the nonlinear hyperbolic equation,

see (3.1). The heuristics behind the construction of approximate Riemann solvers and slope limiters described by Cockburn (2001) are the guiding lines to determine an explicit expression for the artificial diffusion term. A relation between the artificial viscosity $\varepsilon(u)$ in (3.2) and the limited solution, see (3.7), of (3.1) is established.

### Artificial diffusion

Denote by $u^\varepsilon$ the exact solution of (3.2). The weak form of this convection-diffusion equation is

$$\int_{I_e} u_t^\varepsilon v\,dx - \int_{I_e} (f(u^\varepsilon) - \varepsilon(u^\varepsilon)u_x^\varepsilon)v_x\,dx + \big[(f(u^\varepsilon) - \varepsilon(u^\varepsilon)u_x^\varepsilon)v\big]_{x_e}^{x_{e+1}} = 0 \tag{3.8}$$

where the same partition proposed in Section 3.1.1 is used.

It is well known, see for instance LeVeque (1992) or Cockburn (2001), that for physical reasons, the correct solution, called the entropy solution is obtained when viscosity tends to zero, that is $\varepsilon \to 0$. Therefore the entropy solution at a given instant $t$ is defined by

$$\int_{I_e} uv\,dx = \lim_{\varepsilon\to 0}\int_{I_e} u^\varepsilon v\,dx$$

and analogously the numerical flux, typical of DG methods, is

$$\hat{f}_e = \lim_{\varepsilon\to 0}\big[f(u^\varepsilon(x_e,t)) - \varepsilon(u^\varepsilon)u_x^\varepsilon(x_e,t)\big]. \tag{3.9}$$

Taking the limit as $\varepsilon$ goes to zero in (3.8) and following the procedures developed by Cockburn (2001) the following weak formulation is obtained:

$$\int_{I_e} u_t v\,dx - \int_{I_e} f(u)\,v_x\,dx + \big[\hat{f}_{e+1}\,v(x_{e+1}^-) - \hat{f}_e\,v(x_e^+)\big] + \int_{I_e} \hat{\varepsilon}(u)\,u_x v_x\,dx = 0 \tag{3.10}$$

where the last term in (3.8) has been replaced by $\big[\hat{f}_{e+1}\,v(x_{e+1}^-) - \hat{f}_e\,v(x_e^+)\big]$. The term

containing the artificial viscosity coefficient $\hat{\varepsilon}(u)$ is the so-called *shock-capturing term*, and it is determined in what follows.

**Remark 3.2.** *The numerical flux $\hat{f}$ given by* (3.9) *can be reduced to an E-flux of the form $\hat{f}_e = f(u(x_e, t))$ like the Godunov flux, the Enquist-Osher flux or the Lax-Friedrichs flux for $\Delta t$ small enough. For a justification see Osher (1984).*

Assuming again time integration under enough regularity the weak formulation is then rewritten as

$$\int_{I_e} u^{(\ell)} v \, dx = \int_{I_e} u^n v \, dx + \int_{t^n}^{t^{n+k_\ell}} \int_{I_e} f(u) \, v_x \, dxdt - \int_{t^n}^{t^{n+k_\ell}} \left[\hat{f}_{e+1} \, v(x_{e+1}^-) - \hat{f}_e \, v(x_e^+)\right] dt - \int_{t^n}^{t^{n+k_\ell}} \int_{I_e} \hat{\varepsilon}(u) \, u_x v_x \, dxdt \quad (3.11)$$

In order to determine the shock-capturing term the RKDG scheme described by (3.5a) and (3.5b) in replaced into (3.11) to obtain

$$\int_{I_e} \Lambda\Pi_h(u^{n+k_\ell}) v \, dx = \int_{I_e} u^{n+k_\ell} v \, dx - \int_{t^n}^{t^{n+k_\ell}} \int_{I_e} \hat{\varepsilon}(u) \, u_x v_x \, dxdt \quad (3.12)$$

Assuming $\hat{\varepsilon}$ constant for $x \in I_e$ and $t \in [t^n, t^{n+k_\ell}]$ an explicit expression for the artificial diffusion coefficient is obtained

$$\hat{\varepsilon} = \Big(\int_{I_e} \big(u^{n+k_\ell} - \Lambda\Pi_h(u^{n+k_\ell})\big) v \, dx\Big) \Big/ \Big(\int_{t^n}^{t^{n+k_\ell}} \int_{I_e} u_x v_x \, dxdt\Big) \quad (3.13)$$

where $u^{n+k_\ell}$ is the standard DG solution (not limited) obtained from (3.5a) and $\Lambda\Pi_h(u^{n+k_\ell})$ is the reconstructed solution (3.5b), whose structure is described in (3.7).

In fact, for each Legendre polynomial $v = P_i$, $i = 1, \ldots, p$, a viscosity is obtained, say $\{\hat{\varepsilon}_i\}_{i=1,\ldots,p}$. Thus each viscosity $\hat{\varepsilon}_i$ contains information of the reconstructed moment $\tilde{c}_i$. Of course, from (3.7) and (3.13) it is obvious that $\hat{\varepsilon}_i = 0$ for $i = 0, \ldots, k$. Notice that $\hat{\varepsilon}_0 = 0$ since $c_0^e = \tilde{c}_0^e$ (conservation of mean value within the element).

Using the orthogonality and hierarchy of Legendre polynomials in (3.13), viscosities are readily computed

$$\hat{\varepsilon}_i = \frac{h^2(c_i^e - \tilde{c}_i^e)}{2(2i+1)} \Big[ \int_{t^n}^{t^{n+k_\ell}} \int_{-1}^{1} u_\xi \frac{dP_i}{d\xi}\, d\xi dt \Big]^{-1} \quad \text{for } i = k+1, \ldots, p, \tag{3.14}$$

where $h$ is the element size and $\xi$ are the local coordinate in the reference element $[-1, 1]$.

Only the maximum viscosity is retained, because it corresponds to the lower-order reconstructed moment

$$\hat{\varepsilon} = \max\{\hat{\varepsilon}_{k+1}, ..., \hat{\varepsilon}_p\} = \hat{\varepsilon}_{\min\{i|\tilde{c}_i^e \neq c_i^e\}} \tag{3.15}$$

Roughly speaking, a bigger amount of viscosity is required to impose monotone lower-order derivatives than higher-order ones.

### Order of the introduced diffusion

There are two key points to ensure the success of a shock-capturing method. First, it is crucial to preserve accuracy in smooth regions and second, it is required to obtain sharp shock profiles, not directly proportional to the element size.

Assuming sufficient regularity in (3.13) and (3.15), the order of the introduced artificial diffusion can be infered by a simple analysis based on modal coefficients of the approximation.

In fact, the degrees of freedom $c_j^e(t)$ of an approximation of the form (3.6) are of order $\mathcal{O}(h^j)$ for $j = 0, \ldots, p$. Using basic orthogonality properties of Legendre polynomials and assuming $c_j(t)$ constant on $]t^n, t^{n+k_l}[$, a Taylor analysis of (3.13) demonstrates that the introduced viscosity scales like

$$\hat{\varepsilon} \sim \begin{cases} \mathcal{O}\big(h^{k+1}/\Delta t\big) & \text{if } k \text{ is even} \\ \mathcal{O}\big(h^{k+2}/\Delta t\big) & \text{if } k \text{ is odd} \end{cases}$$

where $k$ is the last non reconstructed moment in (3.7). Note that the time step $\Delta t$ is chosen to satisfy the CFL condition in every step of the TVD-RKDG methods; in fact, $\Delta t \sim \mathcal{O}(h)$, see Cockburn and Shu (2001).

In contrast with the more standard approaches by Cockburn and Shu (1989) which introduce a shock profile of $\mathcal{O}(h)$, the proposed diffusion scales as $\mathcal{O}(h^k)$ for $1 \leq k \leq p$. Numerical examples indicate that, in general, $k > 1$. Thus accuracy is usually higher than one in the shock regions. Compared to other artificial diffusion techniques , Persson and Peraire (2006) or Barter and Darmolfal (2007), where diffusion scales like $\hat{\varepsilon} \sim \mathcal{O}(h/p)$, the proposed artificial diffusion is in general smaller when relatively coarse meshes and high degree of approximation are used. Numerical tests corroborate this issue.

**Extension to a system of equations**

The extension to nonlinear system of equation, for instance the Euler equations (1.1), is standard: the artificial viscosity is applied to the characteristic variables i.e, Riemann variables, see Section 1.4.1 or Donea and Huerta (2003). In one space dimension, the system of Euler equations in conserved variables can be written as

$$U_t + F(U)_x = 0 \tag{3.16}$$

where $U = (\rho, \rho v, \rho E)^T$ and $F(U) = (\rho v, \rho v^2 + p, (\rho E + p)v)^T$.

The system of characteristic variables is obtained multiplying (3.16) by the inverse of the matrix of right eigenvectors of the Jacobian of the flux $F(U)$, namely $\mathbf{R}^{-1}$, that is,

$$\mathbf{R}^{-1}\Big(U_t + F(U)_x\Big) = 0$$

Recall from Section 1.4.1 that a diagonal system of equations is obtained. Introducing the characteristic variable $W = \mathbf{R}^{-1}U$, a system of 3 decoupled equations is obtained, see equation (1.4). Then, the computation is straightforward: a single viscosity for each characteristic variable is obtained by using the method proposed

here. Due to the diagonalization, each viscosity is computed independently from one another. The result is mapped back into the conserved variables space by multiplication with the matrix of right eigenvectors, obtaining a non-constant artificial viscosity tensor for the system of conserved quantities.

#### Shock detection

Introducing just the necessary diffusion is important but it is also crucial to do it where it is needed. The smoothness indicator proposed by Persson and Peraire (2006) and explained in detail in Section 2.2 is again used here.

Recall that the sensor is expressed as one simple non-linear equation, $S^e(s)$, that detects spurious numerical oscillations within each element. It has been consistently proven that the sensor is very efficient in the presence of high-order elements, which are standard in DG. Moreover, the use of orthogonal and hierarchical polynomial basis simplifies computations, see (2.9).

### 3.1.3 Sub-cell extension for the artificial diffusion method

In this setting the discontinuity sensor $S^e(s)$ is an element-based integral and $\varepsilon(u)$ takes constant value within each element. However, from (3.2) one can think that the discrete approximation generated by the numerical scheme is an exact solution to a slightly perturbed PDE of the original conservation law (3.1). According to this, the *ideal* diffusion should be a continuous function, not only depending on the solution, but also pointwise defined, that is $\varepsilon(u(x))$. However, the shock location for a given flow field is rarely known *a priori* and the artificial viscosity cannot be a pre-determined function in space. Moreover, a pointwise switch, based on purely local quantities, is not yet a dependable option at higher-order interpolations due to the severe numerical noise in the shock layer.

Nevertheless, constant artificial viscosity within each element may have some drawbacks. Specifically, for large elements where the shock width is far more thinner than the element size, a more local diffusion may be beneficial, especially in terms of accu-

racy.

Keeping in mind these shortcomings, an extension of the proposed artificial diffusion into a division of sub-cells within each element is described in the following section.

### Sub-cell shock detection

First, it is necessary to identify more precisely the shock within the element. With this purpose, the computational element $I_e$ is divided into small patches of size $h/p$, namely sub-cells, and the usual discontinuity sensor $S^e(s)$ is applied over each one of them. This procedure is only perfmored in those elements identified by the elementwise sensor.

Here, for simplicity, the sub-cells are a uniform partition of each element $I_e = [x_k, x_{k+1}]$. For an approximation of degree $p \geq 2$ the interior nodes of the high-order mesh define the subdivision. Hence, each element is divided into a set of $p$ non-overlapping intervals, that is,

$$I_e = \bigcup_{l=1}^{p} I_e^l \qquad \text{with } I_e^l = [x_k, x_{k+1/p}, ...., x_{k+1}] \tag{3.17}$$

Projecting the elemental solution $u(x,t)$ of $I_e$ over each sub-cell an approximation of degree $p$ is obtained within each subinterval $I_e^l$. If element $I_e$ has been detected for the sensor as an element containing numerical oscillations the subsensor is applied within each of the sub-cells $I_e^l$ for $l = 1, \ldots, p$. Hence, the computational overhead of recomputing the sensor within the element is only reduced to a few number of elements. It is worth noting that the subdivision (3.17) is only considered with the purpose of applying the sensor to a more local entity, i.e, the computational mesh is not refined and hence, this procedure does not increase the computational cost. The solution is still defined as a $p$th order approximation within the element $I_e$.

This procedure would, at best, increase the accuracy of the shock location, which will be limited to a region of width $h/p$, rather than $h$. At worst, the size of the

detected area will still remain as the element size, $h$. To increase $p$ also improves the accuracy of this adaptive procedure, as numerical tests consistently show.

### Sub-cell viscosity

Following this idea the artificial diffusion could be defined within each element as a piecewise function, providing then a closer approximation to the *ideal* pointwise viscosity.

Here, piecewise constant viscosity within each sub-cell is computed, by means of (3.13) and (3.15). However, other approaches may be considered. For instance, a gaussian function centered at the detected region with deviation equal to the total length of the detected sub-cells is suggested by Barter and Darmolfal (2007) for elementwise viscosity.

To illustrate the gaussian viscosity, consider for instance the following function

$$u(x) = xe^{-\lambda}\frac{(1-e^{-\lambda})\mathrm{erf}\left(\frac{1}{2\sqrt{2\epsilon}}\right)}{\mathrm{erf}\left(\frac{1}{\sqrt{2\epsilon}}\right)}.$$

with $\lambda = 2$ and $\epsilon = 0.00025$, which consists on a step gradient centered at $x = 0$. Figure 3.1 shows a possible distribution of gaussian artificial viscosity centered at the step gradient of the domain. Grid lines correspond to computational elements. Note that the elementwise sensor will identify elements 4 and 5 (with coordinates $[0.4, 0.5]$ and $[0.5, 0.6]$, respectively). The amplitude of the gaussian must be determined depending on several parameters, such as the width of the detected are and oscillations which may appear in vicinities of the shock. Continuity of the viscosity within the element will preclude possible oscillations in the derivative $u_x$ of the function, which may be beneficial in terms of error estimates, for instance. Further research on this topic can be found by Barter (2008).

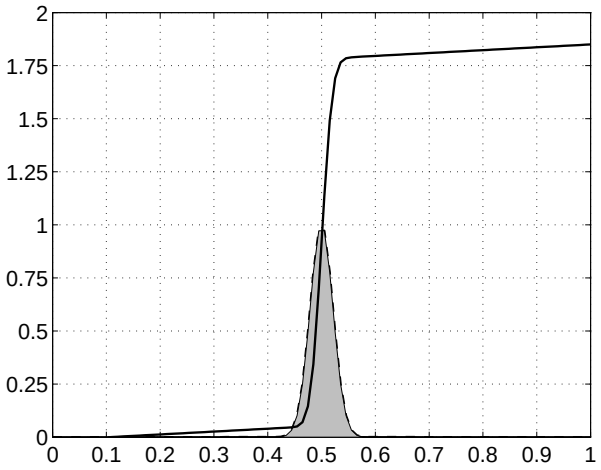


Figure 3.1: Distribution of gaussian artificial viscosity over a function with high gradient.

## 3.2 Multi-dimensional artificial viscosity

This section presents the extension to general triangular meshes of the one-dimensional artificial diffusion method described by Casoni et al. (2009).

Given an approximate solution within each element, $u(x, y)$, obtained with the DG method, the essential idea is to compute the solution along each spatial direction of the two-dimensional space and apply the one-dimensional viscosity model to each direction. However, for general triangular meshes this extension is not trivial: directions $x$ and $y$ are coupled in the expansion of the solution. Moreover, cartesian coordinates do not seem to be the natural choice for triangular meshes. Instead, triangular coordinates, also known as *barycentric coordinates*, provide a more practical approach for triangles.

### 3.2.1 From cartesian to barycentric coordinates

Barycentric coordinates is a coordinate system corresponding to masses placed at the vertices of a reference simplex. Consider the general triangle of vertices $ABC$, displayed in Figure 3.2 (left). In a triangle, barycentric coordinates are also known

as area coordinates, because the coordinates of an arbitrary point $P$ with respect to the triangle $ABC$ are proportional to the signed areas of $PBC, PCA$ and $PAB$. In particular, the barycentric coordinates are defined by the triple of numbers $(\alpha, \beta, \gamma)$ such that each coordinate is defined as the ratio between the triangular subdomain formed by point P and two vertices and the whole triangle, as shown in Figure 3.2 (right).

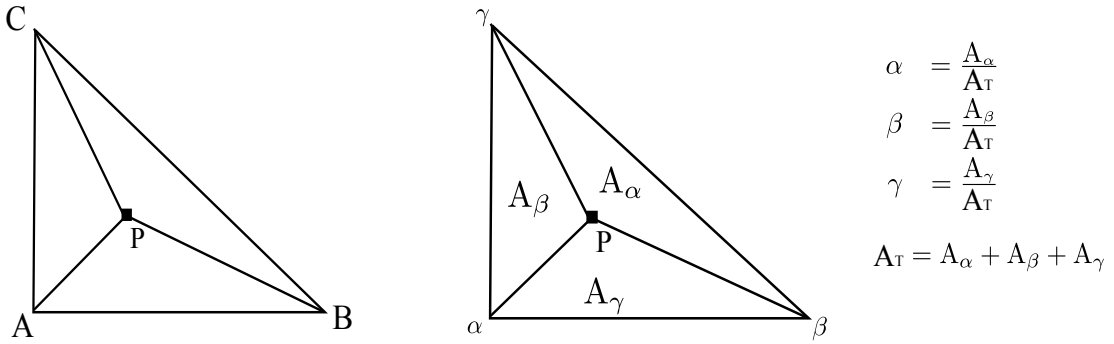


Figure 3.2: Area coordinates.

Formally, given a triangle of vertices $(x_i, y_i)$ for $i = 1, 2, 3$, the barycentric coordinates $(\alpha, \beta, \gamma)$ are defined by a linear relation between them and the cartesian ones, which is given by the following system:

$$\begin{aligned} x &= \alpha x_1 + \beta x_2 + \gamma x_3 \\ y &= \alpha y_1 + \beta y_2 + \gamma y_3 \\ 1 &= \alpha + \beta + \gamma \end{aligned} \tag{3.18}$$

Each coordinate takes value equal to zero along one edge and equal to 1 at the opposite vertex. For instance, vertex $A = (x_1, y_1)$ has barycentric coordinates $(1, 0, 0)$ with $\alpha = 1$ and $\beta = \gamma = 0$.

Relation (3.18) implies that $\alpha$ contours are straight lines equally spaced and parallel to edge $\overline{\beta\gamma}$, in which $\alpha = 0$, see Figure 3.3. Analogous relation is accomplished for $\beta$ and $\gamma$, with edges $\overline{\gamma\alpha}$ and $\overline{\alpha\beta}$ respectively.

**Remark 3.3.** *Any function defined in a triangle may be expressed either in cartesian*

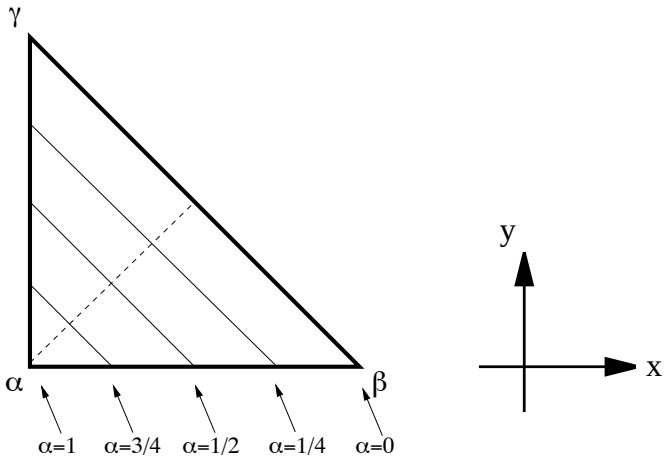


Figure 3.3: Barycentric coordinates.

*or triangular coordinates. Explicitly, a simple manipulation of Equation* (3.18) *shows that, for a general triangle of vertices* $(x_i, y_i)$ *for* $i = 1, 2, 3$*, the barycentric coordinates of an arbitrary point* $(x, y)$ *wtihin the triangle are*

$$\begin{aligned}
\alpha &= \frac{(x_2y_3 - x_3y_2) + (y_2 - y_3)x + (x_3 - x_2)y}{2\Delta} \\
\beta &= \frac{(x_3y_1 - x_1y_3) + (y_3 - y_1)x + (x_1 - x_3)y}{2\Delta} \\
\gamma &= \frac{(x_1y_2 - x_2y_1) + (y_1 - y_2)x + (x_2 - x_1)y}{2\Delta}
\end{aligned} \tag{3.19}$$

*with*

$$\Delta = \frac{1}{2} det \begin{vmatrix} 1 & x_1 & y_1 \\ 1 & x_2 & y_2 \\ 1 & x_3 & y_3 \end{vmatrix}$$

In the Finite Element community it is usual to consider a reference triangle, ex-

pressed in local coordinates, to simplify computations. Hence, given a general triangle of straight sides in cartesian coordinates, a standard linear mapping, see Figure 3.4, between this triangle and the reference one of vertices $(0,0),(1,0),(0,1)$ is used to pass from the physical domain to the reference element. Tus, barycentric coordinates in terms of this reference triangle in local coordinates $(\xi,\eta)$ are defined by

$$\begin{aligned} \alpha &= 1-\xi-\eta \\ \beta &= \xi \\ \gamma &= \eta. \end{aligned} \tag{3.20}$$

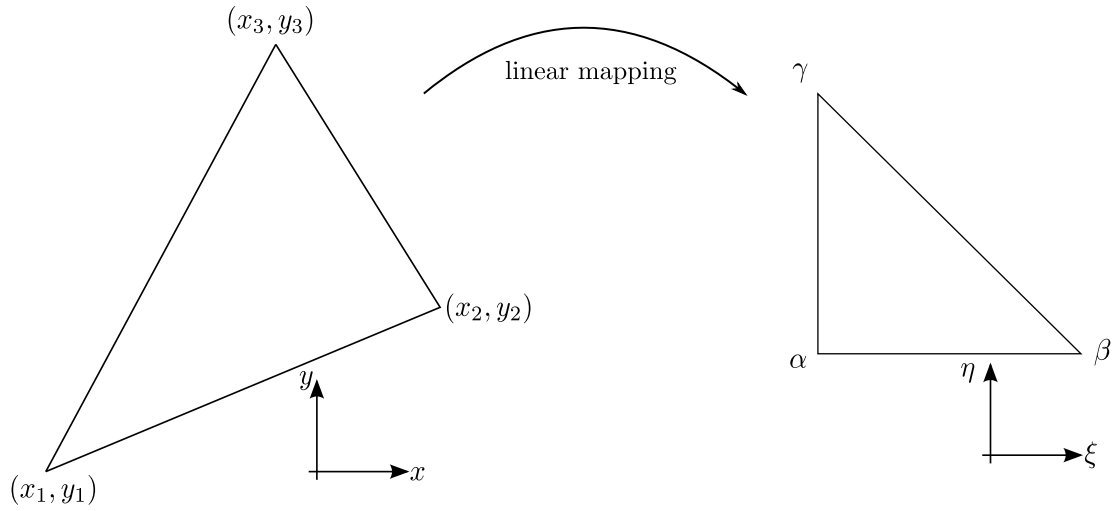


Figure 3.4: Two dimensional domain transformation.

### 3.2.2 From 2D to 1D

The computation of one-dimensional approximations within the triangle is assessed in this section. The goal is to obtain one-dimensional projections of the approximate solution $u(x,y)$ in order to apply the viscosity model defined in Section 3.1.2. In particular, the solution $u(x,y)$ is projected along three directions within the triangular element.

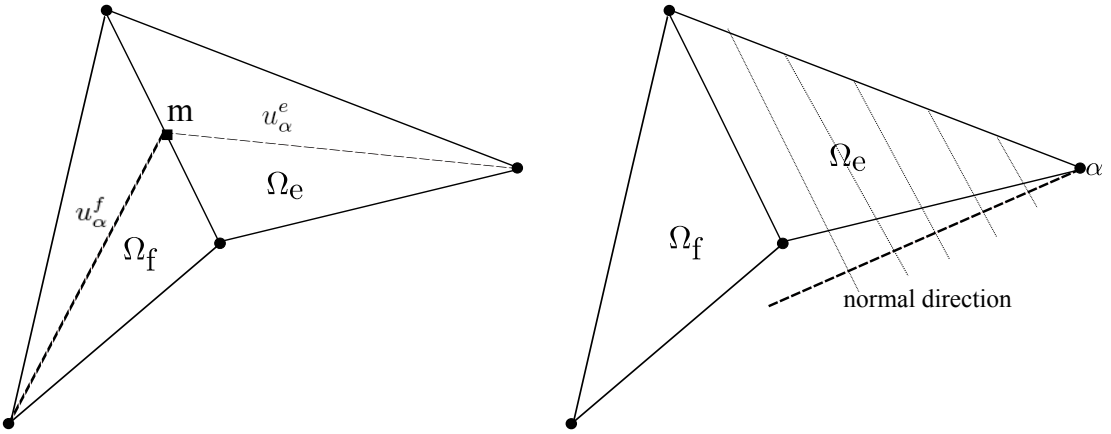


Figure 3.5: Possible directions of projection.

A question which arises from the elaboration of the one-dimensional approximations for triangular meshes is concerned with the choice of the directions to project the solution. Two natural choices can be considered: first, for each barycentric coordinate the normal direction to its contours is proposed, see Figure 3.5 (right). Despite this option appears to be the natural one, it has been ruled out since for degenerate triangles this direction may not be contained within the computational element. Second option is to consider the direction defined by the medians of the triangle, that is, the direction given by joining each vertex with the midpoint of its opposite edge, see Figure 3.5 (left). In this case, the projection will be always contained within the element. For instance, the direction associated to coordinate $\alpha$ is given by the median $\overline{\alpha m_\alpha}$, where $m_\alpha$ denotes the midpoint of the opposite face to the vertex, that is the midpoint of edge $\overline{\beta\gamma}$, following the notation introduced in the previous section. In contrast with the multi-dimensional slope limiter techniques, see Cockburn et al. (1990) and Burbeau et al. (2001), this approach leads to a scheme which does not depend on the mesh geometry and can be defined for any triangular element.

Once the directions are defined, consider then the approximate solution $u(x, y)$ of order $p$ in an arbitrary element $\Omega_e$. Using the linear mapping from cartesian to local coordinates, see Figure 3.4, the approximation is written in local coordinates,

$u(\xi(x,y),\eta(x,y))$. The projection along the median $\overline{\alpha m_\alpha}$ is given by

$$u_\alpha(\alpha) = u\Big(\frac{1-\alpha}{2}, \frac{1-\alpha}{2}\Big).$$

The justification for this projection is outlined in what follows.

Since any point of the median $\overline{\alpha m_\alpha}$ satisfies $\beta = \gamma$, it has barycentric coordinates $(\alpha, \frac{1}{2}, \frac{1}{2})$. Using this relation and replacing it into (3.20), any pair of coordinates $(\xi, \eta)$, may be parameterized with a single parameter, say $\alpha$, as

$$\xi = \frac{1-\alpha}{2}\,, \qquad \eta = \frac{1-\alpha}{2}. \tag{3.21}$$

An analogous procedure with coordinates $\beta$ and $\gamma$ gives similar relations. Projections along each coordinate are given then by the following expressions

$$\begin{aligned} u_\alpha(\alpha) &= u\Big(\frac{1-\alpha}{2}, \frac{1-\alpha}{2}\Big) \\ u_\beta(\beta) &= u\Big(\beta, \frac{1-\beta}{2}\Big) \\ u_\gamma(\gamma) &= u\Big(\frac{1-\gamma}{2}, \gamma\Big) \end{aligned}$$

Note that each expression is a polynomial of degree $p$ within each variable, $\alpha$, $\beta$ and $\gamma$, respectively. This is obvious since the approximation $u(x,y)$ is a polynomial of degree $p$ in $(x,y)$. That is, for all $x, y \in \mathbb{R}$,

$$u(x,y) = \sum_{|i+j|\leq p} a_{ij} x^i y^j$$

with $a_{ij} \in \mathbb{R}$.

**Remark 3.4.** *It is also possible to work with cartesian coordinates and find the parameterization* $u_\alpha(\alpha(x,y))$ *instead of* (3.21) *just by considering the relation* (3.19) *and the midpoints of the edges in cartesian coordinates, that is* $m_\alpha = \Big(\frac{x_2+x_3}{2}, \frac{y_2+y_3}{2}\Big)$. $m_\beta$

*and $m_\gamma$ have the same expression but with cyclic permutation of indices. Nevertheless, expressions and computations in cartesian coordinates become more involved.*

**Remark 3.5.** *In* (3.21) *the median has been chosen as the direction of projection in order to obtain one-dimensional polynomial approximation of degree p. However, the choice is not unique: any direction obtained by joining a vertex of the triangle with an arbitrary point $P$ of the opposite edge gives a polynomial of degree p within the barycentric coordinate associated to the vertex. For instance, consider the vertex $\alpha$ and a point $P_\alpha = (0, k, 1-k)$ of edge $\overline{\beta\gamma}$, with $0 < k < 1$. Any point $Q$ of the segment $\overline{\alpha P_\alpha}$ may be written as $Q = P_\alpha t + \alpha(1-t)$, for $t \in (0, 1)$. By writing this expression in local coordinates $(\xi, \eta)$ it is easily demonstrated that $\beta/\gamma = k/(1-k)$. By reproducing the procedure of the projection over the median, the following parameterization for any pair $(\xi, \eta)$ of the triangle is obtained*

$$\xi = \frac{1-\alpha}{(1+\frac{k}{1-k})}\,, \qquad \eta = \frac{1-\alpha}{(1+\frac{k}{1-k})}$$

*for $0 < k < 1$.*

### 3.2.3 Definition of artificial diffusion in the element

In order to define de artificial viscosity, the one-dimensional method presented in-Section 3.1.2 is recalled. Consider the single-parameter approximations, $u_\alpha, u_\beta, u_\gamma$, obtained by the projection detailed in the previous section. The limited solutions $\Lambda\Pi_h(u_\alpha), \Lambda\Pi_h(u_\beta), \Lambda\Pi_h(u_\gamma)$ are then easily computed by following the high-order limiting procedures by Biswas et al. (1994). Recall that, by limiting the solution coefficients, this method retains as high an order as possible, and does not automatically reduce accuracy to first order. However, although the approximations are one-dimensional polynomials, the computational element is a two-dimensional struc-

ture and hence, standard limiting procedures in 1D should be modified in some way. Consider the two adjacent elements $\Omega_e$ and $\Omega_f$ and the projections $u^e_\alpha(\alpha)$ and $u^f_\alpha(\alpha)$ along $\overline{\alpha m_\alpha}$ for each one, see Figure 3.5 (left). For simplicity the projections are expanded in terms of orthogonal Legendre polynomial, within each element $u_\alpha$ may be written as

$$u^e_\alpha = \sum_{i=0}^{p} a^e_i(t) P_i(\alpha) \qquad\qquad u^f_\alpha = \sum_{i=0}^{p} a^f_i(t) P_i(\alpha)$$

where the expansion coefficients of each element are emphasized with superscripts $^e$ and $^f$ and the $P_i$ are the Legendre polynomials. As usual, beginning with the coefficient associated with the highest polynomial degree (i.e for $i = p, p-1, \ldots, 1$) the coefficient $a^e_i$ is replaced by

$$\tilde{a}^e_i = \text{minmod}(a^e_i, (a^e_{i-1} - a^f_{i-1})/2i - 3)$$

Analogous procedure is repeated for $u_\beta$ and $u_\gamma$. Note that, in contrast with the standard one-dimensional limiting techniques (Cockburn and Shu (1989), Biswas et al. (1994) and Krivodonova (2007)), the minmod function acts over two values, instead of three, due to the geometrical approach of the limiting directions.

Getting to this point, the computation of the artificial diffusion for each barycentric coordinate is straightforward, following Section 3.1.2. Three artificial viscosities, say $\varepsilon_\alpha, \varepsilon_\beta$ and $\varepsilon_\gamma$, are then obtained for each triangular element. With the purpose to obtain a single-valued viscosity within the element several options can be considered. For simplicity, here a scalar viscosity is computed by linearly combining the three values. Thus, artificial diffusion within the element is defined by

$$\varepsilon_e = (\varepsilon_\alpha + \varepsilon_\beta + \varepsilon_\gamma)/|\Omega_e|. \tag{3.22}$$

As numerical tests show, this approach, although requiring further research, seems promising. However it is worth to be investigated: for instance, tensorial viscosity might be beneficial in order to take into account the directionality of the shock.

## 3.3 Numerical Examples

A variety of numerical examples are now considered to show the capacity of the method to preserve the accuracy and to capture sharp shock profiles. An analysis of the introduced viscosity, where and how much, is also performed in the examples. Comparisons with classical methods in one-dimension, say slope limiters, are deeply analyzed. The novel shock-capturing method presented in Chapter 2, and the multi-dimensional artificial diffusion are also compared.

Appendix D presents a real application for the method, consisting on the modeling of highly adsorbent media. As pointed out, the application shows that the method can handle nonlinearities of different nature, such as nonlinear reaction terms.

### 3.3.1 One-dimensional tests

#### Linear advection

Here two linear tests are proposed. First, transport of a sinus wave shows that the proposed methodology does not affect the optimal order of convergence of high-order DG methods. Second, a more involved test convecting pulses and Gaussian functions is computed. Both examples are linear initial value problems with periodic boundary conditions and can be defined as

$$\begin{cases} u_t + u_x = 0, & -1 \leq x < 1,\ t > 0 \\ u(x,0) = u_0(x). \end{cases}$$

#### Transport of a sinus wave.

Table 3.1 shows error in the $L^1$ norm for the initial condition $u_0(x) = \sin(\pi x)$ at time $t = 2$ for $p = 1, 2, 3, 4$ on uniform meshes having 16, 32, 64, 128 and 256 elements. As expected, the optimal rate of convergence is obtained. Moreover, these errors are least one order of magnitud smaller compared to those presented by Krivodonova (2007) with high-order limiters.

Table 3.1: Transport of a sinus wave: errors in $L^1$ norm and rate of convergence.

| N | $p=1$ | | $p=2$ | | $p=3$ | | $p=4$ | |
|---|---|---|---|---|---|---|---|---|
| 16 | 1.64e-02 | | 2.78e-04 | | 4.70e-06 | | 9.10e-08 | |
| 32 | 4.10e-03 | 2.0023 | 3.46e-05 | 3.0036 | 2.92e-07 | 4.0044 | 2.83e-09 | 5.0050 |
| 64 | 1.03e-03 | 2.0006 | 4.32e-06 | 3.0009 | 1.83e-08 | 4.0011 | 8.85e-11 | 5.0013 |
| 128 | 2.56e-04 | 2.0001 | 5.40e-07 | 3.0002 | 1.15e-09 | 4.0003 | 2.76e-12 | 5.0003 |
| 256 | 6.40e-05 | 2.0000 | 6.75e-08 | 3.0001 | 7.13e-11 | 4.0001 | 8.63e-14 | 5.0004 |

**Transport of a combination of Gaussians and pulses.**

The same linear advection problem is solved with the initial condition

$$u_0(x)=\begin{cases} \frac{1}{6}\big(G(x,\beta,z-\delta)+G(x,\beta,z+\delta)+4G(x,\beta,z)\big) & \text{if } x\in[-0.8,-0.6],\\ 1 & \text{if } x\in[-0.4,-0.2],\\ 1-|10(x-0.1)| & \text{if } x\in[0,0.2],\\ \frac{1}{6}\big(F(x,\alpha,a-\delta)+G(x,\alpha,a+\delta)+4G(x,\alpha,a)\big) & \text{if } x\in[0.4,0.6],\\ 0 & \text{otherwise.}\end{cases}$$

where $G(x,\beta,z)=\exp(-\beta(x-z)^2)$, $F(x,\alpha,a)=\sqrt{\max(1-\alpha^2(x-\alpha)^2,0)}$, $a=0.5$, $z=-0.7$, $\delta=0.005$, $\alpha=10$, and $\beta=\log 2/(36\delta^2)$

The solution contains a combination of smooth but narrow Gaussian, a square pulse, a sharp triangle, and a combination of half-ellipses. Moreover, to further accentuate the dissipation introduced by slope-limiter or artificial diffusion techniques, the solution is computed after a long time, namely $t=8$.

Figure 3.6 compares the artificial diffusion technique proposed here with the high-order limiter proposed by Krivodonova (2007) (described as "moments" in the figures). Comparisons between these two techniques are always performed with the same number of degrees of freedom. In Figure 3.6(a) 400 degrees of freedom are employed; a mesh of 200 elements with $p=1$ and one of 50 elements with $p=7$ are used to compare these techniques. Figure 3.6(b) corresponds to a mesh of 200 elements with $p=2$ and one of 50 elements and $p=11$.

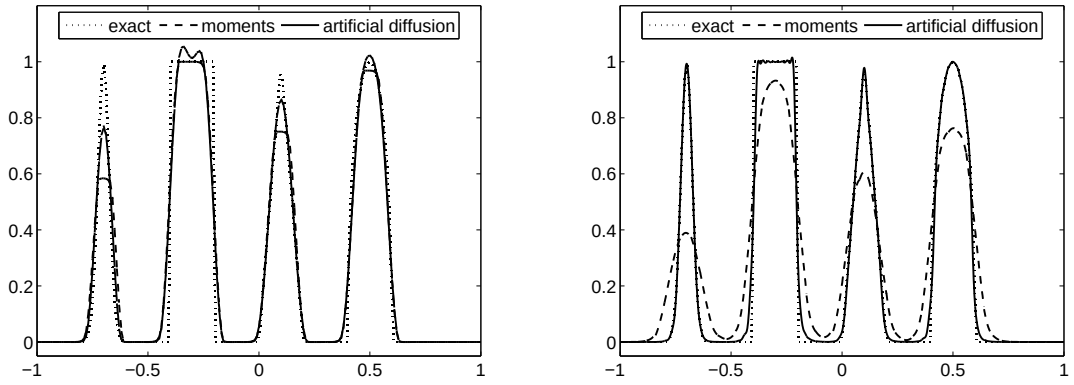


(a) 400 dof: 200 elements with $p = 1$ (left) and 50 elements with $p = 7$ (right)

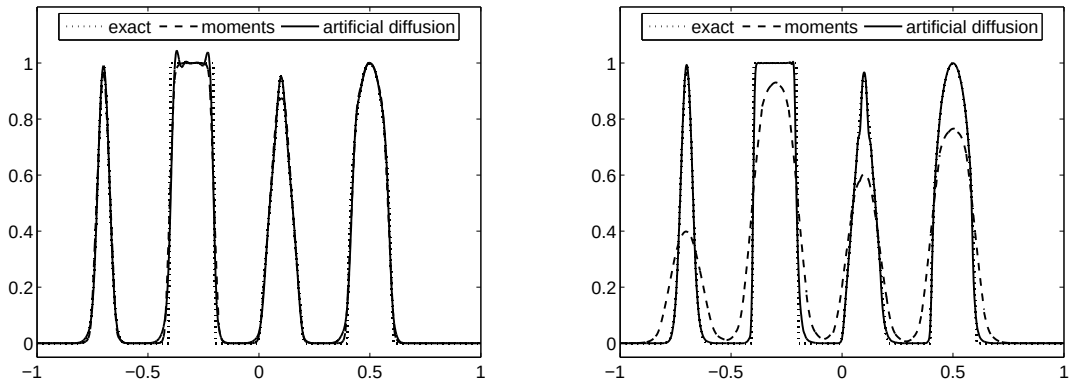


(b) 600 dof: 200 elements with $p = 2$ (left) and 50 elements with $p = 11$ (right)

Figure 3.6: Combination of Gaussians and pulses: comparison between high-order slope limiter ("moments") and artificial diffusion

In general the artificial diffusion techniques outperform the high-order limiting scheme. This is obvious for high-order elements, which is the natural tendency in DG methods. Large high-order elements allow with the artificial diffusion technique to resolve accurately the solution extrema. In contrast, high-order limiting requires, as expected, smaller and low-order elements to capture the features of the transported functions. In other words, it requires h-refinement.

Overshoots near discontinuities in $u$ for the square pulse are observed for the artificial diffusion technique. These overshoots, which should be expected in artificial

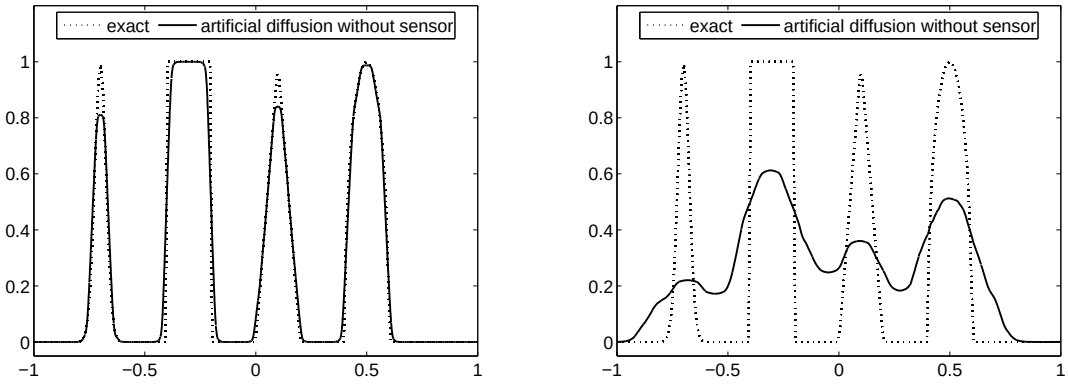


Figure 3.7: Combination of Gaussians and pulses: no discontinuity sensor for 200 elements with $p = 2$ (left) and 50 elements with $p = 7$ (right)

diffusion methods, are almost negligible for high-order approximations. Low-order polynomial approximations present clear localized oscillations in the pulse, see Figure 3.6.

Since the amount of artificial diffusion is directly proportional to the limited coefficients, in principle, one could guess that there is no need for any discontinuity sensor. If no limiting is necessary, the artificial diffusion is zero. Thus, in a sense the proposed approach already incorporates a discontinuity sensor. Figure 3.7 compares the artificial diffusion scheme with and without the discontinuity sensor for 200 and 50 elements. It is clear that such an approach is over-diffusive. Two key aspects contribute to this over-diffusion: constant element-by-element artificial diffusion and the proposed algorithm which always take the maximum computed diffusion. Note, as previously shown, that using the discontinuity sensor allows both to preclude an over-diffusive method and reduce the computation overhead only to the detected elements.

### A steady-state convection-diffusion problem

Next, a linear convection-diffusion example is studied,

$$\begin{cases} u_t + u_x - \nu u_{xx} = 1 & \text{in } [0,1],\ t > 0, \\ u(0,t) = u(1,t) = 0, \\ u(x,0) = 0. \end{cases}$$

For high Peclet numbers the solution of this problem develops a boundary layer at the end of the domain. Results are presented at $t = 1.2$ when the solution can be considered in steady state. All the computations are performed with $\nu = 0.001$ and discretizations are chosen such that Peclet is equal to 10.

As in the previous example, numerical tests show that the artificial diffusion method outperforms the high-order limiting technique and, in particular, it improves accuracy when coarse meshes and high-order approximations are used. Discretizations from $p = 1$ to $p = 12$ and number of elements such that the number of degrees of freedom is the same order for all of them have been tested. Figure 3.8 shows the results for a discretization with *low* order ($p = 3$) and a fine grid of 17 elements and a discretization with high order ($p = 11$) and a coarse grid of 5 elements. Note, for instance, that limiting techniques are not able to capture the boundary layer. Artificial diffusion method provides a more accurate solution than slope limiting techniques, especially when the order of the approximation is increased. It also ensures a major control of interelement jumps.

Moreover, in order to show that the proposed viscosity is sufficient to capture sharp shock profiles and non-oscillatory solutions, two artificial viscosity approaches are compared. The proposed artificial diffusion, denoted by $\varepsilon$, is compared with a technique that adds constant artificial viscosity of order $h/p$, here denoted by $\varepsilon^{h/p}$ , as suggested by Persson and Peraire (2006). Results for the same previous discretizations are shown in Figure 3.9, for $p = 3$ on the top plots and $p = 11$ on the bottom. Although similar solution profiles are obtained with both viscosities, numerical evidence

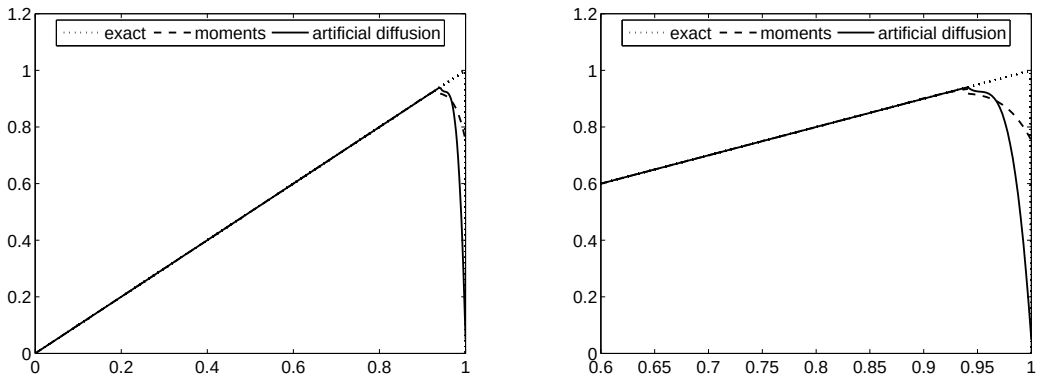


(a) 17 elements and $p = 3$

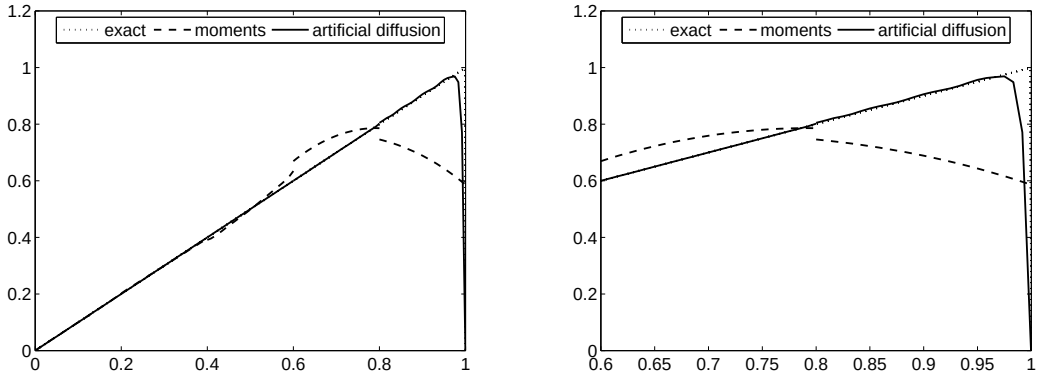


(b) 5 elements and $p = 11$

Figure 3.8: Steady-state convection-diffusion problem: figures on the right show the detail around the boundary layer.

indicates, for different degrees of approximation, that the viscosity computed with the approach proposed here is always smaller than the value $h/p$. Hence, higher accuracy is also expected. In fact, Figure 3.10 shows the amount of diffusion introduced in the last element at each time step for both cases, clearly demonstrating this fact.

To further differentiate the artificial diffusion solutions the $L^\infty$ and $L^1$-norm are computed in the region containing the shock, that is $\{x \in [0,1] | x > 0.8\}$. Both errors are also computed for the limited solutions. The $L^1$ error is also computed for the solution obtained with the high-order limiter. The $L^\infty$ error is not shown for the slope limiting technique because the lack of resolution at the boundary makes

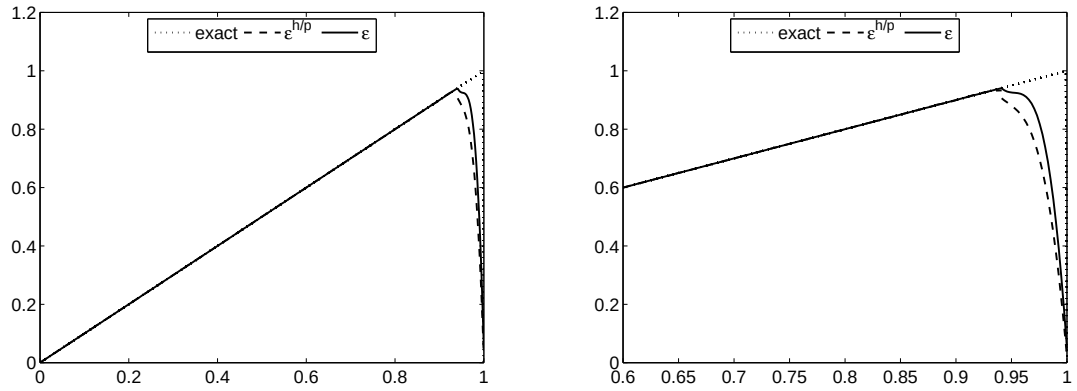


(a) 17 elements and $p = 3$

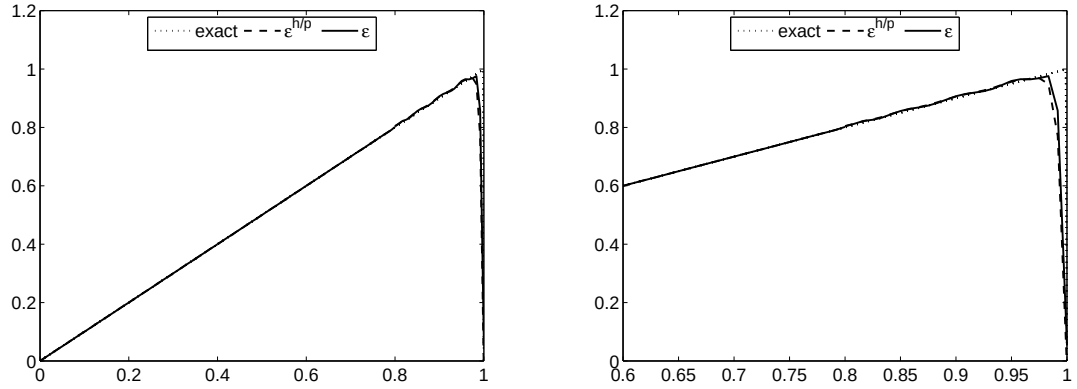


(b) 5 elements and $p = 11$

Figure 3.9: Steady-state convection-diffusion problem: comparison between a diffusion of order $h/p$ and the proposed technique.

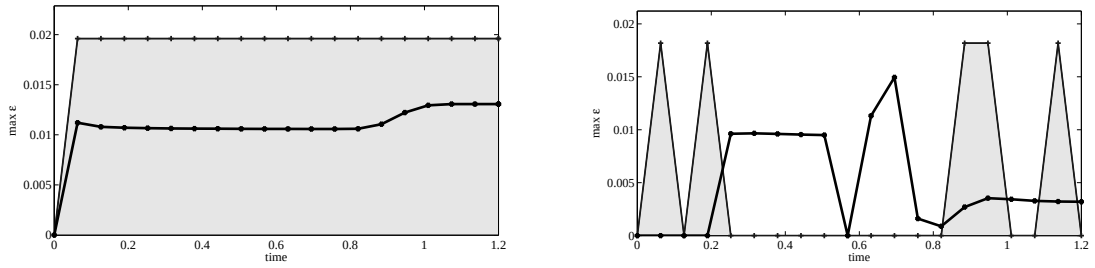


Figure 3.10: Steady-state convection-diffusion problem: evolution of artificial diffusion with time; the order $h/p$ viscosity is filled in grey and the proposed diffusion as a solid black line, left $p = 3$ and right $p = 11$.

this computation unreliable. The proposed methodology always presents the smallest errors, as shown in Table 3.2. For instance, it is reduced by one order of magnitude with respect to the limiters. In addition, note that the improvement is more relevant as the degree of approximation increases.

Table 3.2: Steady-state convection-diffusion problem: errors in $L^1$ and $L^\infty$ norms in the region of the shock $x > 0.8$ for different discretizations.

| | $L^1$ error | | | | $L^\infty$ error | | | |
|---|---|---|---|---|---|---|---|---|
| | $p=3$ | $p=5$ | $p=8$ | $p=11$ | $p=3$ | $p=5$ | $p=8$ | $p=11$ |
| Limiter | 0.0061 | 0.0154 | 0.0334 | 0.0438 | | | | |
| $\varepsilon = h/p$ | 0.0184 | 0.0111 | 0.0086 | 0.0062 | 0.8115 | 0.7721 | 0.7214 | 0.7493 |
| $\varepsilon$ proposed | 0.0133 | 0.0080 | 0.0070 | 0.0047 | 0.7437 | 0.7719 | 0.7001 | 0.6487 |

Despite the proposed approach gives good results for any degree of approximation, adding constant artificial diffusion in the whole element seems excessive when the shock width is far more thinner than the element size. For these situations, it may be beneficial to just add diffusion in a small region of the element, where the solution profile develops large gradients. Figure 3.11 shows the approximation of degree $p = 11$ over the mesh of 5 elements with the *sub-cell artificial diffusion* technique. A detail of the last two elements is also shown. The constant element-by-element artificial diffusion approach imposes a finite viscosity on $[0.8, 1]$, which is far more bigger than the shock width. But, with the sub-cell approach the artificial diffusion is only added in a region ten times smaller, i.e, $h/(p-1)$, obtaining a sharp shock free of spurious oscillations.

### Burgers' equation

In order to generalize the previous conclusions also for nonlinear problems the inviscid Burgers' equation with periodic boundary conditions and smooth initial condition is solved

$$\begin{cases} u_t + f_x(u) = 0 & \text{in } [0,1],\ t > 0, \\ u(x,0) = \frac{1}{2} + \sin(2\pi x). \end{cases}$$

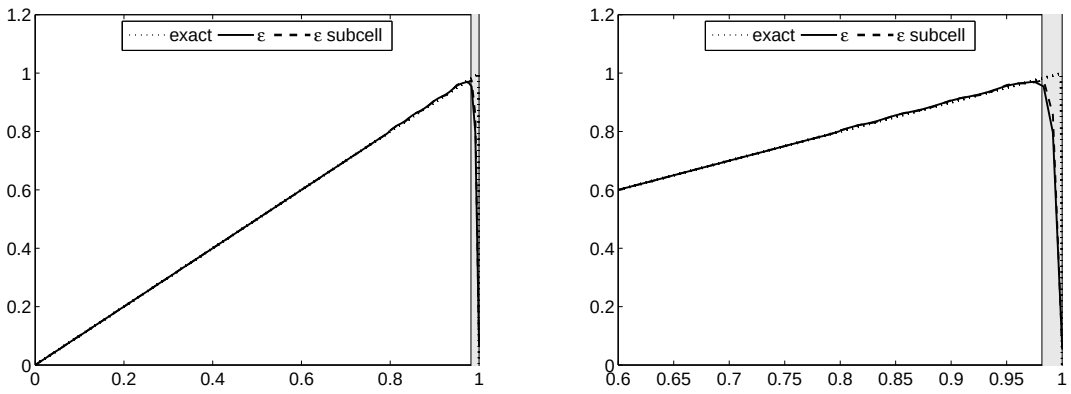


Figure 3.11: Steady-state convection-diffusion problem: the left figure shows the region detected by the subsensor is filled in grey, and the right one a detail is plotted.

Recall from Section 2.3.1 that a shock is completely formed at time $t = 0.5$.

Figure 3.12 shows a comparison between high-order slope limiting procedures and the artificial diffusion. The problem is solved on a mesh of 10 elements with $p = 5$ and $p = 10$ (left and right plots, respectively). Note that the high-order limiter proposed by Biswas et al. (1994) gives, in this case, the same results for $p = 5$ and $p = 10$. With the artificial diffusion method accuracy is improved as the degree is increased and also a sharper shock, free of oscillations, is obtained, see the detail of the shock in Figure 3.13.

Next, the proposed approach is compared with a constant artificial viscosity of order $h/p$, denoted by $\varepsilon^{h/p}$, as suggested in Persson and Peraire (2006). Figure 3.14 shows the obtained solution for $p = 3, 5, 8$ and 11 (from left to right and top to bottom) on a 10 element mesh. Both techniques produce similar shock profiles, in particular, as the order of the approximation is increased beyond 5. Note, however, that the proposed viscosity is notably smaller than the one of order $h/p$.

In order to better compare both approaches as well as their accuracy, the total amount of viscosity is computed. In contrast to the previous example, where the boundary layer is always located at the right boundary, here the formed shock evolves in time and hence, it may change from one element to another along the computation. Hence, in order to make a fair comparison, the total viscosity footprint is computed

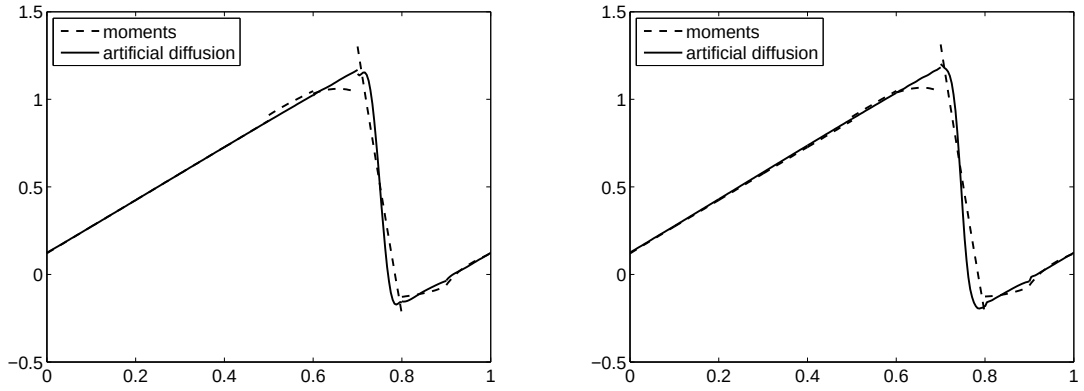


Figure 3.12: Burgers' equation: comparison between high-order slope limiter and proposed method for approximations of degree $p = 5$ (left) and $p = 10$ (right).

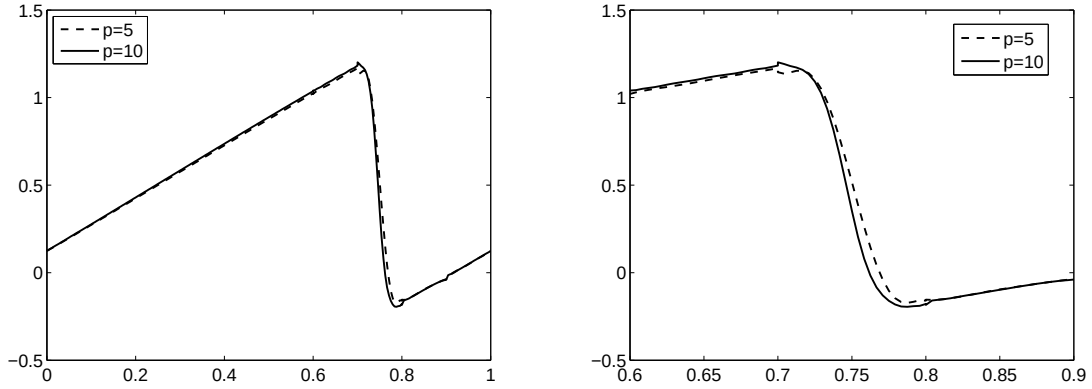


Figure 3.13: Burgers' equation: comparison between approximations of degree $p = 5$ and $p = 10$ for the artificial diffusion approach on a mesh of 10 elements, a detail is presented on the right.

as

$$\varepsilon_t = \sum_{e=1}^{\mathrm{n_{el}}} \int_{\Omega_e} \varepsilon \, dx \qquad \text{for each } t_i \in [0, t]. \tag{3.23}$$

Figure 3.15 shows the evolution of the added diffusion for a discretization of degree $p = 8$ and a mesh of 10 elements for both methods. Similar results are obtained for the different discretizations. The viscosity proposed here is always smaller than the

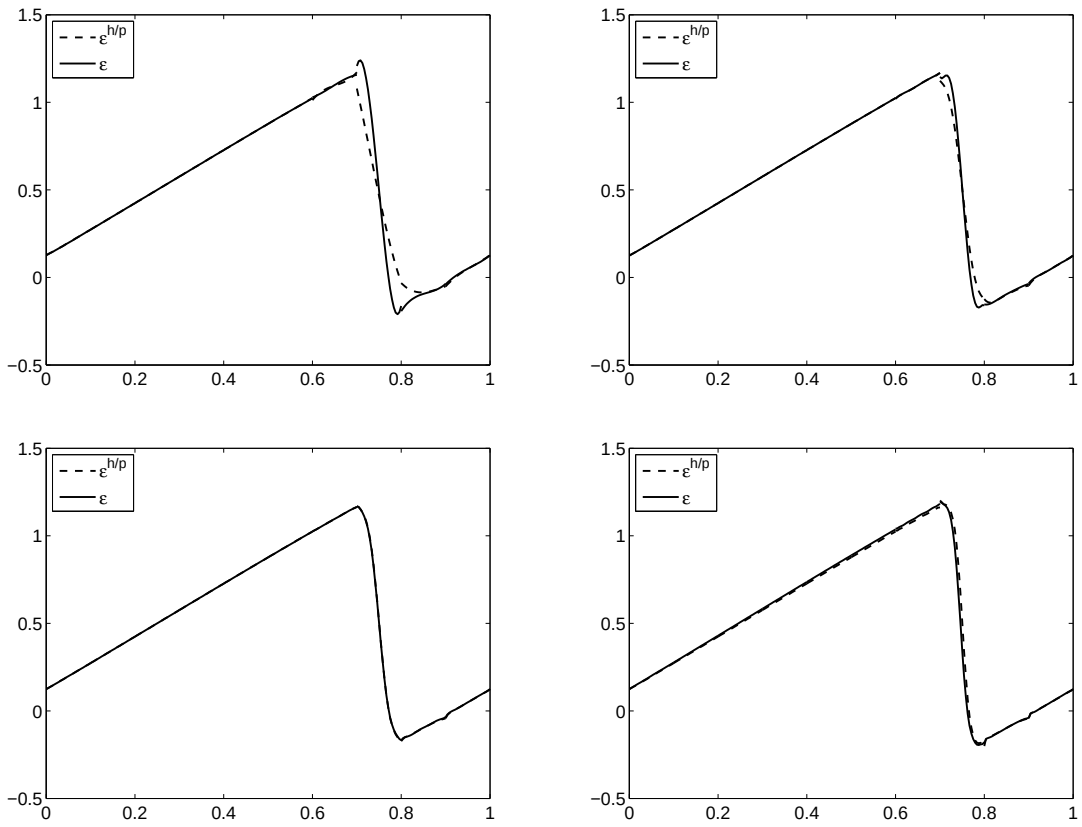


Figure 3.14: Burgers' equation: comparison between a diffusion of order $h/p$ and the proposed technique for a 10 element mesh with $p = 3, 5, 8$ and 11 form left to right and top to bottom.

theoretical value $h/p$. The mean value of the viscosity along all the process is also computed. That is,

$$\bar{\varepsilon} = \sum_{i=0}^{nt} \varepsilon_{t_i}$$

for a discretization in time $0 = t_0 < t_1 < \ldots < t_{nt} = t$. In Figure 3.16 it is compared for both approaches and different degrees of approximation. Note that the amount of viscosity required decreases as the degree of approximation $p$ increases.

In Figure 3.17 solution computed applying local viscosity on a mesh of 10 elements and degree $p = 8$ is shown. Dashed grid lines indicate the computational elements. Left figure shows the moving shock at time $t = 0.25$, when the shock is crossing

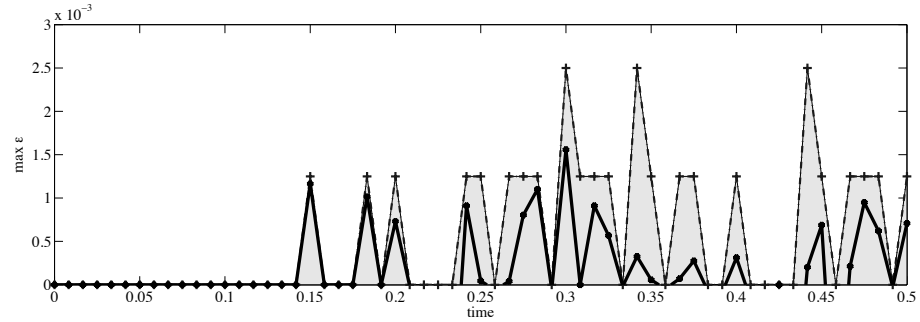


Figure 3.15: Burgers' equation: evolution of the viscosity for $p = 8$. Artificial diffusion of order $h/p$ (grey) and proposed diffusion (solid black line)

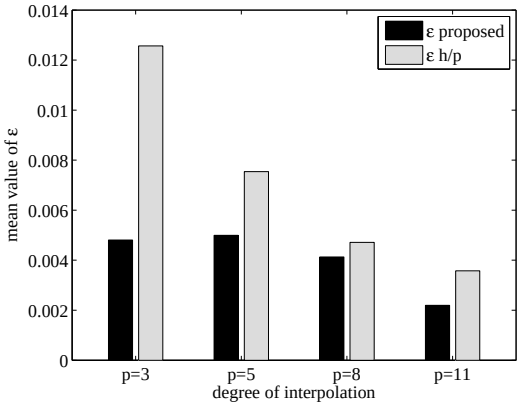


Figure 3.16: Burgers' equation: comparison of the mean value of the introduced viscosity along all the process for $p = 3, 5, 8$ and 11.

two elements. Notice that the sub-cell detection just identifies a small region within the two elements containing the shock. In contrast, an elementwise detection would identify the two elements sharing the shock (that is, a region of size $2h$), see for instance the approach by Persson and Peraire (2006). At time $t = 0.5$ the shock is contained within a single element. Again, the sub-cell detection gives a smaller viscosity footprint that the elementwise one. Hence, for both situations, when the shock in contained within a single element and also when it crosses the elements, the amplitude of the introduced viscosity is notably reduced.

The total amount of viscosity added along the computation is computed again following (3.13). Figure 3.18. clearly shows that the sub-cell viscosity improves accu-

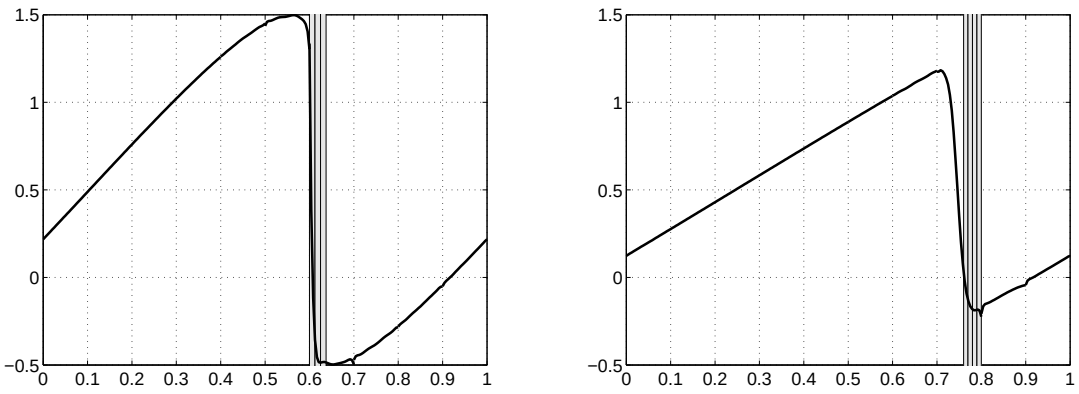


Figure 3.17: Burgers' equation: solution at time $t = 0.25$ (left) and $t = 0.5$ (right). The amplitude footprint of the detection is filled in grey.

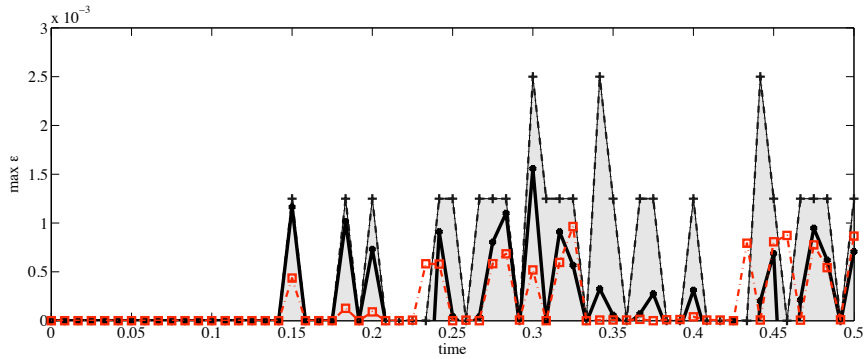


Figure 3.18: Burgers' equation: evolution of the viscosity for $p = 8$. Artificial diffusion of order $h/p$ (grey), elementwise diffusion (continuous line) and sub-cell diffusion (dashed line)

racy: along all the simulation, the total amount of viscosity is reduced, in comparison with the elementwise approaches. Just at the end of the computation both values are comparable.

To sum up, the use of large high-order elements does not imply a bigger amount of artificial viscosity. Although the sub-cell viscosity gives qualitatively similar profiles to the shock, a smaller viscosity footprint is obtained.

### The shock tube problem

The system of Euler equations is now considered. This test shows that the method can handle with nonlinear systems of conservations equations which develop solutions with more complicated structures and several shocks. Consider the classical Sods problem, described by LeVeque (2002), subject to the initial conditions

$$\vec{U} = (\rho, \rho v, \rho E)^T, \qquad \vec{F}(\vec{U}) = (\rho v, \rho v^2 + p, (\rho E + p)v)^T$$

$$(\rho, v, p) = \begin{cases} (3, 0, 3) & \text{if } 0 \leq x \leq 0.5, \\ (1, 0, 1) & \text{if } 0.5 < x \leq 1. \end{cases}$$

with $\gamma = 1.4$. This test is deeply analyze by LeVeque (2002). Solutions profiles at time $t = 0.2$ of the density, velocity and pressure are reported in the following figures.

Similarly, high-order limiting techniques are compared with the artificial diffusion approach introduced here. Figure 3.19 demonstrate again the superiority of the proposed approach. The left column shows the limiter solution obtained with 300 degrees of freedom (mesh of 100 elements with $p = 2$). The right column corresponds to the proposed technique with only 132 degrees of freedom (12 elements with $p = 10$). The plots are obvious. The smeared limited solution is clearly improved with sharper fronts for the artificial diffusion technique with less than half degrees of freedom. Note that in the proposed method sharp shock profiles are obtained which are far more thinner that the element size. Shocks are captured essentially in one element without production of spurious oscillations. This is particulary noticeably for the density variable, where only one element is needed to capture a discontinuity.

## 3.3.2 Two-dimensional tests

### Linear advection

The following example is addressed to demonstrate the well-behavior of the artificial diffusion method for the transport of shocks and sharp gradients. Consider the linear

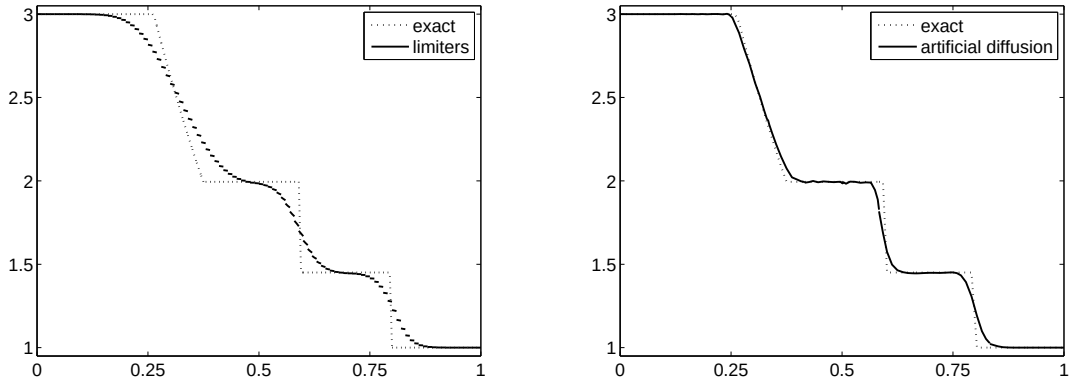


(a) density

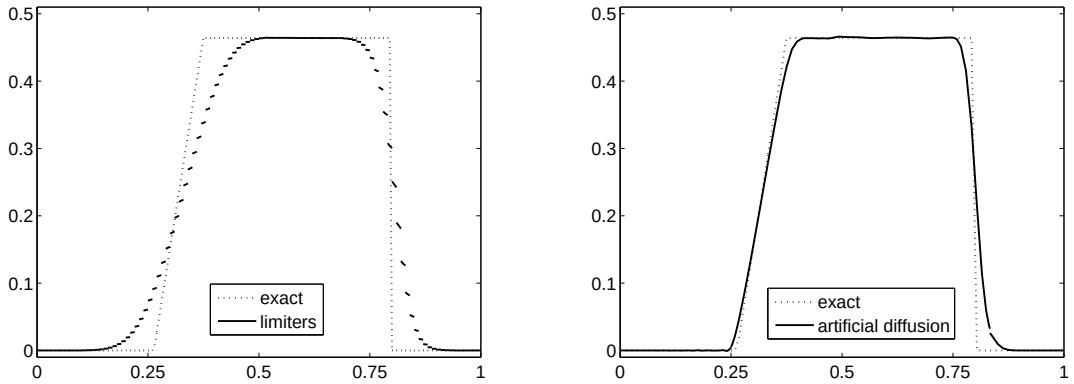


(b) velocity

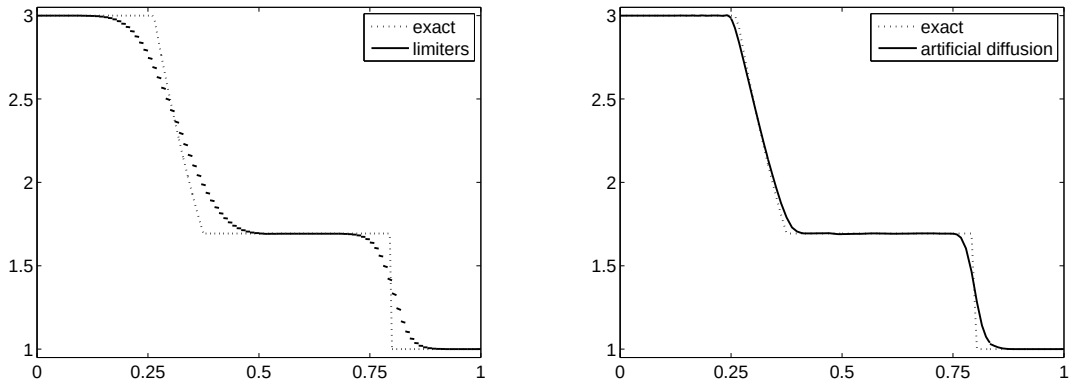


(c) pressure

Figure 3.19: Euler equations. Comparison between high-order limiters with 300 degrees of freedom (left) and artificial diffusion method with 132 degrees of freedom (right).

advection problem on a square $\Omega = [-1, 1] \times [-1, 1]$ with a profile consisting on a cone and a square pulse rotating clock-wise around the origin with velocity $\boldsymbol{v} = (2\pi y, -2\pi x)$. The initial conditions are given by

$$u_0(\mathbf{x}) = \begin{cases} \cos^2(2\pi r) & \text{if } r \leq 0.25, \\ 1 & \text{if } x \in [0.1, 0.6],\ y \in [-0.25, 0.25] \\ 0 & \text{otherwise.} \end{cases}$$

where $r = (x + 0.5)^2 + y^2$. Dirichlet boundary conditions equal to 0 are set.

Two different discretizations are considered: a mesh of 40 by 40 element and degree $p = 3$ (32 000 dof) and a mesh of 18 by 18 elements with degree $p = 8$ (29 160 dof). Both discretizations use uniform meshes and a reduced number of degrees of freedom, for instance compare with the mesh used by Krivodonova (2007).

To further accentuate the dissipation introduced by the artificial diffusion method, the solution is computed after four periods of time, namely $t = 4$. Figure 3.20 shows an intermediate solution at $t = 2.6$. There is no visual change in the shape of the solution between the approximations. Both shapes are transported without a trace in the domain. Figure 3.21 depicts the results obtained after four periods. A two-dimensional view of the solution is shown with the purpose to better compare the loss of accuracy at the contours along the simulation. Both solutions are in good agreement with the initial profiles, but the third order approximation presents smoother contours, especially in the square.

A more accurate analysis is obtained in Figure 3.22, which shows a cross section along $y = 0$ and compares both solutions with the exact one. The comparison reveals again the superiority of the higher order solution $p = 8$, showing sharper profiles. The maximum discrepancy is observed for the third order approximation between the cone and the square, due to the smearing along high gradients. However, in both cases the method prevails overshoots in the solution, thus indicating that artificial diffusion and high-order approximations might be beneficial for long-time simulations.

Next, same linear advection problem is solved but with a more involved configura-

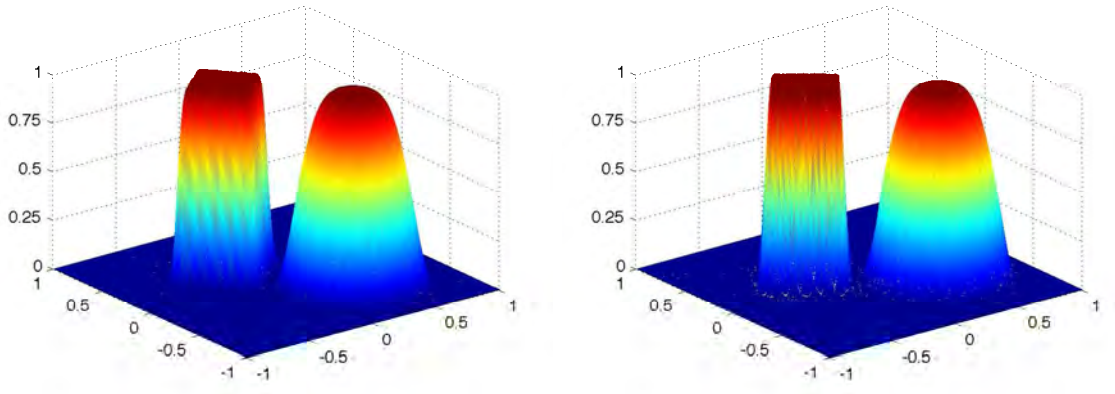


Figure 3.20: Linear advection: solution at time $t = 2.6$.

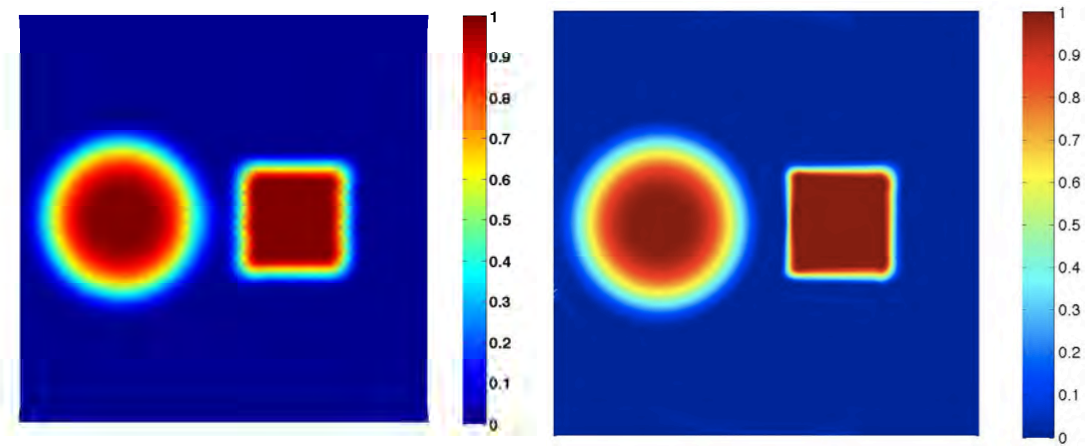


Figure 3.21: Linear advection: solution at time $t = 4$.

tion. The solid body is modeled with a scalar density function that has three shapes: a slotted cylinder, a cone and a sinusoidal hump. The problem is defined on the square domain $\Omega = [0, 1] \times [0, 1]$, with constant angular velocity $\boldsymbol{v} = (0.5 - y, x - 0.5)$. The initial conditions are given by:

$$u_0(x, y) = \mathrm{H}(R - \| \mathbf{r} - \mathbf{r_1} \|_2)[1 - \mathrm{H}(0.025 - |x - x_1|)\mathrm{H}(0.85 - y)] + 1 -$$
$$- \min\left(\frac{\| \mathbf{r} - \mathbf{r_2} \|_2}{R}, 1\right) + \frac{1}{4}\left[1 + \cos\left(\pi \min\left(\frac{|\mathbf{r} - \mathbf{r_3}|_2}{R}, 1\right)\right)\right]$$

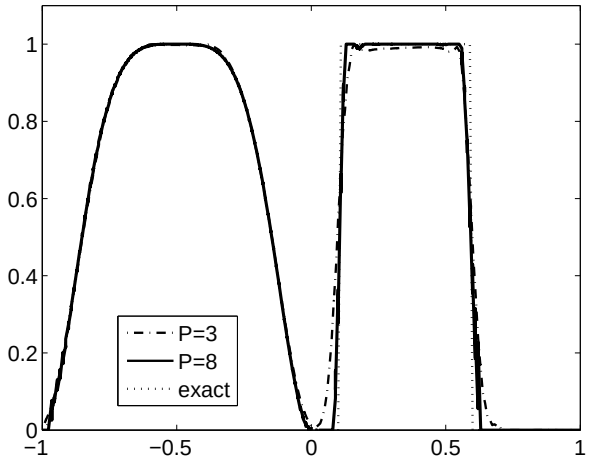


Figure 3.22: Linear advection: section across $y = 0$

with $R = 0.15$, $\mathbf{r} = (x, y)$, $\mathbf{r_1} = (0.5, 0.75), \mathbf{r_2} = (0.5, 0.25)$, $\mathbf{r_3} = (0.25, 0.5)$ and $\mathrm{H}(x)$ is the Heaviside function defined by

$$\mathrm{H}(y) = \frac{1 + \mathrm{sgn}(y)}{2} = \begin{cases} 0 & \text{if } y < 0, \\ 1 & \text{if } y > 0. \end{cases}$$

Dirichlet boundary conditions equal to zero are again imposed. Under the considered velocity field the initial solution completes a full revolution in $2\pi$ seconds. The numerical solution is showed here after four revolutions, that is, $t = 8\pi$.

Two discretizations are considered: first, a regular mesh of size $h = 0.035$ and 1 370 elements with degree $p = 3$ (13 700 number of dof) and, second, a coarse mesh of size of size $h = 0.075$ and 493 elements with degree $p = 6$ (13 804 dof). Note that again, both discretizations reduce the number of degrees of freedom up to one order of magnitude, for instance than Kuzmin (2010) and Nadukandi (2011).

Figure 3.23 shows both approximations after four periods. The mesh is also plotted with the purpose of enhancing the sub-cell resolution of the method. Note that, although having comparable number of degrees of freedom, the higher order approximation is less diffuse at the contours. This is specially highlighted around the slotted

cylinder.

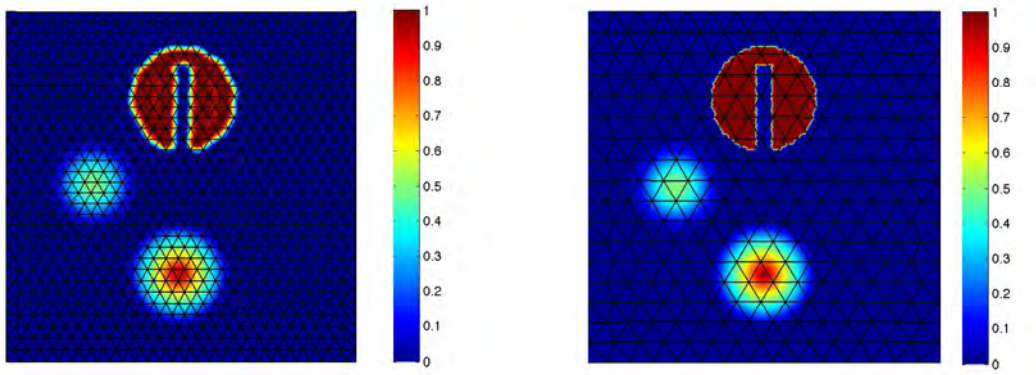


Figure 3.23: Linear advection of 3 body rotation: solution at time $t = 8\pi$.

The errors in $L_2$ norm within each element are displayed in Figure 3.24. As expected, the highest errors are concentrated on the areas where $u$ reaches its maximum value. The accuracy of the method is highlighted providing errors below $10^{-6}$.

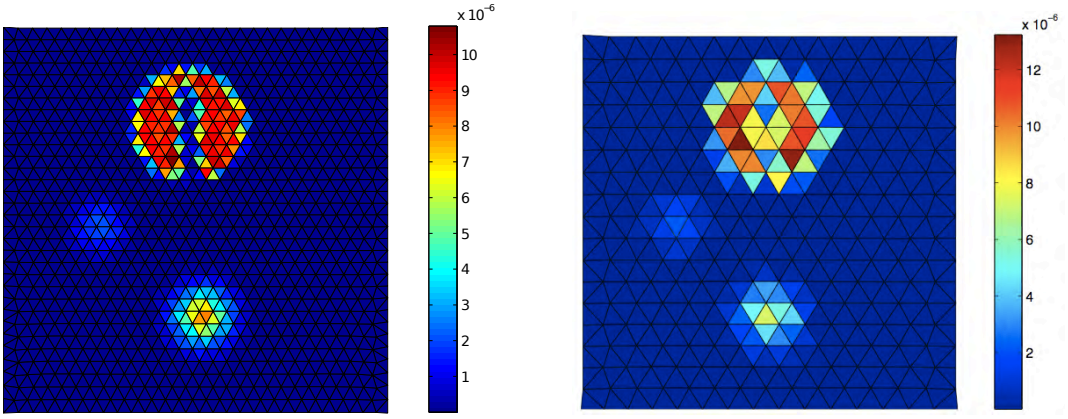


Figure 3.24: Linear advection of 3 body rotation: $L^2$-error within each element.

Cross and vertical sections along $y = 0.75$ and $x = 0.5$ are depicted in Figure 3.25 for both approximations. The exact solution of the problem is also plotted. The comparison on the cross section reveals some oscillations with the lower order approximation on both sides of the slotted cylinder. However, these small oscillations

typically arise in artificial diffusion methods and low order approximations, as pointed out in the one dimensional example of the transport of pulses, in Section 3.3.1. However, an excessive smearing in between both pulses (i.e, in the slotted cylinder) is also noticeable in this plot. In contrast, the high-order solution of degree $p = 6$ shows sharp profiles without propagating oscillations in the vicinity of the surface of the bodies, i.e, the high-gradients. Comparing the vertical section plot, the dissipative effect in the contours of the body is also highlighted for the third order approximation. Nonetheless, the contours of the cone match perfectly with the exact solution. Sixth order approximation overlaps the exact solution along the whole section.

An interesting result is observed by comparing the exact solution with respect the approximations between both sections. Whereas for the vertical section the profiles for the high-order approximation and the exact one clearly overlap, in the horizontal section slightly retardation effect between the exact and the approximated solutions, both for $p = 3$ and $p = 6$, is noticed. This dispersion error is not evident in the first period, but it increases as the solution advances in time. The explanation lies in the dissipative character of the upwind numerical fluxes along the streamlines, since at the vertical $x = 0.5$ the flow is only transported in the x-direction.

To sum up, on one hand this example again illustrates the good behavior of the method for simulating the advection of sharp profiles on unsteady problems. And on the other hand, it has been demonstrated that refined meshes are not always mandatory to obtain accurate results.

#### Supersonic flow past a bump

The next test considers the supersonic flow over a circular duct at free stream Mach number $M = 1.4$. This test has been introduced previously in Section 2.3.2. Same discretizations are proposed: a mesh of 1 452 elements with degree $p = 3$ and a mesh of 588 elements and degree $p = 5$, both structured and uniform, see Figure 2.14 of Chapter 2.

Figures 3.26 and 3.27 show the Mach number for the third and fifth order approximations, respectively. Both solutions are indistinguishable, even in the vicinity of

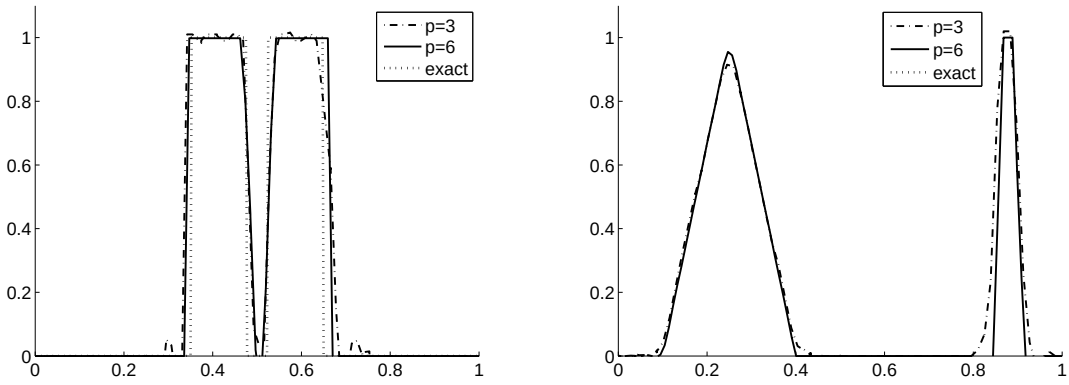


Figure 3.25: Linear advection of 3 body rotation: Section $y = 0.75$ (left) and $x = 0.5$ (right).

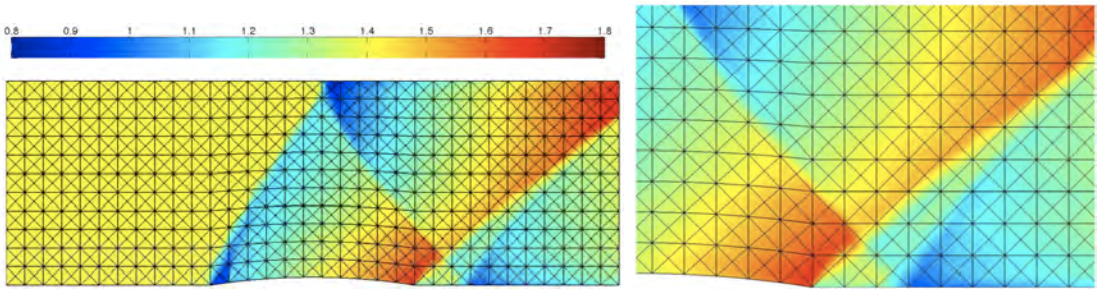

Figure 3.26: Supersonic flow past a bump with $M = 1.4$: Mach number for $p = 3$ and 1 452 elements.

the shocks. The shocks are well-resolved without significant dissipative effects and, as can be noticed in the zoomed section around the reflected shock, they also cross the elements maintaining its sharp profile.

More interesting conclusions can be extracted from the plot of artificial viscosity, depicted in Figure 3.28. First, excellent agreement between the artificial diffusion footprints and the $\alpha$-values distribution of Section 2.3.2 are obtained for both discretizations. Secondly, regarding the amount of viscosity introduced, never reaches the theoretical value $h/p$ for any of the discretizations ($h/p$ is equal to 0.0214 for the discretization of 1 452 elements and $p = 3$ and 0.0201 for the discretization of 588 elements and $p = 5$). In addition, it is important to stress that, as expected

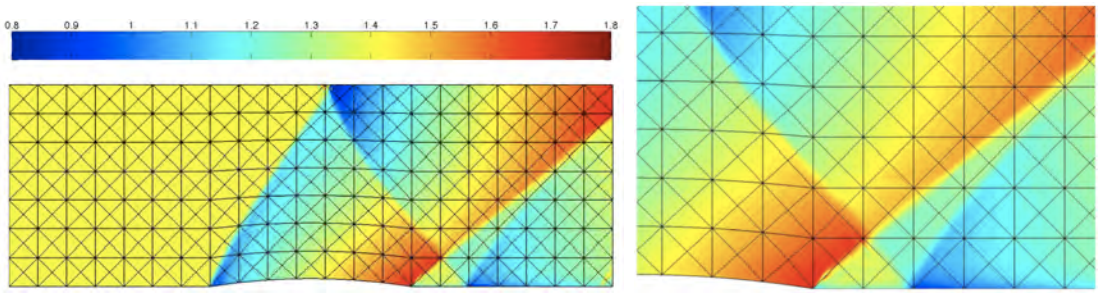


Figure 3.27: Supersonic flow past a bump with $M = 1.4$: Mach number for $p = 5$ and 588 elements.

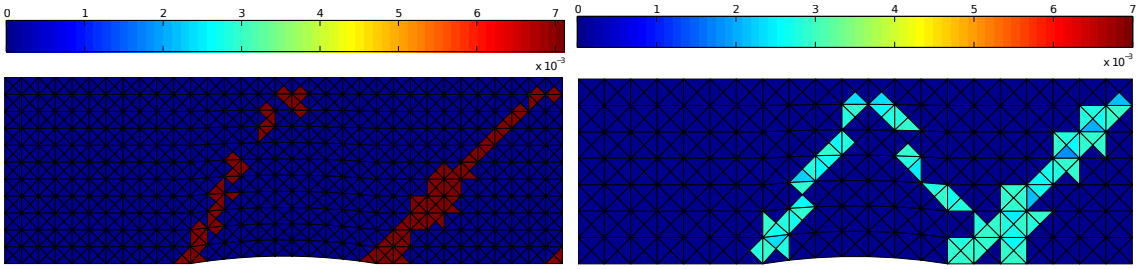


Figure 3.28: Supersonic flow past a bump with $M = 1.4$: amount of viscosity within each element.

and according to the one-dimensional results, high-order approximations require less amount of viscosity than lower-order ones.

In Figure 3.29 the Mach number distribution along an horizontal section (y = 0.4) is depicted for the approximation of degree $p = 5$. Moreover, the solution is compared with the solution obtained with the continuous-discontinuous shape function method presented in Chapter 2 for the same discretization. Both approaches give nearly coincident profiles with sharp shock profiles free of spurious oscillations. The only visible discrepancy is located at $x = 2.5$ where a slightly small perturbation in the artificial diffusion method arises. To further analyze the behavior of this method and compare it with the artificial diffusion one, an unsteady example is taken in the next section.

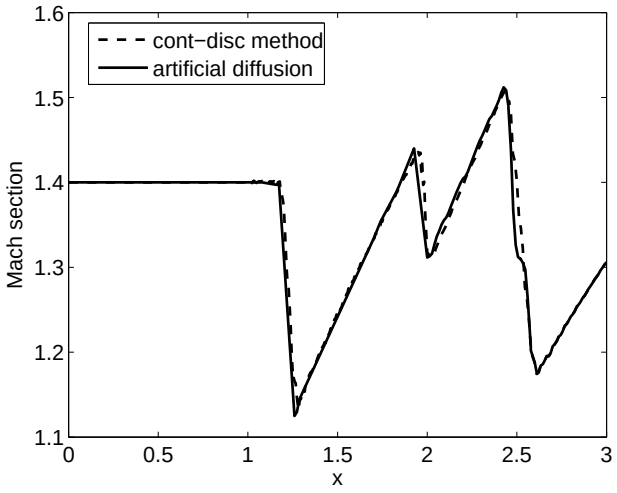


Figure 3.29: Supersonic flow past a bump with $M = 1.4$: section along $y = 0.4$ for approximations of degree $p = 5$ and a mesh of 588 elements.

### The forward-facing step problem

The following test is a classical example for testing the accuracy of numerical schemes for computing unsteady shock waves, see Emery (1968) and Woodward and Colella (1984), which was also introduced in Chapter 2, Section 2.3.2. It consists on a wind tunnel with a flat faced step at the bottom wall. Recall that this is an unsteady test. Solutions are shown at time $t = 4$ of the computations, where a special and complicated shock configuration is showed. Again, as with the continuous-discontinuous shape function method, no modification of the scheme, neither h-adaptation is applied towards the singular point of the problem, located at the corner of the step.

In order to analyze the influence of the approximation degree in the artificial viscosity method, solutions are computed with a uniform mesh of 1 728 elements and degrees $p = 4$ and $p = 5$. The mesh is depicted in Figure 3.30. Note that the number of degrees of freedom is significantly reduced upto one order of magnitude with respect to other classical approaches, like FV or DG with slope limiters (Luo et al. (2007) or Cockburn and Shu (1998b)).

Figure 3.31 shows the density profile for both approximations. The shock width of the fifth order approximation (bottom) is slightly thinner than the fourth order

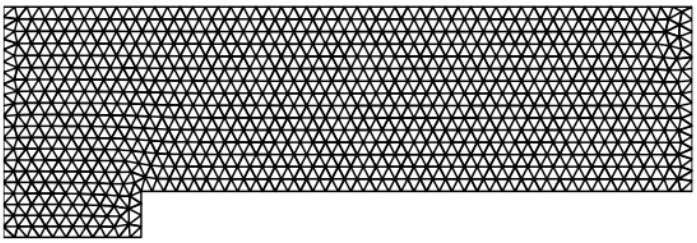

Figure 3.30: Forward Facing step Mach 3: computational mesh.

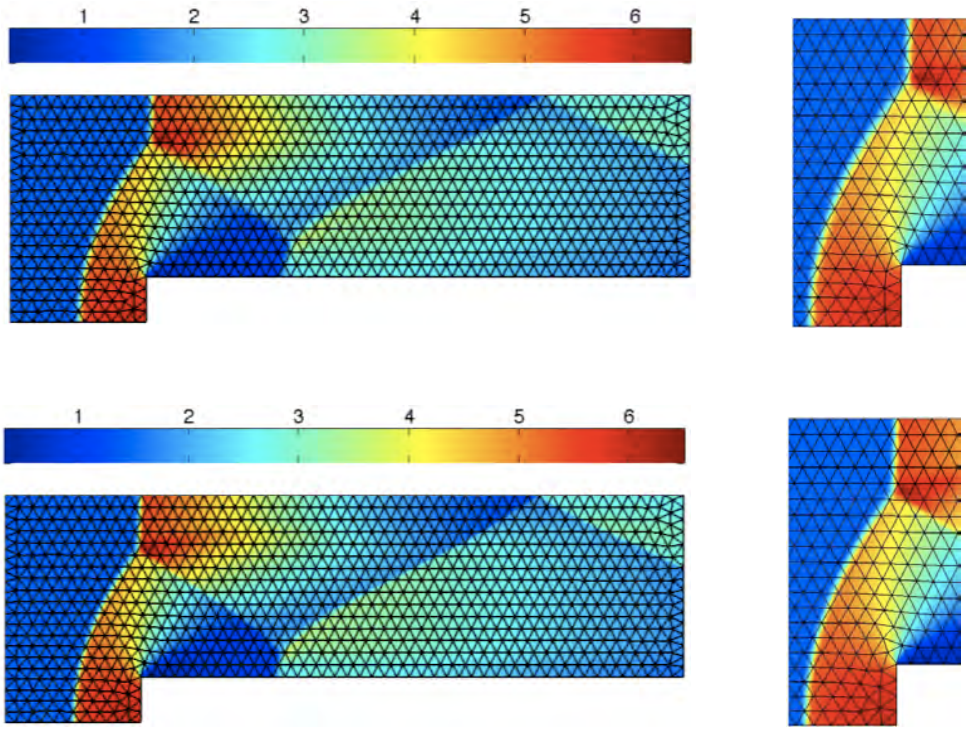


Figure 3.31: Forward Facing step Mach 3: density contours for $p = 4$ (top) and $p = 5$ (bottom) for a mesh of 1 728 elements.

one (top), as expected. Nonetheless, it can be noticed that in both cases the shock is captured inside the elements, showing thickness less than the element size. In order to emphasize this effect, a zoom of the bow shock is also depicted.

The map of the artificial viscosity added within each element is depicted in Figure 3.32 for both approximations. This example again confirms the fact that increasing the approximation degree, the amount of required viscosity decreases, since the value of the viscosity for the fifth order approximation is smaller the fourth order one. In

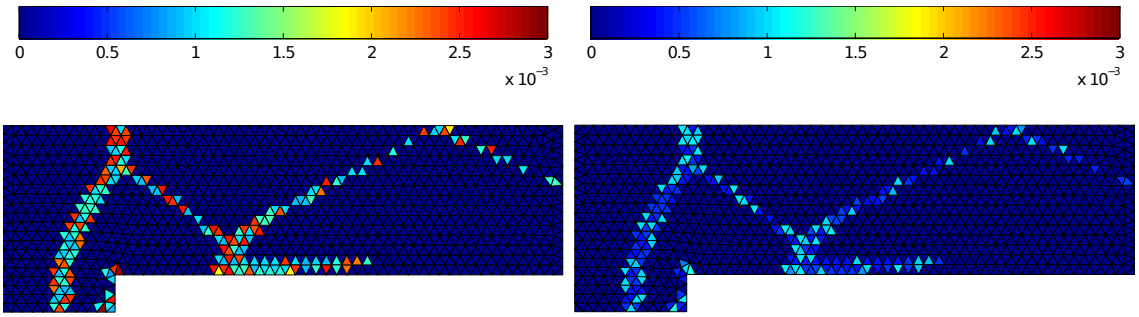


Figure 3.32: Forward Facing step Mach 3: artificial viscosity for $p = 4$ (top) and $p = 5$ (bottom) for a mesh of 1 728 elements.

both cases the amount of diffusion never reaches the theoretical value $h/p$, which for the $p = 4$ approximation is 0.0028 and for the $p = 5$ approximation is 0.0022. However, note that the degree of the approximation does not have influence in the effect of the sensor for high enough degrees of approximations, say $p \geq 3$, because the trace of the sensor for both discretizations approximately the same. Despite in some cases it is necessary the addition of viscosity across several elements through the shock, the shock profile remains thinner that the detected area. In other words, the footprint of the added viscosity is bigger than the shock width. The transition can occur within a single element, enhancing then the sub-cell resolution of higher-order artificial viscosity method. See for instance the strong bow shock in previous figure.

A comparison with the continuous-discontinuous method is studied next. The solution is now computed with the method described in Chapter 2 for the same discretizations ($p = 4$ and $p = 5$ and a mesh of 1 728 elements). First, the map of $\alpha$ values is depicted in Figures 3.33. Again, it coincides with the artificial diffusion map: in general, the elements with positive artificial diffusion agree with the elements in which $\alpha < 1$. However, since artificial diffusion decreases with the degree of approximation, there is no appreciable difference between the map of $\alpha$ values for the fourth order approximation and the one for the fifth order. The amount of diffusion introduced by the continuous-discontinuous shape function method comes from the interelement jumps, which are not easily measurable.

Finally, to get a more accurate comparison of both methods, a section of the

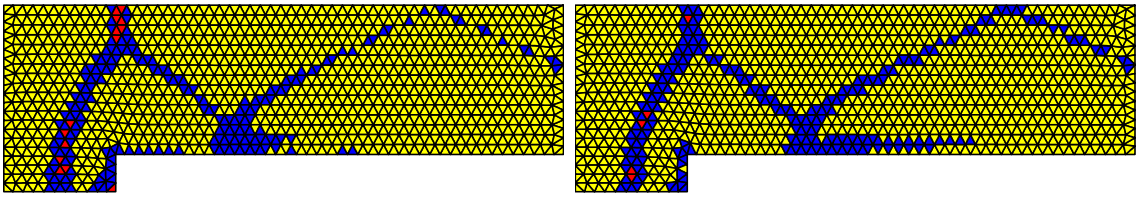

Figure 3.33: Forward Facing step Mach 3: $\alpha$ values for $p = 4$ and $p = 5$ for 1 728 elements, yellow for $\alpha = 1$, blue for $0 < \alpha < 1$, and red for $\alpha = 0$.

density distribution along $y = 0.2$ is plotted in Figure 3.34, with the fifth order approximations for both methods. There are almost no significative differences, except for the outflow boundary, where the solution is slightly more diffuse for the continuous-discontinuous shape functions method. The discontinuous nature of the approximation in elements where $\alpha < 1$ is the reason of this behavior. Recall that the accuracy in these elements is of the order $h/p$, while the artificial diffusion method reaches values below the theoretical $h/p$.

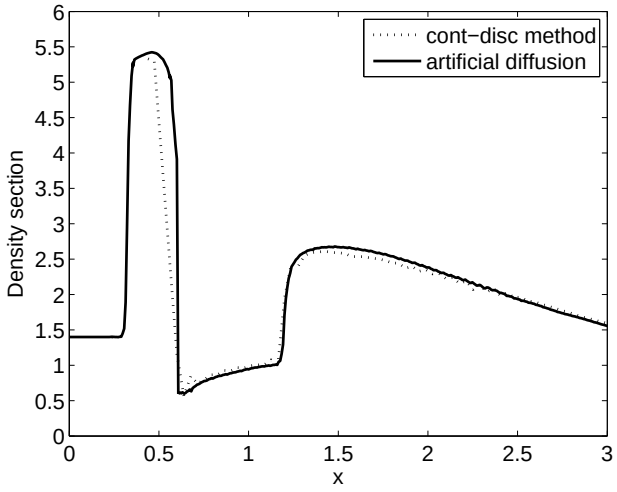


Figure 3.34: Forward Facing step Mach 3: section along $y = 0.2$ of the density profile.

# Chapter 4

# Summary and future developments

This thesis has presented two shock-capturing methods for high-order ($p > 1$) Discontinuous Galerkin methods. In the framework of high-order approximations for high-fidelity computations mesh adaptivity is almost mandatory to obtain highly accurate results. This recourse implies an important computational overhead, since DG methods duplicate nodes. The two methods try to overcome this problem and enhance the use of large high-order elements.

## 4.1 Summary and contributions

Two shock-capturing methods for high-order Discontinuous Galerkin have been presented in this thesis.

The first method exploits the stability introduced by numerical fluxes: it is based on one parameter which automatically modifies shape functions from continuous high-order ones to discontinuous ones, depending on the smoothness of the solutions. Discontinuous functions introduce jumps within the element. In these elements accuracy is reduced to order one, but shock width is of order $h/p$ (where $h$ the characteristic size of the elements and $p$ the order of the approximation). This novel approach does not require mesh adaption and does not increase the number of degrees of freedom. The method is highly robust: first, the parameter does not require tuning and basis functions within the element are chosen automatically. Second, it has been consis-

tently proved that small changes of the parameter don't affect the overall accuracy of the method. Extension of the method to three dimensions is straightforward. Two key ingredients are only required: the definition of constant shape functions basis and a general partition of the tetrahedra. For instance, standard FV shape functions and a Delaunay partition can be considered, respectively.

The second method is based on the classical techniques of introducing artificial viscosity to the original equations. The introduced viscosity is automatically adjusted for any pair $h, p$, with independence of the problem, neither the topology of the mesh. The main contribution of the method is that viscosity of the order $h^k$, with $1 \leq k \leq p$ is obtained. For high-order approximations this value is usually smaller than $h/p$. Locality of the method is highlighted: in general, artificial diffusion is only applied to the element containing the shock. Extension to higher dimensions is carried out by projection of the one-dimensional viscosity into characteristic directions within the triangle. Thus, it is easily computed for any mesh and any problem, with minimum computational overhead.

Both methods show that high-order elements require less degrees of freedom compared to low-order approximations when high accuracy is necessary. In both techniques, the obtained accuracy outperforms the order $h$ of slope limiting techniques and FV. Shocks thinner than the element size are obtained. Moreover, they can be implemented in the framework of either implicit, or explicit integrators.

Classical one and two-dimensional examples show the efficiency and accuracy of the methods. Although the bulk of this thesis focus on the compressible Euler equations, long time simulations of very sharp profiles are also highlighted.

Finally, artificial diffusion method is applied to a particular physical problem: the characterization of Homogeneus Surface Diffuson Model (HSDM) in 1D, which is defined by a set of convection-diffusion-reaction equations. This problem has been studied by many authors, see for instance Aizinger et al. (2000), Pérez-Foguet and Huerta (2005) and Sperlich et al. (2008), among others. The problem is highly nonlinear and the different flow regimes, as well as the physical parameters involved, make the analysis of the model behavior specially complicated. Appendix D is devoted to

analyze the behavior of the model within a wide range of dimensionless numbers and absorbers.

## 4.2 Future developments

This thesis has focused on the development of shock-capturing methods for high-order Discontinuous Galerkin methods. Although the examples show that both methods have proven to be well-suited for compressible flows and demonstrate high-accuracy on the results, there is still much work to do in order to exploit both methodologies and apply them to real engineering problems:

1. **Adaptivity.** Given a simple error estimation technique and under a high-order approximation rationale, p-adaptivity is easily implemented in Discontinuous Galerkin methods. p-adaption drastically reduces the number of degrees of freedom in the discontinuous scheme by means of p-refining only where more precision is needed. This procedure will result in accurate computations and uniform error distributions.

2. **3D extension.** The next task to be fulfilled is the 3D implementation of the methods. This will allow to simulate compressible flow in more complex physical situations, as would be for instance the design of airfoil wings. Actually, a 3D code for hyperbolic conservation laws (Euler equations) has been developed within the LaCàN (Laboratori de Càlcul Numèic) research group. The actual code solves the set of Euler equations in a subsonic flow.

3. **Development of implicit time integration schemes.** Incorporating implicit time integration schemes is a necessary step for 3D simulations. On one hand, an implicit scheme is preferred in order to solve multiple spatial scales, typical in compressible flow, without having to decrease dramatically the time step. On the other hand, implicit time integration schemes allow the possibility to achieve higher-order unconditionally stable methods.

4. **Parallelization of the code.** 3D simulations naturally turn into more involved computations, but also into an important increase of memory requirements and computational time. Actually this is still one of the most important computational overheads of numerical methods for simulating real problems. Parallelization will exploit the computational power of DG formulations, also permitting the use of meshes with an important number of degrees of freedom (either by increasing the number of elements or by increasing the degree of approximation). Parallelization can be dealt easily with OpenMP directions.

5. **Improvement of the sub-cell artificial viscosity.** An adaptive shock-capturing methodology for high-order Discontinuous Galerkin methods based on adding articial viscosity is presented in Chapter 3. The proposed method is able to capture sharp gradients and to preserve high-order accuracy. In the vicinity of shocks the approximation is not systematically reduced to first order, in fact, it is kept as high as possible. This is crucial because no adaption is required. An extension of the method allows to locate the shock within the element with a precision of order $h/p$, less than the element size. Piecewise constant viscosity within the element is then possible. Very preliminary results show that this approach might be beneficial. However further research is needed, considering also a smooth artificial viscosity, localized within the detected shock area.

6. **Introduction of the directionality in the artificial viscosity method.** The artificial viscosity in two dimensions is obtained by a linear combination of the viscosities. Each viscosity is obtained by projecting the two-dimensional elemental approximation along a direction within the triangle. A scalar value for the viscosity is considered in this thesis. However, a more sophisticated option consists on obtaining a tensorial viscosity, and hence, take into account the directionality of the shock. This option must be carefully studied. First ideas are given in the following discussion.

   The natural way to introduce artificial diffusion in two-dimensions is to consider

a diffusivity tensor $\boldsymbol{\varepsilon}$, consisting on a symmetric positive definite matrix which may vary in space, i.e.

$$\boldsymbol{\varepsilon} = \begin{pmatrix} \varepsilon_{11} & \varepsilon_{12} \\ \varepsilon_{21} & \varepsilon_{22} \end{pmatrix}$$

with $\varepsilon_{12} = \varepsilon_{21}$. Hence, symmetry requirement simplifies the problem to define only three values: $\varepsilon_{11}, \varepsilon_{12}$ and $\varepsilon_{22}$. Notice that in this way the complexity of the problem is reduced, since the number of unknowns equals the number of data (recall that for each element three viscosities, $\varepsilon_\alpha$, $\varepsilon_\beta$ and $\varepsilon_\gamma$, have been computed by the one-dimensional approach). Note that if the diffusivity tensor has the simplified form $\boldsymbol{\varepsilon} = \varepsilon \mathbf{I}$ where $\varepsilon$ is constant, then the artificial viscosity is just a single scalar value within each element. This approximation is the one used in this thesis, but due to the rude approach, it can be over-diffusive.

In order to introduce the directional behavior of the shock in the diffusivity tensor and assign the correct amount of artificial viscosity along each direction, the viscosity tensor is projected along each triangular direction, see Section 3.2.1. Viscosity along direction $\vec{\mathbf{d}\alpha}$ must be equal to the one-dimensional viscosity computed for projection $u_\alpha$, namely $\varepsilon_\alpha$. The following restrictions are obtained:

$$\begin{aligned} \boldsymbol{\varepsilon}\, \vec{\mathbf{d}\alpha} &= \varepsilon_\alpha\, \vec{\mathbf{d}\alpha} \\ \boldsymbol{\varepsilon}\, \vec{\mathbf{d}\beta} &= \varepsilon_\beta\, \vec{\mathbf{d}\beta} \\ \boldsymbol{\varepsilon}\, \vec{\mathbf{d}\gamma} &= \varepsilon_\gamma\, \vec{\mathbf{d}\gamma} \end{aligned} \tag{4.1}$$

Define an error function associated to these restrictions:

$$\text{err} = \| \boldsymbol{\varepsilon}\, \vec{\mathbf{d}_\mathbf{i}} - \varepsilon_i\, \vec{\mathbf{d}_\mathbf{i}} \|_2 = \sum_{i=\{\alpha,\beta,\gamma\}} (\boldsymbol{\varepsilon}\, \vec{\mathbf{d}_\mathbf{i}} - \varepsilon_i\, \vec{\mathbf{d}_\mathbf{i}})^2 \tag{4.2}$$

Numerically, solving the system of equations (4.1) is equivalent to minimize the error functions, adding the restriction of positivity of the diffusive matrix. Thus,

defining $f(\varepsilon_{11}, \varepsilon_{22}, \varepsilon_{12}) = \sum_{i=\{\alpha,\beta,\gamma\}} (\boldsymbol{\varepsilon}\, \vec{\mathbf{d}}_\mathbf{i} - \varepsilon_i\, \vec{\mathbf{d}}_\mathbf{i})^2$, formally, the problem is stated as follows:

$$\begin{aligned} &\min_{\varepsilon_{11},\varepsilon_{22},\varepsilon_{12}} f(\varepsilon_{11}, \varepsilon_{22}, \varepsilon_{12}) \\ &\varepsilon_{11}\varepsilon_{22} - \varepsilon_{12}^2 \geq 0 \end{aligned} \tag{4.3}$$

which is nothing than a minimization problem with nonlinear restrictions.

7. **Application to other sets of equations.** The tests cases contained in this thesis were limited to the compressible set of Euler equations and scalar convection-dominated problems for long time simulations. However, complex hypersonic flow cases, compressible Navier-Stokes equations, considering also the introduction of turbulent flows, need to be explored.

# Appendix A

# Slope limiting techniques

One of the older and more successful classes of shock capturing methods is the Total Variation Diminishing (TVD) approach. The concept of TVD was introduced by Harten (1983) by means of non-linear operators, called either flux limiters or slope limiters. Godunov (1954) also established that any linear TVD scheme can be first-order accurate. However, this statement does not exclude the possibility of having nonlinear TVD shcemes that are second order accurate. Actually, these schemes were first introduced by van Leer (1974, 1977a,b, 1979) for the Finite Difference and Finite Folume method with the aim of improving stability properties. Basically, Total Variation Diminishing and Total Variation Bounded (TVB) methods prevent the creation of local extrema in the solution and hence, the creation of non-physical oscillations. To accomplish it the introduction of flux limiters or slope limiters is required. The term flux limiter is used when the limiter acts on system fluxes, and slope limiter is used when the limiter acts on system states. However they both have the same mathematical form, and both have the effect of limiting the solution gradient near shocks or discontinuities. The main drawback of these schemes is that they are, at most, second-order accurate.

For DG, Cockburn and Shu (1989); Cockburn et al. (1989, 1990); Cockburn and Shu (1998b) developed TVD and TVB schemes for Discontinuous Galerkin methods. The method is based on a Runge-Kutta type discretization in time in combination with slope limiters that maintain the formal accuracy of the scheme. This method is commonly referred to as RKDG and it has become popular in the DG community,

see for instance Biswas et al. (1994), Burbeau et al. (2001) or Hoteit et al. (2002).

This appendix details the classical generalized slope limiter by Cockburn and Shu (2001) for the one-dimensional and multidimensional case. The extension by Biswas et al. (1994) introduced in Chapter 3 relies on the limiter here detailed.

## A.1 The one-dimensional limiting operator

The TVD Runge-Kutta Disconinuous Galerkin method (Cockburn and Shu (1989)) ensures stable solutions for a general nonlinear hyperbolic conservation law. One of the key ingredients of the method is the construction of a nonlinear operator, namely the slope limiter $\Lambda\Pi_h$, whose aim is to enforce nonlinear stability by preventing the approximate solution at any point within the element from having local extrema.

For simplicity, the approximate solution is expanded in terms of orthogonal Legendre polynomial, within each element $I_e$ (for all $e = 1, \ldots, \mathrm{n_{el}}$) the approximation of $u$ may be written as

$$u^e(x,t) = \sum_{i=0}^{p} c_i^e(t)\ P_i(x) \tag{A.1}$$

where the $P_i$ are the Legendre polynomials, normalized such that $P_i(1) = 1$, and the degrees of freedom $c_i^e$ are the so called modal coefficients.

The limiter is initially designed for linear approximations, i.e, $p = 1$. The idea is to decrease the gradient of the approximate solution such that at any point within the element the value of the solution is kept within the range spanned by the neighboring solution averages. Mean value within the element is conserved. Figure A.1 illustrates the limiting.

The coefficient $c_1^e$ of (A.1) is replaced by

$$\tilde{c}_1^e = \mathrm{minmod}\big(c_1^e, c_0^{e+1} - c_0^e, c_0^e - c_{i-1}^{e-1}\big),$$

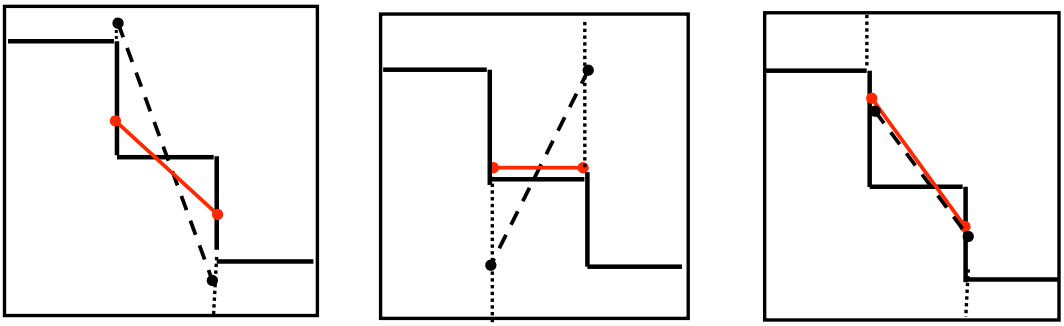

Figure A.1: Illustration of one-dimensional slope limiter.

with the usual definition:

$$\text{minmod}\big(a_1, a_2, a_3\big) = \begin{cases} s \min\limits_{1\le n\le 3} |a_n| & \text{if } s = \text{sign}(a_1) = \text{sign}(a_2) = \text{sign}(a_3), \\ 0 & \text{otherwise.} \end{cases}$$

Since conservation of mass is imposed within each element, coefficient $c_0^e$ is kept constant, that is, $c_0^e = \tilde{c}_0^e$.

It is possible to obtain a Total Variation Bounded scheme by modifying the minmod function to obtain second-order accurate solution at local extrema. The modification consists on introducing a a constant $M$ which is an upper bound of the absolute value of the second-order derivative of the solution at local extrema. Then, the minmod function is modified in the following way,

$$\tilde{m}\big(a_1, a_2, a_3\big) = \begin{cases} a_1 & \text{if } |a_1| \le M(\Delta x)^2, \\ \text{minmod}\big(a_1, a_2, a_3\big) & \text{otherwise.} \end{cases}$$

For high-order approximations, say $p \ge 2$, Cockburn and Shu (1989) suggest to set $c_i^e = 0$ for $i = 2, \ldots, \text{n}_{\text{en}}(p)$. In other words, in elements where limiting is necessary, the solution is locally truncated and the order of the approximation is reduced to a linear one. While preventing spurious oscillations, this procedure tends to flatten excessively the solution. Higher-order limiters have been proposed to overcome this drawbacks, see for instance the interesting approaches by Biswas et al. (1994) or

Krivodonova (2007).

## A.2 The multi-dimensional slope limiter

The adaptation of the method to multi-dimensional meshes is a bit more involved. The main problem is referred to stability, which is not yet demonstrated for higher dimensions. Unstructured meshes also raise numerous problems. In fact, for general triangular meshes slope-limiting operators are only constructed on piecewise linear functions. Along this section, in order to simplify the exposition and understating of the technique, the notation proposed by Cockburn and Shu (1998a) is used.

Guided by the theoretical studies of the one-dimensional slope limiter, the multi-dimensional extension of the operator $\Lambda\Pi_h$ proposed by Cockburn and Shu (1998a) rely on the assumption that spurious oscillations are present in a polynomial approximation only if they are present in its linear part, which is obtained by projecting the approximation into the space of piecewise linear functions. Thus, to compute the multidimensional slope limiter, it is first necessary to compute the projection of any polynomial approximation of degree $p$ over the space of linear polynomials. If no limiting is necessary, then $\Lambda\Pi_h(\mathbf{U}^e) = \mathbf{U}^e$ remains a $p$th degree approximation. Otherwise, the higher order part of the expansion of the numerical approximation is chopped off and hence, the high-order approximation is reduced to a linear one and the limiting operator is applied.

**Remark A.1.** *The assumption that oscillations are only present in the linear part of the approximation is only based on numerical results. A theoretical justification is still an open problem.*

Let $\mathcal{T}_h$ be a triangulation of the computational domain $\Omega$ such that

$$\bar{\Omega} = \bigcup_{e=1}^{\mathrm{n_{el}}} \bar{\Omega}_e \quad \text{such that} \quad \Omega_e \bigcap \Omega_l = \emptyset \quad \text{for} \quad e \neq l$$

and $\mathbf{U}^e$ the approximate solution in element $\Omega_e$. Then, the nonlinear slope limiter $\Lambda\Pi_h$ satisfies the following properties:

1. Accuracy: If $\mathbf{U}^e$ is linear then $\Lambda\Pi_h(\mathbf{U}^e) = \mathbf{U}^e$.

2. Conservation of mass: for every element $\Omega_e$ of the triangulation $\mathcal{T}_h$, it is satisfied

$$\int_{\Omega_e} \Lambda\Pi_h(\mathbf{U}^e)\, d\Omega = \int_{\Omega_e} \mathbf{U}^e\, d\Omega.$$

3. Slope limiting: on each element $\Omega_e$ of $\mathcal{T}_h$, the gradient of $\Lambda\Pi_h(\mathbf{U}^e)$ is not bigger than that of $\mathbf{U}^e$.

Despite the choice of basis and degrees of freedom does not affect the algorithm, a suitable choice may simplify the implementation and calculation. An approximation of degree $p$, $\mathbf{U}^e \in \left[\mathcal{P}^p(\Omega_e)\right]^{\mathrm{n_{sd}}}$, is expressed in terms of the hierarchical and orthogonal Koornwinder basis function, see Koornwinder (1992), as

$$\mathbf{U}^e(\boldsymbol{x}, t) = \sum_{i=1}^{\mathrm{n_{en}}(p)} \boldsymbol{U}_i^e(t)\varphi_i(\boldsymbol{x}) \tag{A.2}$$

where $\mathrm{n_{en}}(p)$ is the number of element nodes (i.e, the number of degrees of freedom) for an approximation of degree equal to $p$. For this set of basis functions, the mean value of $\mathbf{U}^e$ on the element $\Omega_e$ is reduced to the degree of of freedom associated with the first function of the basis, that is

$$\boldsymbol{U}_1^e = \bar{\mathbf{U}}^e = \frac{1}{\mathrm{meas}(\Omega_e)} \int_{\Omega_e} \mathbf{U}^e\, d\Omega$$

To construct the multidimensional slope limiter the following geometrical property is advocated:

Consider a triangle $\Omega_e$ with neighbors $\Omega_{e,j}$ and barycenter denoted by $b_0$, see Figure A.2. The midpoint of edge $\Gamma_j = \bar{\Omega}_e \bigcap \bar{\Omega}_{e,j}$ is denoted by $m_j$ and the barycenter of

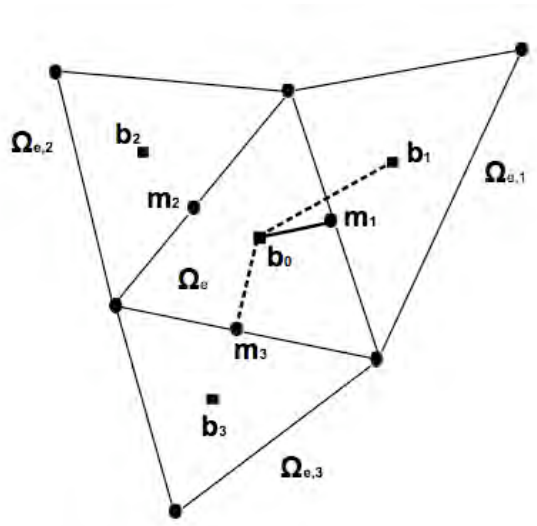


Figure A.2: Notations and illustration of multi-dimensional slope limiter.

triangle $\Omega_{e,j}$ is denoted by $b_j$ for $j = 1, 2, 3$. There exist nonnegative coefficients $\alpha_j$ and $\beta_j$ for $j = 1, 2, 3$ such that

$$
\begin{aligned}
m_1 - b_0 &= \alpha_1(b_1 - b_0) + \beta_1(b_2 - b_0) \\
m_2 - b_0 &= \alpha_2(b_2 - b_0) + \beta_2(b_3 - b_0) \\
m_3 - b_0 &= \alpha_3(b_3 - b_0) + \beta_3(b_1 - b_0)
\end{aligned}
$$

Since in an arbitrary element $\Omega_{e,l}$ the mean value of an approximation $\mathbf{U}^e$ can be computed by evaluating it at the barycenter of the triangle, that is, $\bar{\mathbf{U}}^{e,l} = \mathbf{U}^{e,l}(b_l)$, for any linear approximation $\mathbf{U}^e$ it is satisfied:

$$
\begin{aligned}
\mathbf{U}^e(m_1) - \bar{\mathbf{U}}^e &= \alpha_1(\bar{\mathbf{U}}^{e,1} - \bar{\mathbf{U}}^e) + \beta_1(\bar{\mathbf{U}}^{e,2} - \bar{\mathbf{U}}^e) \\
\mathbf{U}^e(m_2) - \bar{\mathbf{U}}^e &= \alpha_2(\bar{\mathbf{U}}^{e,2} - \bar{\mathbf{U}}^e) + \beta_2(\bar{\mathbf{U}}^{e,3} - \bar{\mathbf{U}}^e) \\
\mathbf{U}^e(m_2) - \bar{\mathbf{U}}^e &= \alpha_3(\bar{\mathbf{U}}^{e,3} - \bar{\mathbf{U}}^e) + \beta_3(\bar{\mathbf{U}}^{e,1} - \bar{\mathbf{U}}^e)
\end{aligned}
$$

The purpose of limiting is to obtain a solution $\mathbf{U}^e$ such that

$$\min(\bar{\mathbf{U}}^e, \bar{\mathbf{U}}^{e,1}, \bar{\mathbf{U}}^{e,2}, \bar{\mathbf{U}}^{e,3}) \leq \mathbf{U}^e(\boldsymbol{x}) \leq \max(\bar{\mathbf{U}}^e, \bar{\mathbf{U}}^{e,1}, \bar{\mathbf{U}}^{e,2}, \bar{\mathbf{U}}^{e,3})$$

Keeping this concept in mind, the following quantities are defined:

$$\begin{aligned}
\Delta_1 &= \text{minmod}\Big(\mathbf{U}^e(m_1) - \bar{\mathbf{U}}^e, \nu(\alpha_1(\bar{\mathbf{U}}^{e,1} - \bar{\mathbf{U}}^e) + \beta_1(\bar{\mathbf{U}}^{e,2} - \bar{\mathbf{U}}^e))\Big) \\
\Delta_2 &= \text{minmod}\Big(\mathbf{U}^e(m_2) - \bar{\mathbf{U}}^e, \nu(\alpha_2(\bar{\mathbf{U}}^{e,2} - \bar{\mathbf{U}}^e) + \beta_2(\bar{\mathbf{U}}^{e,3} - \bar{\mathbf{U}}^e))\Big) \\
\Delta_3 &= \text{minmod}\Big(\mathbf{U}^e(m_3) - \bar{\mathbf{U}}^e, \nu(\alpha_3(\bar{\mathbf{U}}^{e,3} - \bar{\mathbf{U}}^e) + \beta_3(\bar{\mathbf{U}}^{e,1} - \bar{\mathbf{U}}^e))\Big)
\end{aligned}$$

where $\nu > 1$ (Cockburn and Shu (1998b) set $\nu = 1.5$ in their numerical experiments).

For simplicities on the procedure, a modification of (A.2) is introduced,

$$\tilde{\mathbf{U}}^e(\boldsymbol{x}, t) = \sum_{i=1}^{3} \tilde{\boldsymbol{U}}_i^e(t)\varphi_i(\boldsymbol{x}) - \bar{\mathbf{U}}^e$$

Then, the limited solution is defined as

$$\Lambda\Pi_h(\mathbf{U}^e)(\boldsymbol{x}, t) = (\boldsymbol{U}_1^e(t) + \tilde{\boldsymbol{U}}_1^e(t))\varphi_1(\boldsymbol{x}) + \tilde{\boldsymbol{U}}_2^e(t)\varphi_2(\boldsymbol{x}) + \tilde{\boldsymbol{U}}_3^e(t)\varphi_3(\boldsymbol{x})$$

with

$$\begin{aligned}
\tilde{\boldsymbol{U}}_1 &= \frac{1}{3}(\Delta_1 + \Delta_2 + \Delta_3) \\
\tilde{\boldsymbol{U}}_2 &= -\frac{1}{3}(2\Delta_1 - \Delta_2 - \Delta_3) \\
\tilde{\boldsymbol{U}}_3 &= \frac{1}{2}(\Delta_2 - \Delta_3)
\end{aligned}$$

In order to preserve conservation of mass within each element, $\Delta_i$ quantities must

satisfy $\sum_{i=1}^{3} \Delta_i = 0$. Otherwise, the following modification on $\Delta_i$ must be performed:

$$\hat{\Delta}_i = \theta^+ \max(0, \Delta_i) - \theta^- \max(0, -\Delta_i) \quad \text{for } i = 1, 2, 3$$

with

$$\theta^+ = \min\left(1, \sum_{i=1}^{3} \max(0, -\Delta_i) \Big/ \sum_{i=1}^{3} \max(0, \Delta_i)\right)$$
$$\theta^- = \min\left(1, \sum_{i=1}^{3} \max(0, \Delta_i) \Big/ \sum_{i=1}^{3} \max(0, -\Delta_i)\right)$$

# Appendix B

# The Local Discontinuous Galerkin method

For the sake of simplicity, the LDG method is described for a general scalar hyperbolic conservation law. Consider the following boundary value problem

$$\begin{aligned} \frac{\partial u}{\partial t} + \boldsymbol{\nabla} \cdot \mathbf{F}(u) - \boldsymbol{\nabla} \cdot (\nu \boldsymbol{\nabla} u) = 0 \qquad & \text{in } \Omega,\, t > 0 \\ u = u_D \quad & \text{on } \partial\Omega_D \\ (\nu \boldsymbol{\nabla} u) \cdot \mathbf{n} = h \qquad & \text{on } \partial\Omega_N \end{aligned} \tag{B.1}$$

where $\Omega$ is a bounded domain in $\mathbb{R}^{\mathrm{n_{sd}}}$ with boundary $\partial\Omega = \partial\Omega_D \cup \partial\Omega_N$ and $\nu$ is the viscosity. Here, for simplicity on the notation, the viscosity $\nu$ is considered constant in space and time.

Introducing the variable $\boldsymbol{\sigma} = \boldsymbol{\nabla} u$ the previous problem may be rewritten as a system of first-order equations:

$$\begin{aligned} \frac{\partial u}{\partial t} + \boldsymbol{\nabla} \cdot \mathbf{F}(u) - \boldsymbol{\nabla} \cdot \boldsymbol{\sigma} = 0 \qquad & \text{in } \Omega,\, t > 0 \\ \boldsymbol{\sigma} - \nu \boldsymbol{\nabla} u = \mathbf{0} \qquad & \text{in } \Omega,\, t > 0 \\ u = u_D \quad & \text{on } \partial\Omega_D \\ \boldsymbol{\sigma} \cdot \mathbf{n} = h \qquad & \text{on } \partial\Omega_N \end{aligned}$$

where $\mathbf{n}$ is the outward unit normal to the boundary of $\Omega$.

Recall the function space $\mathcal{V}^h$ defined in Section 1.4.2 and introduce a new space $\boldsymbol{\Sigma}^h$, namely

$$\mathcal{V}^h = \{v \in \mathcal{L}^2(\Omega) |\, v_{|\Omega_e} \in \mathcal{P}^p(\Omega_e),\ \forall \Omega_e\}$$
$$\boldsymbol{\Sigma}^h = \{\boldsymbol{\tau} \in [\mathcal{L}^2(\Omega)]^{\mathrm{n_{sd}}} |\, \boldsymbol{\tau}_{|\Omega_e} \in [\mathcal{P}^p(\Omega_e)]^{\mathrm{n_{sd}}},\ \forall \Omega_e\}$$

Consider the general triangulation (1.5) of the domain $\Omega$. The LDG formulation in an arbitrary element $\Omega_e$ reads: find $u_h \in \mathcal{V}^h$ and $\boldsymbol{\sigma}_h \in \boldsymbol{\Sigma}^h$ such that for all $v \in \mathcal{V}^h$ and $\boldsymbol{\tau} \in \boldsymbol{\Sigma}^h$

$$\int_{\Omega_e} v \frac{\partial u_h}{\partial t}\, d\Omega - \int_{\Omega_e} \boldsymbol{\nabla} v \cdot \mathbf{F}(u_h)\, d\Omega + \int_{\partial\Omega_e} v \widehat{F}_{n_e}\, d\Gamma + \int_{\Omega_e} \boldsymbol{\nabla} v \cdot \boldsymbol{\sigma}_h\, d\Omega - \int_{\partial\Omega_e} v\, (\hat{\boldsymbol{\sigma}}_h \cdot \mathbf{n})\, d\Gamma = 0 \tag{B.4a}$$

$$\int_{\Omega_e} \boldsymbol{\tau} \cdot \boldsymbol{\sigma}_h\, d\Omega + \int_{\Omega_e} (\boldsymbol{\nabla} \cdot \boldsymbol{\tau}) u_h\, d\Omega - \int_{\partial\Omega_e} \boldsymbol{\tau} \cdot (\hat{u}\mathbf{n})\, d\Gamma = 0 \tag{B.4b}$$

for every element $e = 1, \ldots, \mathrm{n_{el}}$ and $t > 0$.

The LDG formulation introduces two additional numerical fluxes $\hat{\boldsymbol{\sigma}}_h$ and $\hat{u}$ to the DG discretization. They can be seen as approximations of numerical traces of $\boldsymbol{\sigma}_h$ and $g(u_h)$ on the boundary of element $\Omega_e$. To complete LDG formulation it remains to specify these numerical fluxes and the boundary conditions. Some definitions and notation are first introduced: consider two adjacent elements, $\Omega_e$ and $\Omega_l$ such that $\Gamma = \Omega_e \cap \Omega_l$. The *jump* $[\![\cdot]\!]$ and *mean* $\{\cdot\}$ operators are defined along the interface $\Gamma$ using values from the elements to the left and to the right of the interface and are also extended along the exterior boundary, namely

$$[\![u\mathbf{n}]\!] = \begin{cases} u_e\mathbf{n}_e + u_l\mathbf{n}_l & \text{on } \Gamma \\ u\mathbf{n} & \text{on } \partial\Omega \end{cases} \qquad \{u\} = \begin{cases} k_e u_e + k_l u_l & \text{on } \Gamma \\ u & \text{on } \partial\Omega \end{cases} \quad \text{for scalars}$$

$$[\![\boldsymbol{\sigma}\cdot\mathbf{n}]\!] = \begin{cases} \boldsymbol{\sigma}_e \cdot \mathbf{n}_e + \boldsymbol{\sigma}_l \cdot \mathbf{n}_l & \text{on } \Gamma \\ \boldsymbol{\sigma} \cdot \mathbf{n} & \text{on } \partial\Omega \end{cases} \qquad \{\boldsymbol{\sigma}\} = \begin{cases} k_e\boldsymbol{\sigma}_e + k_l\boldsymbol{\sigma}_l & \text{on } \Gamma \\ \boldsymbol{\sigma} & \text{on } \partial\Omega \end{cases} \quad \text{for vectors}$$

Usually $k_e = k_l = 1/2$ but, in general, these two scalars are only required to verify $k_e + k_l = 1$, see Hansbo and Hansbo (2004). Other definitions of the jump operator have been proposed in the literature. For instance, Arnold et al. (2001) define $[\![u]\!] = u_e\mathbf{n}_e + u_l\mathbf{n}_l$ for scalars, and $[\![\boldsymbol{\sigma}]\!] = \boldsymbol{\sigma}_e \cdot \mathbf{n}_e + \boldsymbol{\sigma}_l \cdot \mathbf{n}_l$ for vectors. Notice that this definition requires different spaces for the input and the output: the jump of a scalar is a vector, and the jump of a vector is a scalar. Other definitions, like the one proposed by Cockburn and Shu (1998b), require the selection of a privilege normal and define $[\![u]\!] = u_e - u_l$ for scalars and $[\![\boldsymbol{\sigma}]\!] = \boldsymbol{\sigma}_e - \boldsymbol{\sigma}_l$ for vectors, assuming $\mathbf{n} = \mathbf{n}_e$. In this thesis, the proposed definition is not dependent on the selection of a normal sign, and it is coherent with the input and output spaces, avoiding ambiguous notations. For extension to tensor products see Montlaur et al. (2008).

With these definitions, the numerical fluxes $\hat{\boldsymbol{\sigma}}_h$ and $\hat{u}_h$ are defined as:

$$\begin{aligned} \hat{\boldsymbol{\sigma}}_h &= \{\boldsymbol{\sigma}_h\} + \mathbf{C_{12}}[\![\boldsymbol{\sigma}_h \cdot \mathbf{n}]\!] - C_{11}[\![u_h\mathbf{n}]\!] \\ \hat{u}_h &= \{u_h\} - \mathbf{C_{12}} \cdot [\![u_h\mathbf{n}]\!] \end{aligned}$$

for the interior faces, and

$$\hat{\boldsymbol{\sigma}}_h = \begin{cases} \boldsymbol{\sigma}_h - C_{11}(u_h - u_D)\mathbf{n} & \text{on } \partial\Omega_D, \\ h\mathbf{n}, & \text{on } \partial\Omega_N \end{cases} \qquad \hat{u} = \begin{cases} u_D & \text{on } \partial\Omega_D, \\ u_h & \text{on } \partial\Omega_N \end{cases}$$

for the boundary faces.

Note that definition of the LDG method involves two parameters, $C_{11}$ and $\mathbf{C_{12}}$. The former, $C_{11}$, is a non-negative constant and it acts as a penalty parameter . The latter, $\mathbf{C_{12}}$ is a vector of $\mathbb{R}^{n_{sd}}$ which is determined for each interior face. An

appropriate selection of $\mathbf{C_{12}}$ provides a near local stencil, see Sherwin et al. (2006). In this thesis, $\mathbf{C_{12}}$ is chosen following this local approach and $C_{11} = 0$ in order to avoid extra stabilization.

# Appendix C

# Shock-capturing with B-Splines

This chapter is devoted to investigate the use of B-splines basis functions for shock-capturing problems. Excellent references are available with presentations of B-splines, see for instance Piegl et al. (1995) and Sevilla et al. (2008).

## C.1 Motivation for the use of B-splines

For many years there has been an important research pursuing the relation between monotonicity and high-order methods, see LeVeque (1992) for a review of these methods. However, it is well known by the Godunov's order barrier theorem, Godunov (1954) that monotone methods are only first-order accurate. Here the idea of Hughes et al. (2005) is recovered. In their work, they investigate the ability of the isogeometric approach, in conjunction with some stabilizing technique, to solve problems involving high gradients and shocks. The artificial diffusion technique proposed in of Chapter 3 is used as stabilization approach, but employing the basis function defined by B-splines instead of the standard Lagrange.

B-spline polynomials have some distinctive properties that could be relevant in the application of shock-capturing problems. In particular, they possess the variation diminishing property, which ensures that the approximation with B-splines of a monotone function is still monotone. One of the goals of this chapter is to exploit this property. Moreover, the knot insertion procedure, also typical of B-splines, pro-

vides a tool to enrich the solution space by increasing the number of functions of the basis, but without changing the order of the approximation. The flexibility between elements of DG methods permits just to enrich with extra knots the elements where more resolution is needed.

In the next sections basic concepts on B-splines and a preliminary approach to the approximation of shocks are first introduced. Then the modification of the artificial diffusion method withB-splines basis functions is explained in detail. Finally, some standard numerical tests in one-dimension are discussed and also compared with the use of standard Lagrangian basis functions.

## C.2 Basic concepts on B-splines

Following Sevilla (2009), a $p$th-degree B-spline curve (or approximation) is a piecewise rational function defined in parametric form as

$$u(\lambda) = \sum_{i=1}^{\mathrm{n_{cp}}+1} C_{i,p}(\lambda) P_i \qquad 0 \leq \lambda \leq 1 \tag{C.1}$$

where $\{P_i\}$ are the coordinates of the $\mathrm{n_{cp}} + 1$ degrees of freedom or *control points* and $\{C_{i,p}(\lambda)\}$ are the normalized B-spline basis functions of degree $p$. The definition of these basis functions is recursive in $k$. For degree equal to 0, functions $C_{i,0}$ are piecewise constant functions,

$$C_{i,0}(\lambda) = \begin{cases} 1 & \text{if } \lambda \in [\lambda_i, \lambda_{i+1}[ \\ 0 & \text{elsewhere,} \end{cases}$$

and for $k = 1 \ldots p$,

$$C_{i,k}(\lambda) = \frac{\lambda - \lambda_i}{\lambda_{i+k} - \lambda_i} C_{i,k-1}(\lambda) + \frac{\lambda_{i+k+1} - \lambda}{\lambda_{i+k+1} - \lambda_{i+1}} C_{i+1,k-1}(\lambda)$$

where $\lambda_i$, for $i = 0 \dots \mathrm{n_k}$, are the *knots* or *breakpoints*, which are assumed ordered $0 \leq \lambda_i \leq \lambda_{i+1} \leq 1$. They form the so called *knot vector*

$$\Lambda = \{\underbrace{0, \dots, 0}_{p+1}, \lambda_{p+1}, \dots, \lambda_{\mathrm{n_k}-p-1}, \underbrace{1, \dots 1}_{p+1}\},$$

which uniquely describes the B-spline basis functions. A number of coinciding knots is referred to as multiplicity of the knot. The multiplicity is directly related to the number of continuous derivatives of the basis functions: in general,basis functions of order $p$ have $p-1$ continuous derivatives. If a knot is has multiplicity of order $m$ (i.e, it is repeated $m$ times in the knot vector), then the number of continuous derivatives decreases by $m$. Control points $\mathrm{n_{cp}} + 1$, and knots, $\mathrm{n_k} + 1$, are related to the degree of the parametrization, $p$, by the relation $\mathrm{n_k} = \mathrm{n_{cp}} + p + 1$. See Piegl et al. (1995) for more details.

### C.2.1 Basic properties of B-splines

Important properties of B-splines basis functions are:

1. $C_{i,p}(\lambda) = 0$ outside the interval $[\lambda_i, \lambda_{i+p+1})$ (local support property).
2. They constitute a partition of unity. That is: $\forall\lambda$, $\sum_{i=1}^{\mathrm{n}_{cp}} C_{i,p}(\lambda) = 1$
3. $C_{i,p}(\lambda) \geq 0$, $\forall i, p$ and $\lambda$ (nonnegativity).

among many others.

The next properties of an approximation with B-splines are derived from the definition of the basis and from the previous properties:

1. The approximation (C.2) has derivatives of order $p-1$ in the absence of repeated knots or control points. At a knot, $C_{i,p}$, is $p-m$ times continuously differentiable, where $m$ is the multiplicity of the knot (here, multiplicity is the number of times that the knot appears in the knot vector), decreasing also the global continuity of the approximation.

2. If the function to be approximated is monotone the approximation with B-splines will be monotone as wll (variation diminishing). Moreover, it satisfies

$$\Big| \sum_{i=1}^{\mathrm{n_p}+1} C_{i,p}(\lambda) P_i \Big| \leq \max_i |P_i|$$

3. Affine transformations of the approximation are obtaining only by applying the transformation to the control points (affine covariance).

4. $u(\lambda_1) = P_1$ and $u(\lambda_{\mathrm{n}_k+1}) = P_{\mathrm{n}_{cp}+1}$ (end-point interpolation)

5. Between knots, the approximation is $\mathcal{C}^\infty$, whereas at knots, continuity decreases upto $\mathcal{C}^{p-m}$, where $m$ is the multiplicity of the knots.

These properties motivate the use of B-splines for shock-capturing problems with DG methods.

## C.3 B-splines for solving shock-capturing problems

In Chapter 3 a shock-capturing method based on the introduction of artificial viscosity is presented. Despite the method gives excellent results, it is well-known that high-order methods are non monotone. Therefore, small oscillations due to the Gibbs effect inside one element could still arise when discontinuities or high-gradients are simulated.

The motivation for using B-splines as a tool for shock-capturing problems relies in their variation diminishing property. The goal here is to check if the use of B-splines in conjunction with artificial diffusion method provides accurate solutions free of spurious oscillations, also ensuring monotone solutions. This work is motivated by the investigations by Hughes et al. (2005), that propose the use of B-splines in combination with the SUPG method for solving convection-diffusion problems. Further steps are here taken, in the sense that the use of B-splines is applied to purely convection

problems and non-linear ones, which involve more involved features, as discontinuities and shocks.

### C.3.1 The variation-diminishing property of the knot insertion

The insertion of knots for a B-spline approximation is a tool to increase the number of degrees of freedom of an approximation without changing the polynomial degree of the basis function.

Given a knot vector $\Lambda = \{\lambda_1, \ldots, \lambda_{n_{k+1}}\}$ the insertion of the knot $\hat{\lambda} \in [\lambda_k, \lambda_{k+1}]$ does not modify the approximation. Moreover the base of B-splines corresponding to the knot vector $\hat{\Lambda} = \{\lambda_1, \ldots, \hat{\lambda}, \ldots, \lambda_{n_{k+1}}\}$ can be easily obtained from the previous without computing again the full set of basis functions (see Piegl et al. (1995) for the details). This property also gives computational advantage to the knot insertion and knot removal processes.

**Remark C.1.** *The insertion of knots can be compared with the h-refinement of a mesh in finite elements when the inserted knot has multiplicity p.*

The knot insertion procedure also preserves the variation diminishing property of B-splines. That is: if $u(\lambda) = \sum_{i=1}^{n_{cp}+1} C_{i,p}(\lambda) P_i$ and $u(\lambda) = \sum_{i=1}^{n_{cp}+2} C_{i,p}(\lambda) \hat{P}_i$ are the respective approximations obtained with the knot vectors $\Lambda$ and $\hat{\Lambda}$, then

$$S[\hat{\mathbf{P}}] \leq S[\mathbf{P}] \tag{C.2}$$

. where the function $S[\mathbf{v}]$ is defined as the number of sign changes in the sequence defined by the vector $\mathbf{v}$. $\hat{\mathbf{P}}$ and $\mathbf{P}$ are the vectors corresponding to the control points of each approximation. This property can be seen as a powerful tool to obtain high accurate approximations in the areas where the solution is not well-resolved, as it is shown next.

### C.3.2 First assessments of approximation with B-splines

To get an intuitive idea of the behavior of B-splines in functions containing discontinuities of high-gradients, a first preliminary test consists on approximating step functions or functions containing high-gradients using a B-spline basis. For this purpose consider the hyperbolic tangent function, $f(x) = \tanh(10(2x-1))$ for $x \in [0,1]$. This function contains a high-gradient located at $x = 0.5$, which facilitates the current study, since the location of the shock is known *a priori*. Figure C.1 showsvthe approximation using a B-spline basis of fifth order with the Lagrange basis, using least-square approach. Gibbs oscillations, typical of high-order methods arise in the approximation. The solution computed with Lagrange basis gives identical results.

The sequence of next figures shows the same approximation but inserting two interior knots at $x = 0.4$ and $x = 0.6$, enclosing the gradient. A consecutive increasing of the multiplicity of the interior knots is considered, from multiplicity equal to 1 to multiplicity equal to 3. Since the increasing in the multiplicity produces also an increasing of the degrees of freedom, to make a fair comparison, the degree of the lagrange basis functions is increased such that the number of dof is equal for both approximations. For instance, a fifth order B-spline basis function with two interior knots of multiplicity equal to one, is compared with a seventh order Lagrange basis function. Note that, even having the same number of degrees of freedom, the increase in of multiplicity in the insertion of knots prevails the approximation of showing spurious Gibbs type oscillations.

### C.3.3 The subcell detection procedure in the knot insertion process

From the computational point of view, increasing the number of degrees of freedom may also lead to an increase of the computational cost of the process, also making the method more involved. However, a better resolution of the solution is only needed in some specific regions, where shock and strong gradients are present. The flexibility of the DG method to compute the solution element-by-element is crucial, since it

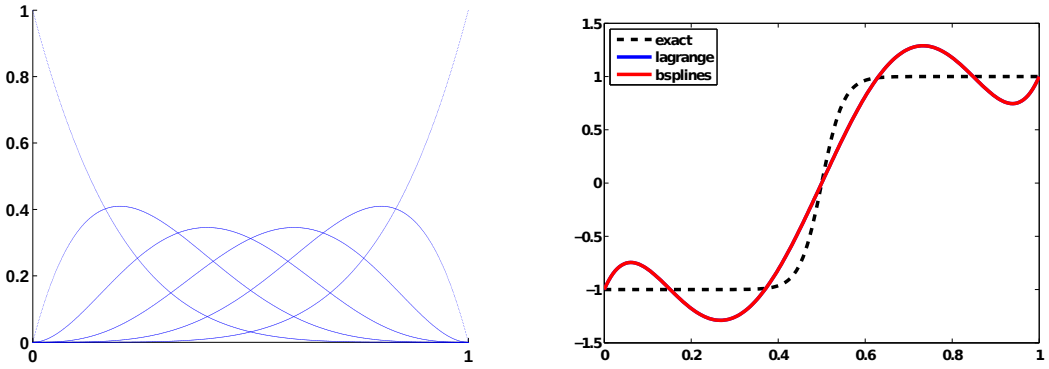


Figure C.1: Fifth order B-spline approximation with knot insertion: B-spline basis of fifth order (left) and least square approximations with B-splines of the hyperbolic tangent (right).

allows the use of different basis functions within each element. As a consequence, the accurate detection of the location of the shock plays an important role in this procedure.

For this purpose he subsensor strategy described in Section 3.1.3 is used. The subsensor is able to locate the shock with, at least, $h/p$ accuracy within the element. In the worst of cases the accuracy equals the accuracy of the default elementwise sensor (see Section 3.1.2 or Persson and Peraire (2006)) that is, it detects the shock in the whole element of size $h$.

The strategy here proposed consists on the insertion of knots only in the region detected by the subsensor and only at the instants of the simulation in which the element is marked by the sensor to contain the shock. Thus, the process of inserting and removing knots a dynamic procedure. The local insertion of knots will not significantly influence the total cost of the procedure while, in principle, it is expected to provide a better resolution of the shock.

### C.3.4 Proposed methodology

Then proposed strategy is briefly described as follows:

- The initial approximation is computed with a $p$-th degree B-spline basis func-

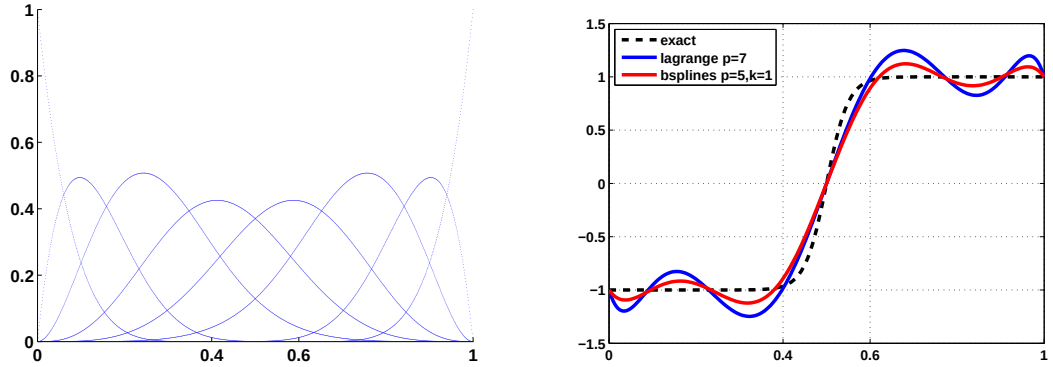


(a) multiplicity equal to 1

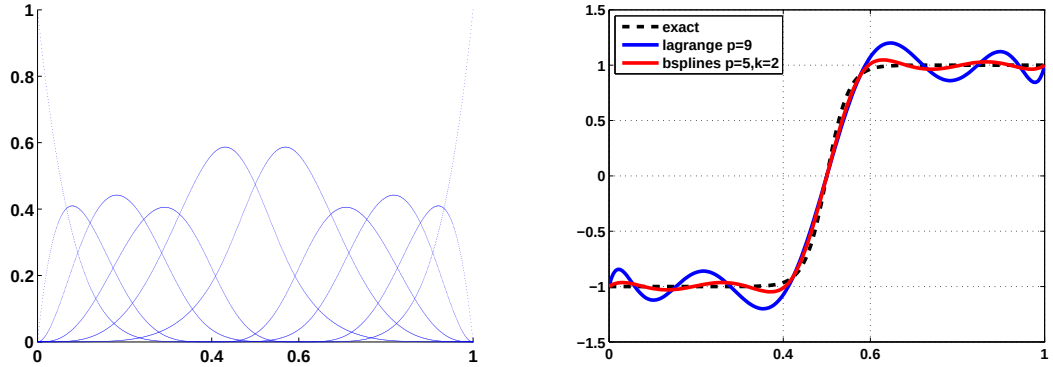


(b) multiplicity equal to 2

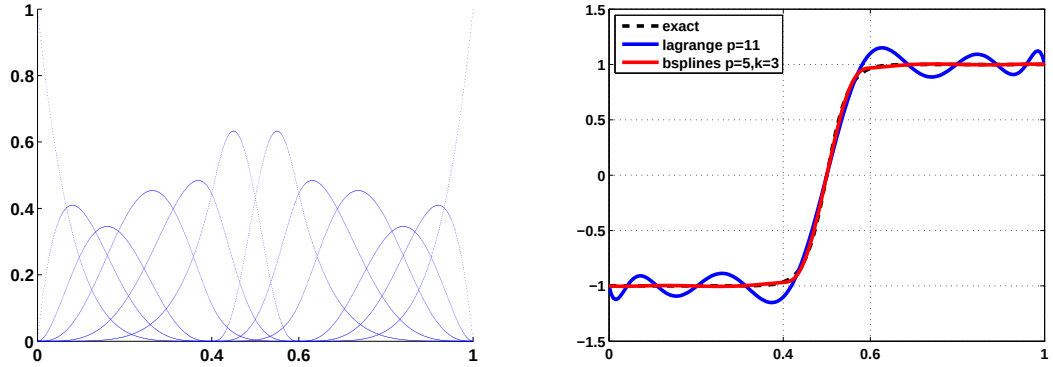


(c) multiplicity equal to 3

Figure C.2: Fifth order B-spline approximation with knot insertion of different multiplicity: B-spline basis (left) and comparison with a Lagrange basis functions for the same number of dof (right).

tions and $p+1$ degrees of freedom. This corresponds to select the following knot vector $\Lambda = \{\underbrace{0\ldots0}_{p+1}\underbrace{1\ldots1}_{p+1}\}$.

- Apply the artificial diffusion scheme proposed in Chapter3.
- Activate the subsensor algorithm in those elements detected by the shock-sensor.
- Insert two knots, one at each extreme of the detected subregion of the element.

Notice also that this procedure is dynamic in the sense that knots are inserted and removed depending on the subsensor detection. As a consequence the number of degrees of freedom may vary for every element and every time step. However, the degree of the approximation is kept constant along all the simulation.

## C.4 Examples

The application of the proposed methodology is illustrated using two numerical examples: a long-time advection of sharp profiles and the inviscid Burgers' equation. The obtained solutions with B-splines are also compared with the approximation using standard Lagrange basis functions and constant number of degrees of freedom.

### C.4.1 Linear advection. Transport of a combination of Gaussians and pulses.

The first example is the linear transport of a combination of Gaussians and pulses, standard in long-time simulations, Krivodonova (2007). For the setup of this problem see Section 3.3.1.

A mesh of 100 elements and degree of interpolation $p = 3$ (400 number of degrees of freedom) has been used. At each time step the sub-cell detection is used and two extra knots are inserted in the detected region. Figures C.3 show the comparison using B-splines and the knot insertion approach and standard artificial diffusion method with

Lagrange basis and constant number of dof. A detail of the square pulse is also shown. Overshoots near discontinuities in the pulse are observed for the artificial diffusion method. Recall that, with the artificial diffusion method, "low" order approximations may suffer from some oscillations. In contrast, the approximation with B-splines removes the overshoots in the corners of the square pulse, but it also provides a smeared profile of the solution, not only around the high-gradients of the pulse, but also reducing the height of the gaussians. However, as expected by theoretical results, the approximation with B-splines look monotone.

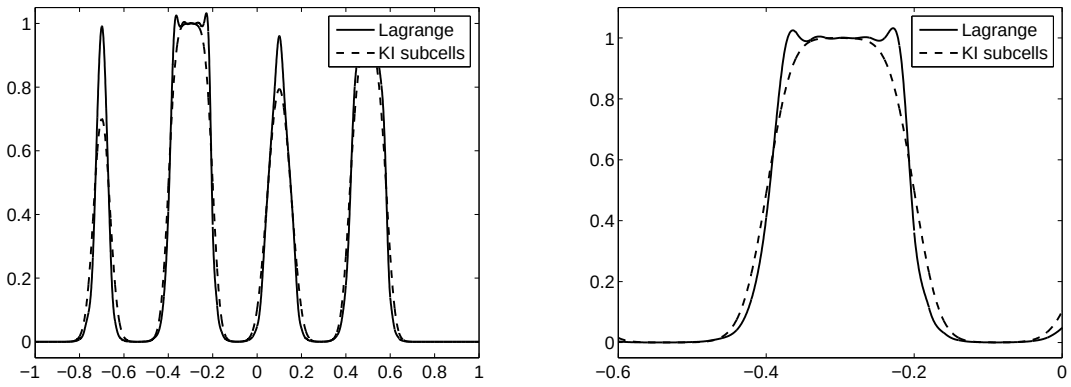


Figure C.3: Combination of Gaussians and pulses: approximations with $p = 3$ and 100 elements.

As the natural tendency of DG methods is the use of high-order elements, a mesh of 40 elements and degree of approximation $p = 6$ is now considered. Results for both methods are shown in Figure C.4. Now the situation is different: the solution with B-splines shows a more diffusive character, specially highlighted at the peaks of the cones and contours of the gradients. A detail look to the square pulse reveals that the solution with Lagrange basis functions provides a sharper profile, free of oscillations. Thus, for long-time simulations and high-order approximations B-splines don't seem to provide a major improvement.

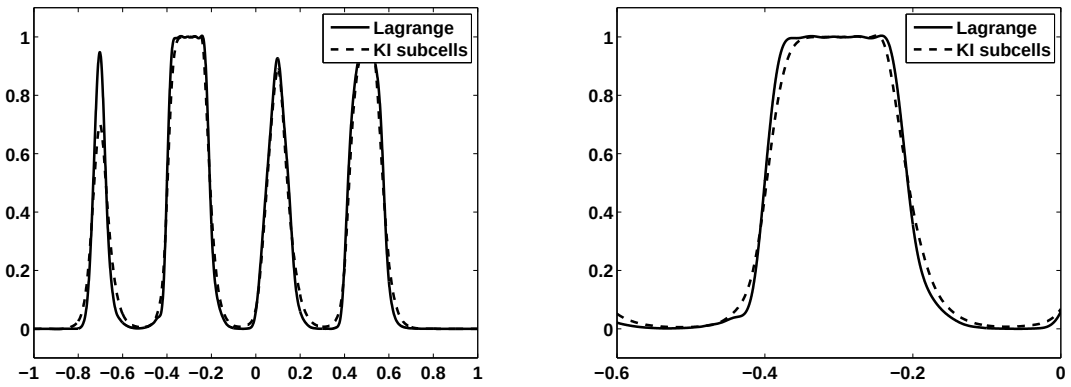


Figure C.4: Combination of Gaussians and pulses: approximations with $p = 6$ and 40 elements.

### C.4.2 Burgers equation

The second example is the classical inviscid Burgers' equation with smooth initial condition, introduced in Section 2.3.1. The problem is solved using a mesh of 10 elements and interpolation degree $p = 3$. Solutions are displayed at time $t = 0.50$, when the shock is fully formed.

Figure C.5 depicts the solutions computed with the knot insertion and Bsplines and the solution computed with standard Lagrange basis functions, both with artificial diffusion. Right figure depicts the control points for the B-spline approximation and the region detected by the sub-sensor, which is filled in grey. Recall that the process is dynamic, in the sense that knots are inserted and removed from one step to another. Hence, the number of control points is not constant. Computational elements are also represented with dashed lines. Both approximations are almost undistinguishable, capturing the shock without spurious oscillations. The solution with B-splines seems to be monotone, but right Figure reveals that this is no longer the case. Control points, marked with black dots, demonstrate that the sign condition (C.3.1) is not verified along the shock. Thus, since both approximations are almost equal and any of them guarantee monotonicity of the solution, first conclusion is that computations with B-splines do not seem to provide benefices in front of classical Lagrange polynomials. Moreover, they have an extra computational overhead because of the procedure of

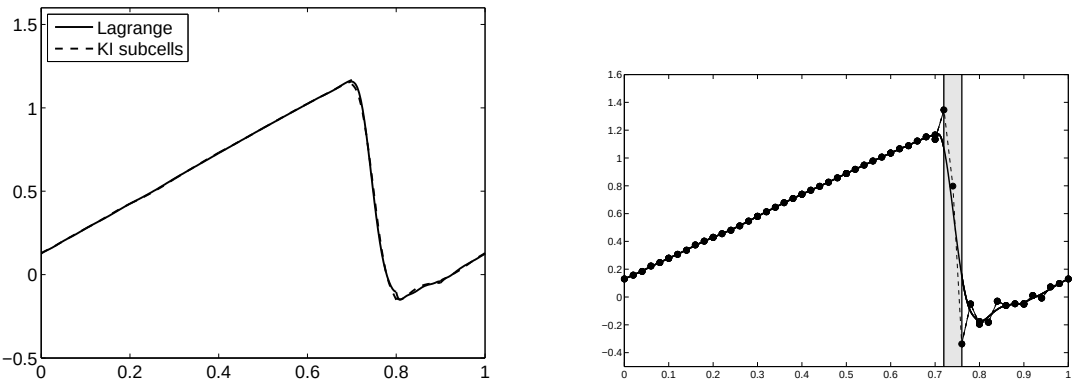


Figure C.5: Burgers' equation: third order approximations with 10 elements (left) and control points (right).

inserting and removing knots.

## C.5 Conclusions

The use of B-splines for shock-capturing problems does not seem to provide significant improvements. On one hand, the use of B-splines does not hinder the necessity of stabilization techniques, that is, B-splines by themselves are not a robust tool for capturing discontinuities, and they have to be combined with some other potential shock-capturing technique. On the other hand, numerical tests prove that, although possessing the variation diminishing property, the solutions might not be monotone anymore, since monotonicity is only kept with respect to control points, and only if the initial data is also monotone. Therefore, the variation diminishing property of B-splines is not exploited.

As the natural tendency of DG is the use of high-order elements, and for this cases the solution with B-pslines does not provide a significant improvement, it is conclude that, despite the use of B-splines is a powerful tool to be exploited, for the case of shock-capturing problems it does not provide a major advantage.

# Appendix D

# A physical application to convection-diffusion-reaction equations: dimensionless analysis of HSDM and application to simulations of Breakthrough curves of GFH

Homogeneous Surface Diffusion Model (HSDM) is widely used for adsorption modeling of aqueous dissolutions. This appendix is devoted to the dimensionless analysis of HSDM and the characterization of the model behavior. The artificial diffusion DG method presented in Chapter 3 is proposed as a numerical technique for dealing with the different flow regimes of the solution.

## D.1 Introduction

Homogeneus Surface Diffusion Model is a dual resistance model which includes influence on adsorption of film mass transfer (of the adsorbate diluted in intersticial fluid into the adsorbent particles) and of intraparticle diffusion (of the solid phase adsorbate inside the adsorbent particles), see the schematic Figure D.1. Weber and Smith (1986, 1987), Crittenden et al. (1987) and Brusseau and Gillham (1989), among

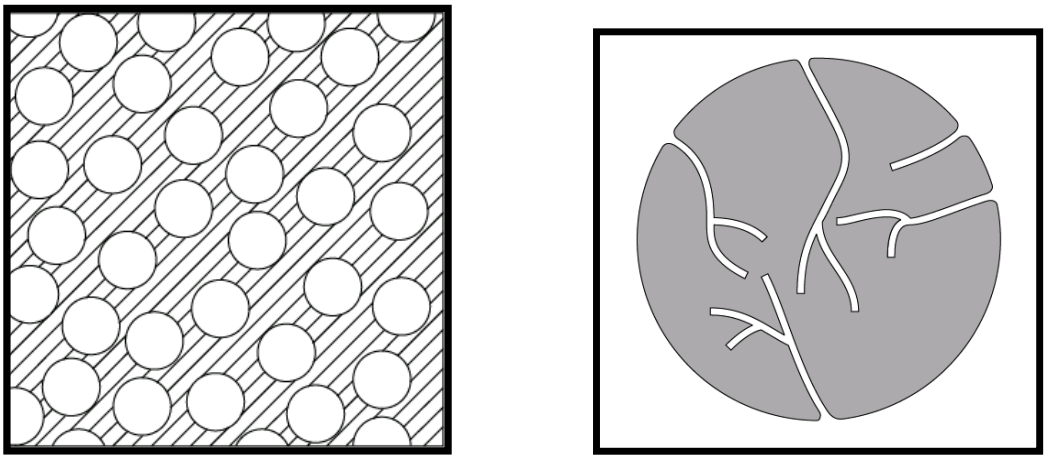

Figure D.1: Interparticle porosity (left) and intraparticle porosity (right).

others, present a general description of HSDM and different practical applications, especially related with wastewater treatment.

HSDM behavior has been characterized in terms of the Biot number, $B_i$, by several authors, see for instance Lee et al. (1983), Hand et al. (1983, 1984) or Traegner and Suidan (1989b). The Biot number is the ratio between the film mass transfer rate and the intraparticle surface diffusion and it is usually used to characterize model behavior. Three regions with different relative importance of both processes have been reported. When $B_i \ll 1$, film mass transfer dominates, while for $B_i \gg 10^2$ surface diffusion does. In between, both have significant influence on the results. These limits can be found referenced in several works dealing with homogeneous problems, see Hand et al. (1983) and Traegner and Suidan (1989a,b), referenced subsequently by Roy et al. (1993), Flora et al. (1998), Baup et al. (2000), Chang et al. (2004) and Badruzzaman et al. (2004). More recently, Sonetaka et al. (2009b,a) propose similar limits to characterize generic adsorbents using shallow bed reactors. HSDM is also widely used in heterogeneous problems, see Oimstead and Weber (1990),Smith (1996) and Rahman et al. (2003). However, in these problems characterization of HSDM with the Biot number is less frequent. One example are plug-flow tests, see for instance Lee et al. (1983), Hand et al. (1984), Brattebo and Odegaard (1986), Sperlich et al. (2005, 2008) and Genz et al. (2008).

Although HSDM has been widely used, model behavior has not been completely characterized yet. Relationships between the limit behaviors of the model and the values of key dimensionless numbers need further analysis. When designing fixed-bed adsorbers, model selection based only on Biot number is not enough. The need of complementing $B_i$ limits has been explicitly highlighted by Sperlich et al. (2008), when simulating breakthrough curves, BTC (the concentration outlet of a plug-flow fix-bed test), with Granular Ferric Hydroxide (GFH). The Stanton number, $S_t$, which is the ratio between film mass transfer rate and flow velocity, has been proposed to complement $B_i$ for characterization of HSDM results, also by Sperlich et al. (2008).

Here, a dimensionless analysis of HSDM has confirmed that both $B_i$ and $S_t$ have influence in BTC, as indicated by Sperlich et al. (2008). Additional interesting results have been found: BTC depend on $S_t$ for small values of $B_i$, but on $E_d = S_t/B_i$ ($E_d$ is the surface diffusivity modulus) for large values of $B_i$. In both cases, i.e. for small or large values of $B_i$, BTC are independent of $B_i$ values; BTC depend only on $S_t$ or $E_d$, respectively. In between, both $B_i$ and $S_t$ (or $E_d$) have influence on BTC.

These results have been obtained with a new and efficient HSDM solver: the intraparticle diffusion equation is reduced to a system of two ordinary differential equations (ODE) using a Galerkin approximation with two polynomials as base functions. This system of ODE is coupled with the partial differential equation representing transport–reaction. This coupling may give rise to a nonlinear convection-diffusion-reaction PDE, which is discretized spatially with the artificial diffusion Discontinuous Galerkin scheme described in Chapter 3 (see also Casoni et al. (2009)). As discussed in Chapter 3 formation of shocks may come from different ways. For instance, non-linear adsorption isotherms develop shocks. Also, purely convective problems are characterized by the transport of a sharp front. It is well-known that standard numerical methods are not sufficient by themselves for simulating these kind of problems, unless specific numerical techniques are used. On one hand, standard high-order methods do not preclude spurious oscillations and, on the other hand, low-order ($p = 0$) methods are overdiffusive (unless very small meshes are used) and, consequently, tend to flatten the solution excessively, losing also its physical meaning.

The approach has been applied to simulation of breakthrough curves of GFH, with real physical cases of different adsorbers. Published experimental data by Sperlich et al. (2008) has been adequately simulated.

## D.2 Mathematical model

HSDM involves two partial differential equations, representing physical processes at two different scales: The macroscale, which is a porous media with a fluid in movement throughout a matrix of adsorbent particles, and the microscale, which represents the adsorbent particles, assumed spherical and also a porous media themselves. The velocity field of the macroscale flow is considered given. Flow and adsorption/desorption are considered uncoupled, hypothesis equivalent to consider the fluid density constant.

The first partial differential equation is an unsteady transport–reaction one. It is written on the macroscale coordinates. It takes into account convection, diffusion and adsorption/desorption of components diluted in the interparticle fluid into the adsorbent particles. The second partial differential equation is an unsteady diffusion equation expressed in terms of the radius of a spherical microscale particle. The intraparticle diffusion equation takes into account the phase change, fluid–solid, and the solid diffusion of adsorbed mass inside the particles. Isothermal equilibrium between solid and fluid phases is considered, with a functional relationship between diluted and adsorbed mass. Both partial differential equations are coupled through the adsorption/desorption term of transport–reaction equation and the external boundary condition of intraparticle diffusion equation.

For the sake of simplicity on the analysis, the dimensionless form of the macroscale equation is considered.

The problem can be expressed in a dimensionless form, by introducing the following dimensionless variables $\boldsymbol{x} = \boldsymbol{x}'/L$ and $\mathrm{t} = V\mathrm{t}'/L$, and the field $\boldsymbol{v} = \boldsymbol{v}'/V$, with $L$ and $V$ reference values of length and velocity, and $\boldsymbol{x}'$, $\mathrm{t}'$ and $\boldsymbol{v}'$ equal to, respectively, time, standard spatial coordinates and flow velocity in the macroscale porous media. Unknowns are $\mathrm{c}(\boldsymbol{x},\mathrm{t}) = \mathrm{c}'(\boldsymbol{x}',\mathrm{t}')/c_{\mathrm{ref}}$ and $\bar{\mathrm{q}}(\boldsymbol{x},\mathrm{t}) = \bar{\mathrm{q}}'(\boldsymbol{x}',\mathrm{t}')/q_{\mathrm{ref}}$, with $\mathrm{c}'$ and

$\bar{\mathrm{q}}'$ equal to, respectively, concentration of adsorbate in porous media fluid and the mean value of adsorbed mass in the adsorbent particles. Parameters $c_{\mathrm{ref}}$ and $q_{\mathrm{ref}}$ are the corresponding reference values of both unknowns.

Dimensionless numbers of the model are the following:

$$\begin{gathered}\mathrm{P_e} = \frac{VL}{D}\,,\ \mathrm{r}_{\varepsilon_\mathrm{p}} = \frac{1-\varepsilon_\mathrm{f}}{\varepsilon_\mathrm{f}}\varepsilon_\mathrm{p}\,,\ \mathrm{D_g} = \frac{q_{\mathrm{ref}}\rho_\mathrm{p}(1-\varepsilon_\mathrm{f})}{c_{\mathrm{ref}}\varepsilon_\mathrm{f}}\,,\ \mathrm{B_i} = \frac{\mathrm{k_f}Rc_{\mathrm{ref}}}{\mathrm{D_s}q_{\mathrm{ref}}\rho_\mathrm{p}}\,,\\ \mathrm{S_t} = \frac{\mathrm{k_f}L(1-\varepsilon_\mathrm{f})}{VR\varepsilon_\mathrm{f}}\,,\ \mathrm{E_d} = \frac{\mathrm{D_g}\mathrm{D_s}L}{VR^2} = \frac{\mathrm{S_t}}{\mathrm{B_i}}\,,\ \mathrm{L}(\bar{\mathrm{q}}) = \frac{\bar{\mathrm{q}}'^{1/n}}{A^{1/n}}\,,\ A = A'\frac{c_{\mathrm{ref}}^n}{q_{\mathrm{ref}}}\,,\end{gathered} \tag{D.1}$$

with $\mathrm{P_e}$ the Peclet number, $D$ the interparticle diffusion, $\mathrm{r}_{\varepsilon_\mathrm{p}}$ the porosity ratio, $\varepsilon_\mathrm{f}$ and $\varepsilon_\mathrm{p}$ the inter e intraparticle porosities, $\mathrm{D_g}$ solute distribution parameter (defined as the ratio of the adsorbed mass and the interparticular diluted mass, in steady state conditions and equilibrium), $\rho_\mathrm{p}$ the density of clean particles, $\mathrm{k_f}$ the film mass transfer coefficient, $R$ the particle radius, $\mathrm{D_s}$ the intraparticle superficial diffusion, and $\mathrm{L}(\bar{\mathrm{q}})$ the Freundlich isotherm function, which depends on parametres $A'$ and $n$.

With this notation in mind, the dimensionless macroscale equation can be written as

$$\frac{\partial \mathrm{c}}{\partial \mathrm{t}} \;=\; \boldsymbol{\nabla}\cdot\left(\frac{\boldsymbol{\nabla}\mathrm{c}}{\mathrm{P_e}}\right) \;-\; \boldsymbol{v}\cdot\boldsymbol{\nabla}\mathrm{c} \;-\; \left(\mathrm{D_g} \;+\; \mathrm{r}_{\varepsilon_\mathrm{p}}\frac{\partial \mathrm{L}(\bar{\mathrm{q}})}{\partial \bar{\mathrm{q}}}\right)\frac{\partial \bar{\mathrm{q}}}{\partial \mathrm{t}} \tag{D.2}$$

where $\boldsymbol{\nabla}$ is the Gradient with respect to $\boldsymbol{x}$. Highly adsorbent media are characterized by large values of $\mathrm{D_g}$. In these cases, second part of reaction term can be neglected (that proportional to $\mathrm{r}_{\varepsilon_\mathrm{p}}$, which represents mass diluted in intraparticle porosity), hence simplifying equation (D.2).

The dimensionless intraparticle diffusion equation is given in radial coordinates and it can be expressed as

$$\mathrm{D_g}\frac{\partial \mathrm{q}}{\partial \mathrm{t}} \;=\; \mathrm{E_d}\,\frac{1}{\mathrm{r}^2}\,\frac{\partial}{\partial \mathrm{r}}\left(\mathrm{r}^2\frac{\partial \mathrm{q}}{\partial \mathrm{r}}\right) \tag{D.3}$$

with $\mathrm{q}(\mathrm{r},\mathrm{t};\boldsymbol{x})$ the dimensionless adsorbed mass profile inside the particle, which depends on r and t, but also on $\boldsymbol{x}$.

Equation (D.3) is complemented with symmetry and Robin–type boundary con-

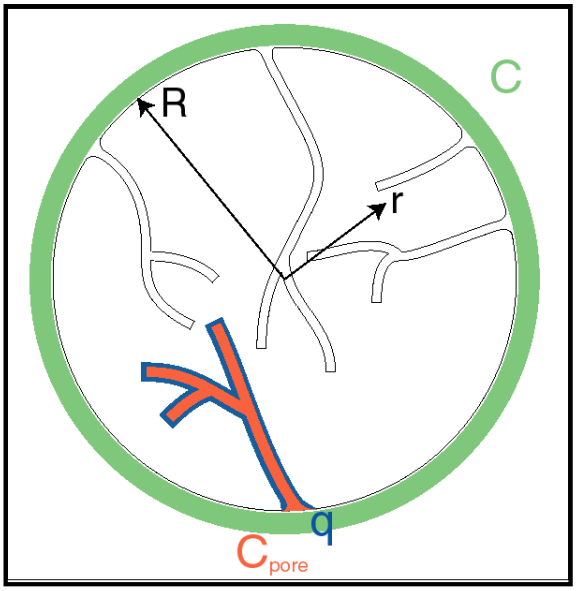


Figure D.2: Radial surface diffusion.

ditions for the center of the particle and for the particle surface, respectively

$$\left.\frac{\partial \mathrm{q}}{\partial \mathrm{r}}\right|_{\mathrm{r}=0} = 0 \quad \text{and} \quad \left.\frac{\partial \mathrm{q}}{\partial \mathrm{r}}\right|_{\mathrm{r}=1} = \mathrm{B_i}\ (\,\mathrm{c}(\boldsymbol{x},\mathrm{t}) - \mathrm{L}(\mathrm{q_R})\,)\ . \tag{D.4}$$

with $\mathrm{q_R}(\boldsymbol{x},\mathrm{t}) = \mathrm{q}(1,\mathrm{t};\boldsymbol{x}) = \mathrm{q}'_{\mathrm{R}}(\boldsymbol{x}',\mathrm{t}')/q_{\mathrm{ref}}$ and $\mathrm{q}'_{\mathrm{R}}$ the value of adsorbed mass in particle external surfaces, see Figure D.2

Ideally, equations (D.3–D.4) are a boundary value problem in r which has to be solved for each $\boldsymbol{x}$. Homogeneous tests, as the uniform batch test, can be simulated by imposing $\mathrm{c}(\boldsymbol{x},\mathrm{t}) = 1$ in equation (D.4) and discarding the transport–reaction equation (D.2).

## D.3 Numerical approach

The system of partial differential equations (D.2) and (D.3–D.4) defines the HSDM model. Several approaches have been proposed to solve numerically the model, mainly finite differences schemes for both equations (Weber and Crittenden (1975); Oimstead

and Weber (1990); Smith (1991); Sun et al. (1996); Başağaoğlu et al. (2000); Sperlich et al. (2008); Sonetaka et al. (2009b,a)), or mixed methods: finite differences schemes for the transport–reaction equation and orthogonal collocation schemes for the intraparticle difussion equation (Baup et al. (2000)), or Laplace transformation and orthogonal collocation schemes (Roy et al. (1993)). A novel approach is proposed in this work. Intraparticle diffusion equation is reduced to a system of two Ordinary Differential Equations (ODE), transport–reaction equation is discretized with a Discontinuous Galerkin method, and the overall system evolution is integrated with a time-marching scheme.

In order to simplify equations (D.3–D.4) into an ODE system, a Galerkin spatial discretization is applied. Intraparticle diffusion $\mathrm{q}(\mathrm{r},\mathrm{t};\boldsymbol{x})$ is approximated by a polynomial of degree $m \geq 2$ in r:

$$\mathrm{q}(\mathrm{r},\mathrm{t};\boldsymbol{x}) \;=\; \bar{\mathrm{q}}(\boldsymbol{x},\mathrm{t})\,\frac{3+m}{m}\,(1-\mathrm{r}^m) \;+\; \mathrm{q}_{\mathrm{R}}(\boldsymbol{x},\mathrm{t})\,\frac{1}{m}\,((3+m)\mathrm{r}^m-3)\;. \tag{D.5}$$

Unknown of equations (D.3–D.4) changes from $\mathrm{q}(\mathrm{r},\mathrm{t};\boldsymbol{x})$ to the couple of variables $\bar{\mathrm{q}}(\boldsymbol{x},\mathrm{t})$ and $\mathrm{q}_{\mathrm{R}}(\boldsymbol{x},\mathrm{t})$.

After some arithmetical operations, the following system of two coupled ODE is found:

$$\begin{aligned}
\mathrm{D_g}\frac{\partial\bar{\mathrm{q}}}{\partial\mathrm{t}} &= 3\mathrm{S_t}(\mathrm{c}-\mathrm{L}(\mathrm{q_R}))\\
\mathrm{D_g}\frac{\partial\mathrm{q_R}}{\partial\mathrm{t}} &= (2m+6)\mathrm{S_t}(\mathrm{c}-\mathrm{L}(\mathrm{q_R}))+\frac{3m^3+15m^2+36m+27}{2m+1}\mathrm{E_d}(\bar{\mathrm{q}}-\mathrm{q_R})\,.
\end{aligned} \tag{D.6}$$

Equations (D.6) are explicitly coupled with transport–reaction equation (D.2) through $\mathrm{c}(\boldsymbol{x},\mathrm{t})$, and $\bar{\mathrm{q}}(\boldsymbol{x},\mathrm{t})$. The overall system, equations (D.2) and (D.6), is linear for linear isotherms, $n = 1$.

Note that a polynomial of degree $m$ has been used to simplify intraparticle diffusion equation in reducing the microscale model by Galerkin approximation. It is well established that second order approximation, $m = 2$, works fine in many situations, but some works have analyzed different contexts and models and conclude proposing

degrees higher than two, see for instance Li and Yang (1999), Sircar and Hufton (2000), Başağaoğlu et al. (2000) or Gadre et al. (2005). In order to obtain a more accurate approximation, here, a variable value of $m$, function of $\xi = \log(\mathrm{E_d}) = \log(\mathrm{S_t}/\mathrm{B_i})$, is proposed: $m = 2$ for $\xi \geq 0$ (or equivalently $\mathrm{S_t} \geq \mathrm{B_i}$), and following expression for $\xi \leq 0$ ($\mathrm{S_t} \leq \mathrm{B_i}$):

$$m(\xi) = 0.389 \cdot \xi^4 - 0.336 \cdot \xi^3 + 1.275 \cdot \xi^2 + 2\,. \tag{D.7}$$

Following values are given by equation (D.7): $m(0) = 2$, $m(-1) = 3$, $m(-2) \approx 16$, $m(-3) \approx 54$. Expression of $m(\xi)$ has been defined imposing $\frac{\mathrm{d}m}{\mathrm{d}\xi}|_{\xi=0} = 0$, in order to present a smooth transition at $\xi = 0$.

Equation (D.7) has been adjusted comparing results of the reduced model, equations (D.6), with those of the full intraparticle model, equations (D.3–D.4). A uniform batch test (with final time equal to $\mathrm{D_g}$) is used for comparison. Both problems have been solved numerically with very high precision. The evolution of mean adsorved mass, $\bar{\mathrm{q}}$, has been used to measure goodness of the aproximation. Best $m$ values have been chosen for each set of dimensionless numbers. The proposed expresion of $m$, equation (D.7), captures main findings of the adjustment process. Proposal is independent of $\mathrm{B_i}$, thus it should be applied for all $\mathrm{B_i}$. However, it has been tested that with values of $\mathrm{B_i} \leq 10$, the problem can be adecuately simulated with $m = 2$ also with $\mathrm{S_t} \leq \mathrm{B_i}$.

The spatial discretization of transport–reaction equation is performed with the Local Discontinuous Galerkin (LDG) scheme, see Appendix B. Nevertheless, non-linear isotherms and a range of values of dimensionless numbers (for instance large values of $\mathrm{B_i}$ and small ones of $\mathrm{E_d}$) lead the approximate solution, either of the concentration $c$ and $\bar{\mathrm{q}}$, to contain sharp shock profiles. To deal with the simulation of shocks as well as the advection of sharp fronts the artificial diffusion method of Chapter 3 is used. The method can handle the shocks, solved with accuracy and also transported along the time, even for very long time simulations, at the correct speed without flattening the profile, as shown, for instance in the examples of Section 3.3.1. Dispersion an

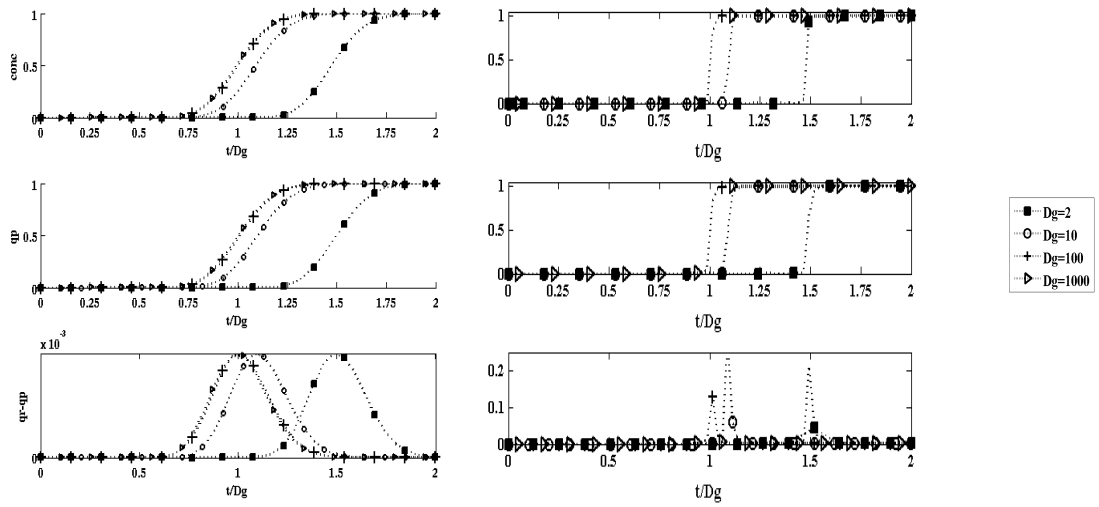


Figure D.3: Breakthrough curves, BTC, of c, $\bar{q}$ and $q_R - \bar{q}$ with $D_g$ from 2 to $10^3$, $B_i$ = 10 and $S_t = 10^2$. Results for $n = 1$, left, and $n = 0.2$, right.

dissionpative errors, typical of problems with the advection of a sharp front, are also controlled. Since the method is parameter-independent, the diffusion is computed with independence to the dimensionless parameters and also to the discretization. The sensing variable of the discontinuity sensor, see Section 2.2, is now the unknown c, i.e, the concentration of adsorbate, which is the variable transported in porous media. Note, however, that shocks may also appear in other variables, such $\bar{q}$, i.e, the concentration of the adsorbed mass in the particles.

All the simulations in this work have been performed with a mesh of one-hundred elements and degree equal to one (linear approximations). In following sections, it is shown that this is more than enough for usual applications of numerical results. However, higher degrees are also possible. Time integration of the overall system is done with the Forward Euler method. Higher order methods can also be applied.

## D.4 Results

The HSDM formulation presented in previous Sections is used here to simulate Breakthrough Curves, BTC, and to characterize limit behaviors of the model. Influence on BTC of $D_g$, $n$, $E_d$, $B_i$ and $S_t$ are assessed with detail in next subsections.

Following values define the reference problem: $L = 1$, $V = 1$, $c_{ref} = 1$, $q_{ref} = L(c_{ref})$ (therefore, $A = 1$), a constant flow velocity field $\boldsymbol{v}$=$\mathbf{1}$, and $r_{\varepsilon_p} = 0$, coherently with hypothesis of highly absorbent media, $D_g \gg 1$. A large value is imposed to $P_e$, $10^5$, that is, the viscosity effect is almost neglected.

### D.4.1 $D_g$ and $n$ influences

The influences of $D_g$ and $n$ in BTC are assessed in this subsection. Values of both parameters established here are used in following analysis.

Figure D.3 presents BTC obtained with $D_g$ from 2 to $10^3$, $n$ equal to 1 and 0.2, and fixed values $B_i = 10$ and $S_t = 10^2$. BTC of c (the standard ones, concentration outlet), but also of $\bar{q}$ (adsorbed mass at the end of the fix-bed) and the difference $q_R - \bar{q}$ (also at the end) are shown until a final time equal to $2D_g$. The difference $q_R - \bar{q}$ is a measure of uniformity distribution of adsorbed mass inside particles.

In all cases of Figure D.3, adsorption is much faster than convection. In fact, $S_t = 10^2$ indicates that film mass transfer is two orders of magnitude faster than convection, and $B_i = 10$ indicates that internal diffusion is just one order of magnitude slower than film mass transfer (and therefore, one faster than convection). Fast adsorption can be identified in Figure D.3. c and $\bar{q}$ BTC are undistinguishable. Coherently, the difference $q_R - \bar{q}$ is close to zero in all cases.

Values of $D_g$ can be very large in highly adsorbent media, up to $10^5$. Since final simulating time is proportional to $D_g$, simulation of highly adsorbent media can be expected to imply large computational time. As can be checked in Figure D.3, solution of fast adsorption processes are smooth waves traveling at constant velocity equal to $1/(1 + D_g)$, which, for large $D_g$, is approximately $D_g^{-1}$. BTC of $D_g = 100$ and 1000 in Figure D.3 are undistinguishable. In this work, except explicitly indicated, $D_g = 10^3$

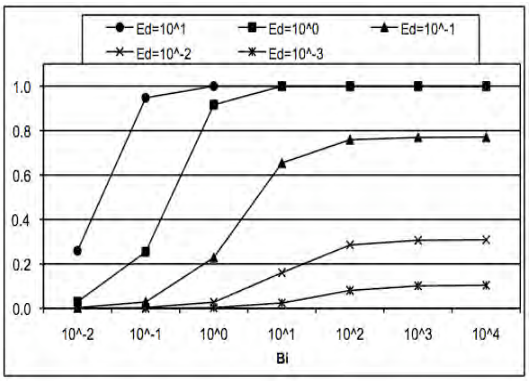


Figure D.4: Uniform batch test. Adsorbed mass inside particles at final time equal to $D_g$.

is considered. Wave front position computed with this value will present an additional delay of 0.001, as maximum, with respect results computed with higher values of $D_g$.

On the other hand, influence of $n$ is reduced to BTC shape, as Figure D.3 shows. Usually, values of $n$ range from 0.1 to 1. Although it has a relevant influence on BTC, it has not in general conclusions of this section. As $n = 1$ makes the problem linear, this value is used if not explicitely indicated. Nonlinearity do not change overall dimensionless behavior of the model, although BTC shapes are very different, specially due to the presence of shocks. However, the numerical solver here proposed it's not influenced by the value of $n$, since the artificial diffusion is automatically computed and parameter-free.

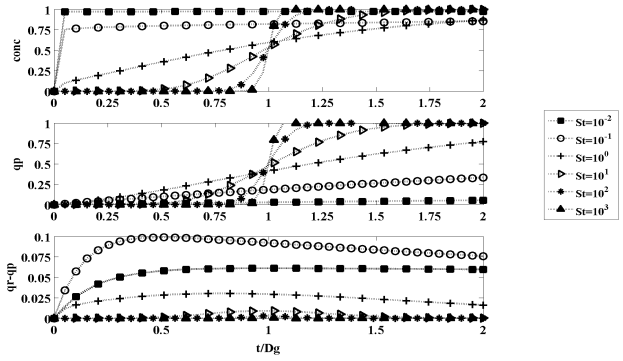


Figure D.5: Breakthrough Curves of c, $\bar{q}$ and $q_R - \bar{q}$ for $B_i = 10^0$.

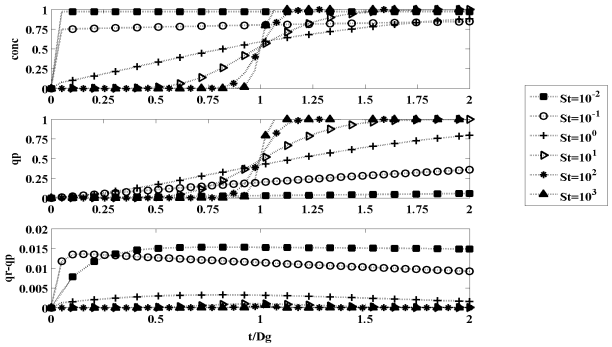


Figure D.6: Breakthrough Curves of c, $\bar{q}$ and $q_R - \bar{q}$ for $B_i = 10^{-1}$.

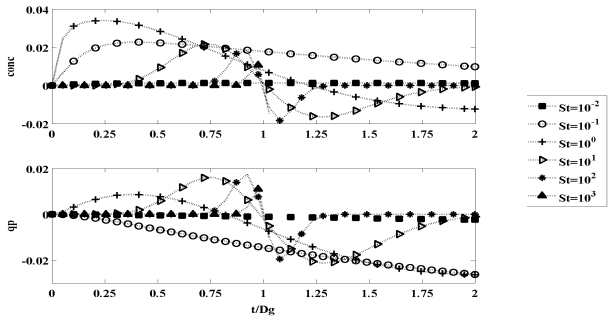


Figure D.7: Differences between Breakthrough Curves (c and $\bar{q}$) computed with $B_i = 10^0$ (Figure D.5) and $B_i = 10^{-1}$ (Figure D.6) for common values of $S_t$.

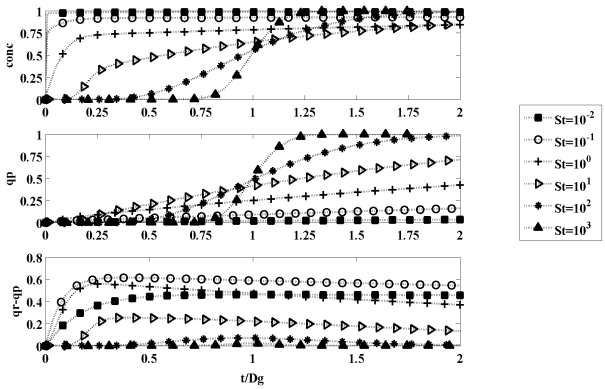


Figure D.8: Breakthrough Curves of c, $\bar{q}$ and $q_R - \bar{q}$ for $B_i = 10^2$.

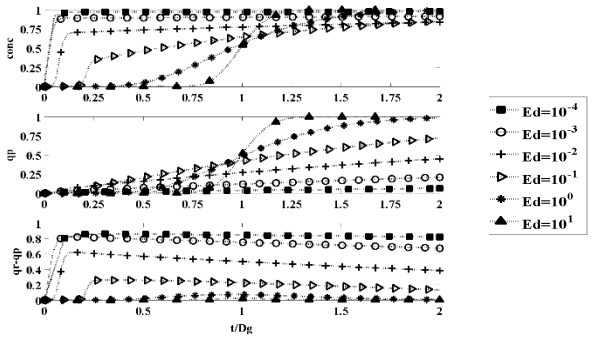


Figure D.9: Breakthrough Curves of c, $\bar{q}$ and $q_R - \bar{q}$ for $B_i = 10^3$.

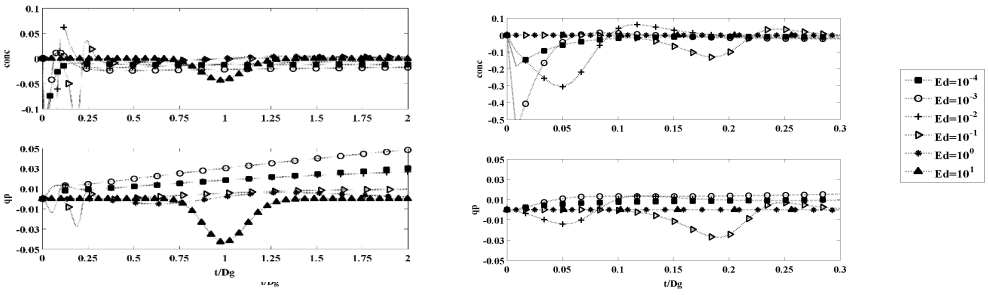


Figure D.10: Differences between Breakthrough Curves (c and $\bar{q}$) computed with $B_i = 10^3$ (Figure D.9) and $B_i = 10^2$ (Figure D.8), for same values of $E_d = S_t/B_i$.

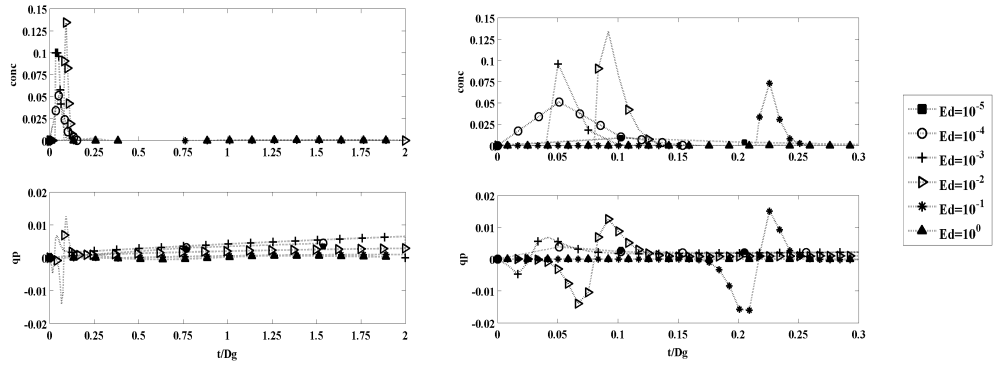


Figure D.11: Differences between Breakthrough Curves (c and $\bar{q}$) computed with $B_i = 10^4$ and $B_i = 10^3$ (Figure D.9), for same values of $E_d$.

### D.4.2 $E_d$ influence

The influence of $E_d$ in HSDM appears clearly in a standard uniform batch test. Adsorbed mass inside particles at final time equal to $D_g$ (for wide ranges of values of $E_d$ and $B_i$) are presented in Figure D.4. Final adsorbed mass is close to one in all cases with $B_i \leq 10^0$ (higher internal diffusion than film mass transfer) and $E_d B_i = S_t \geq 10^0$ (higher film mass transfer than intraparticle velocity), as well as, $B_i \geq 10^0$ and $E_d \geq 10^0$ (higher film mass transfer than internal diffusion and internal diffusion than intraparticle velocity). Keeping the $B_i$ value fixed, larger is the value of $E_d$ and faster is adsorption, and, therefore, more part of adsorption capacity is used during the time scale given by $D_g$. In the oppossite direction, lower is the value of $E_d$ and less relevant is adsorption at $D_g$ time scale. Just part of the adsorption capacity is used in these cases (check $E_d \leq 10^{-2}$ in Figure D.4).

### D.4.3 $B_i$ and $S_t$ influences

In this subsection, solutions for a wide range of $B_i$ and $S_t$ are presented and analyzed. All cases are computed with $D_g = 10^3$, $n = 1$, and until a final time equal to $2D_g$.

Figure D.5 shows BTC of cases $B_i = 10^0$ and $S_t = 10^{-2}$ to $10^3$. Large values of $S_t$ implies fast adsorption, and both c and $\bar{q}$ BC show a front traveling at velocity $D_g^{-1}$ (as in Figure D.3). Small values of $S_t$ imply a smoothed wavefront and, also, that just part of the medium is fully functional (filled of adsorbent) at this time scale. In the limit case of no-adsorption, $S_t = 0$, a wavefront traveling at velocity one (much faster than $D_g^{-1}$)) is obtained. It corresponds to a pure convection problem. This behavior can be identified in Figure D.5, with the lowest values of $S_t$. A sharp front is found just at the beginning of the BTC, at time equals to one.

Figure D.6 shows BTC of cases $B_i = 10^{-1}$ and same $S_t$ range of Figure D.5. Same behavior as before is found with $B_i = 10^{-1}$, except for the values of $\bar{q} - q_R$, that are one order of magnitude lower than in $B_i = 10^0$ case. With $B_i = 10^{-1}$, adsorption retardation is mainly due to film mass transfer (values of $\bar{q}$ and $q_R$ are almost the same all time), intraparticle diffusion does not influence adsorption.

In order to compare both sets of results, Figure D.7 shows results obtained with $B_i = 10^0$ (Figure D.5) minus those obtained with $B_i = 10^{-1}$ (Figure D.6); with same values of $S_t$ in both cases. Errors are less than 4% in all cases and time, and less than 2% in most of them. Differences between results obtained with $B_i$ values lower than $10^{-1}$, keeping same $S_t$, are lower than those obtained between $B_i = 10^0$ and $B_i = 10^{-1}$. Therefore, a limit behaviour is found with $B_i \leq 10^0$. In this limit case, BTC depend only on $S_t$, which covers from instantaneus adsorption $S_t \geq 10^3$ to pure convection (and, therefore, no adsorption at this time scale) $S_t \leq 10^{-2}$.

On the other hand, large values of $B_i$ imply that film mass transfer is higher than internal diffusion and hence, value of surface diffusion dominates behavior of the model. Figure D.8 shows results of $B_i = 10^2$ and $S_t = 10^{-2}$ to $10^3$. Although same limit behaviors for $S_t$ values as in previous cases (Figures D.5 and D.6) are identified, intermediate values have different behavior. A smooth step is identified at an early stage of BTC of c (concentration outlet). Adsorbed mass $\bar{q}$ presents a

smoother profile, that tends to zero for small values of $S_t$, highlighting the convective character of the process for this range of values.

Figure D.9 shows results for $B_i = 10^3$ and same range of $E_d$ than in Figure D.8, from $10^{-4}$ to $10^1$. Note that the offset in values of $E_d$ with respect to $S_t$ is due to the definition $E_d = S_t/B_i$. Similar BTC are obtained for same $E_d$ but larger values of $S_t$, that is, fast adsorption process. Note that for these values, which corresponds to $E_d = 10^0$ and $E_d = 10^1$ (i.e, $S_t = 10^3$ and $10^4$, respectively) curves c and $\bar{q}$ are indistinguishable (i.e, $\bar{q} - q_R$ is almost zero, which means that intraparticle diffusion is neglected in the adsorption process).

Figure D.10 presents results obtained with $B_i = 10^3$ minus those with $B_i = 10^2$ (Figures D.8 and D.9), for same values of $E_d$. The overall difference is zero along all the process except in front position, where differences of 10% can be appreciate. This difference corresponds to the initial steep profile, which is more accentuated for $B_i = 10^3$. In order to further study the limit case $B_i = 10^3$, differences between results obtained with $B_i = 10^4$ minus those with $B_i = 10^3$ are shown in Figure D.11, also for same $E_d$. Again, differences are reduced at all time, except at an early stage of the simulations, where punctual errors up to 10% are detected, enhancing again the fact that for very large values of $B_i$, the value of $S_t$ does not longer characterize by itself the global behavior.

To sum up, it can be considered that there is a limit behaviour for $B_i \geq 10^3$, where BTC depend only on $E_d$. In this limit case, analogously to the first analysis for $B_i \leq 10^0$, $E_d$ covers from instantaneous adsorption $E_d \geq 10^1$ to pure convection (no adsorption at this time scale) $E_d \leq 10^{-4}$.

Table D.1: GFH data for HSDM simulations. From Sperlich et al. (2008), except (*), from this work.

| | $B_i$ | $S_t$ | $E_d$ | $D_g$ | n | R |
|---|---|---|---|---|---|---|
| Salicylic Acid | 16.3 | 6.9 | 0.4233 | 4 155 | 0.52 | 0.39 |
| DOC | 23.3 | 3.9 | 0.1673 | 8 140 | 0.62 | 0.39 |
| Phosphate | 102.1 | 10 | 0.0979 | 20 323 | 0.19 | 0.45 |
| Arsenate | 182.5 | 9.7 | 0.0532 | 24 617 | 0.19 | 0.45 |
| Arsenate (*) | 91.25 | 4.5 | 0.0532 | 1000 | 0.19 | 0.45 |

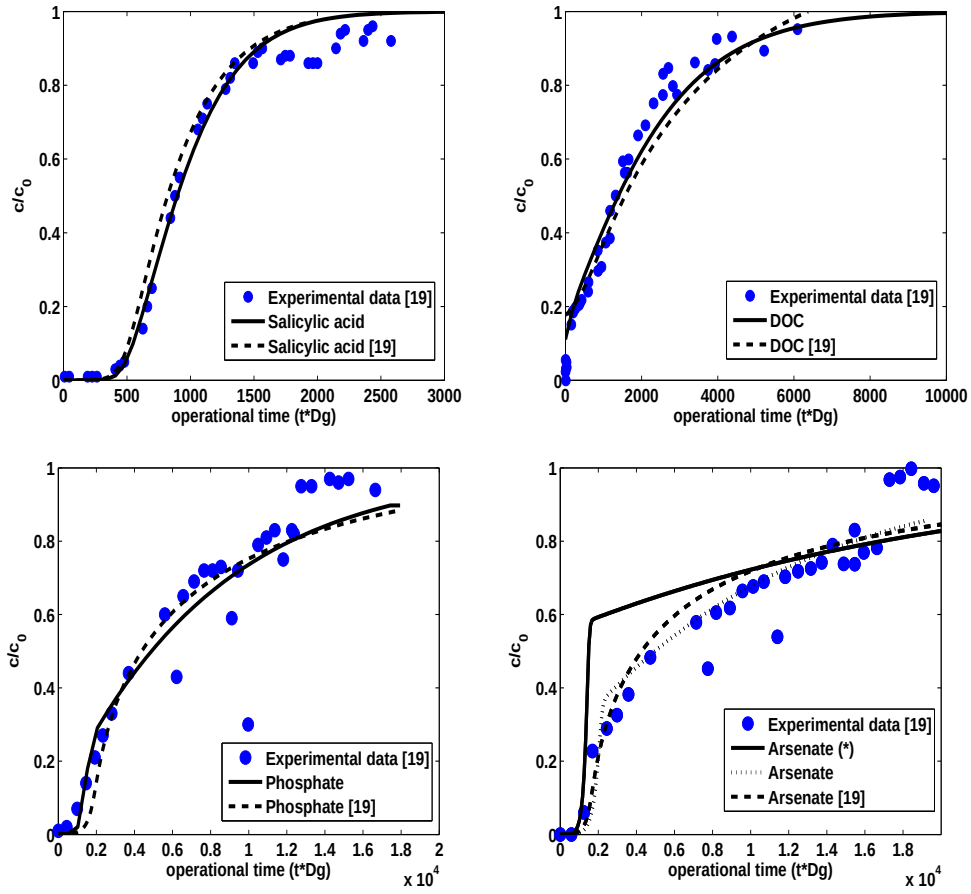


Figure D.12: Experimental data Sperlich et al. (2008) and HSDM simulations for salycilic acid, DOC, phosphate and arsenate (from left to right and up to down), using values of the Table D.1.

## D.5 GFH characterization with HSDM

Experimental adsorption results for different adsorbates in GFH have been reproduced with the HSDM in Sperlich et al. (2008). Characteristic dimensionless numbers of these cases are: Large values of $D_g$, from $10^3$ to $10^5$, non-linear isotherms, $n < 1$, values of $B_i$ from $10^1$ to $10^3$, and $E_d = S_t/B_i$ from $10^{-2}$ - $10^0$. Thus, the HSDM behavior is close to the limit detected for high $B_i$, and with intermediate values of $E_d$. BTC with similar shape to those of Figures D.8 and D.9 are expected.

Figure D.12 shows the BTC of four adsorbates (salycilic acid, DOC, phosphate

and arsenate) computed with the HSDM model presented here, together with the experimental data and the simulation results presented by Sperlich et al. (2008). Table D.1 summarizes parameters that define these examples. Computations have been done with parameters of Table D.1, except $D_g$, limited to 1000 in all cases.

In three of the four cases, as expected, similar results are obtanied with the HSDM formulation presented here and that proposed by Sperlich et al. (2008). However, in the case of arsenate, differences are very significant. This is provably due to the over-diffusive character of the numerical solver used in previous computations (finite diferences), instead of the high-order degree approximation of the interparticle diffusion equation and the DG scheme for transport applied here. Moreover, the artificial diffusion method also has been proven to be much more accurate than other stabilization techniques, avoiding an extra smearing of the solution. Hence, the peak observed in the arsenate curve is produced because of the accurate numerical technique here proposed.

An additional simulation is presented for arsenate, with $B_i$ (and $S_t$) halved with respect to values proposed by Sperlich et al. (2008). This case adjusts much better exerimental data, and therefore the results presented in Sperlich et al. (2008), than the other simulation computed here but with values proposed by Sperlich et al. (2008). In fact, halving both, $B_i$ and $S_t$ does not vary the global shape of BTC, since for large values of $B_i$ the breakthrough curve only depends on $E_d$, whose value is kept constant (recall that $E_d = S_t/B_i$). Note that this agrees with the results found in previous section (see Figures D.8 and D.9), which showed that the behavior of the limit case $B_i \geq 10^2$ only depends on $E_d$.

## D.6 Concluding remarks

Modeling and numerical conclusions are extracted for the simulation of this particular problem. Both are summarized here below.

A full characterization of HSDM model, detailing its limits behaviors, has been established in this work. Here, previous limits with $B_i$ are confirmed, but they are

also complemented with the influence of $S_t$ or $E_d$. An extensive analysis based on breakthrough experiments with linear isoterms is presented. Interesting results have been found: For low values of the Biot number, $B_i \leq 10^0$, BTC depends on $S_t$, within the range from $10^{-2}$ to $10^3$. However, for high values of Biot, $B_i \geq 10^2$, results depend on $E_d$, within the range from $10^{-4}$ to $10^3$. In both cases, immediately adsorption is found with high values of $S_t$ (correspondingly, of $E_d$) and, on the contrary, a pure convection problem (that is, no adsorption) is found with lower values of both ($S_t$ and $E_d$). A step is formed at an early stage of BTC of concentration outlet for intermediate values, $10^{-2}$ to $10^{-1}$, due to high values of film mass transfer and low values of intraparticle diffusion. With lower values of $E_d$, this step collapses with convective transport at the begining of BTC, since $S_t$ values are also low.

The proposed HSDM model shows able to characterize a wide range of adsorption processes. Prediction of BTC for several adsorbates onto GFH are shown. The simulations with HSDM reproduce the experimental data and, also agreeing with previous results published in the literature Sperlich et al. (2008). Same characteristic dimensionless numbers are used, except for high Biot numbers, where the dimensionless numbers $B_i$ and $S_t$ need to be modified in order to better adjust the data, but $E_d$ number is kept constant. As numerical results show, keeping $E_d$ constant does not vary the behavior of BTC curves, since the limit behavior found for high $B_i$ numbers does not depend on $S_t$, neither $B_i$. Hence, GFH simulations agree with the expected results, confirming the full characterization of the model here proposed.

Regarding the numerical approach, the artificial diffusion method, this example demonstrates that the artificial diffusion method is applicable not only for hyperbolic conservations laws, but also to general convection-diffusion-reaction equation. It can handle with shocks and nonlinearities of different nature, either from the convective part or from a highly nonlinear reaction term. The obtained wave travels at the correct speed without dispersion errors. It is especially highlighted that the artificial diffusion term does not depend on the form of the equation, neither the behavior of the solution, in the sense that it is parameter-free and it is automatically computed for any problem and discretizacion.

# Bibliography


Abgrall, R., S. Lantéri, and T. Sonar (1999). ENO approximations for compressible fluid dynamics. *ZAMM Z. Angew. Math. Mech. 79*(1), 3–28.

Aizinger, V., C. Dawson, B. Cockburn, and P. Castillo (2000). The local discontinuous galerkin method for contaminant transport. *Advances in Water Resources 24*(1), 73 – 87.

Anderson, J. (1984). *Modern Compressible Flow*. New York, EUA: McGraw Hill Inc.

Arias, O., O. Falcinelli, N. Fico, and S. Elaskar (2007). Finite Volume simulation of a flow over a NACA 0012 using Jamseon, MacCormack, Shu and TVD esquemes. *Mecanica Computacional XXVI*, 3097–3116.

Arnold, D. N. (1982). An interior penalty finite element method with discontinuous elements. *SIAM J. Numer. Anal. 19*(4), 742–760.

Arnold, D. N., F. Brezzi, B. Cockburn, and L. D. Marini (2001). Unified analysis of discontinuous Galerkin methods for elliptic problems. *SIAM J. Numer. Anal. 39*(5), 1749–1779.

Başağaoğlu, H., T. Ginn, J. McCoy, and M. Mariño (2000). Linear driving force approximation to a radial diffusive model. *AIChE Journal 46*(10), 2097–2105.

Badruzzaman, M., P. Westerhoff, and D. Knappe (2004). Intraparticle diffusion and adsorption of arsenate onto granular ferric hydroxide (GFH). *Water Research 38*, 4002–4012.

Barter, G. and D. Darmolfal (2007). Shock capturing with higher-order, PDE-based artificial viscosity. In *Proc. of the 18th AIAA Computational Fluid Dynamics Conference*, Miami, FL. AIAA-2007-3823.

Barter, G. E. (2008). *Shock capturing with PDE-based artificial viscosity for an adaptive, higher-order discontinuous Galerkin finite element method*. Ph. D. thesis, Massachusetts Institute of Technology, Boston, USA.

Barth, T. (1994). Aspects of unstructured grids and Finite Volume solvers for the Euler and Navier-Stokes equations.

Barth, T. J. and D. C. Jespersen (1989). The design and application of upwind schemes on unstructured meshes. In *Proc. of the 27th AIAA Aerospace Sciences Meeting*, Reno, NV. AIAA-89-0366.

Bassi, F. and S. Rebay (1997a). A high-order accurate discontinuous finite element method for the numerical solution of the compressible Navier-Stokes equations. *J. Comput. Phys. 131*(2), 267–279.

Bassi, F. and S. Rebay (1997b). High-order accurate discontinuous finite element solution of the 2D Euler equations. *J. Comput. Phys. 138*(2), 251 – 285.

Bassi, F. and S. Rebay (2001). Numerical evaluation of two discontinuous Galerkin methods for the compressible Navier-Stokes equations. *Int. J. Numer. Methods Eng. 40*(10), 197–207.

Baumann, C. E. and J. T. Oden (1999). A discontinuous *hp* finite element method for convection-diffusion problems. *Comput. Methods Appl. Mech. Engrg. 175*(3-4), 311–341.

Baup, S., C. Jaffre, D. Wolbert, and A. Laplanche (2000). Adsorption of pesticides onto granular activated carbon: Determination of surface diffusivities using simple batch experiments. *Adsorption 6*, 219–228.

Biswas, R., K. D. Devine, and J. E. Flaherty (1994). Parallel, adaptive finite element methods for conservation laws. *Appl. Numer. Math. 14*(1-3), 255–283.

Brattebo, H. and H. Odegaard (1986). Phosphorus removal by granular activated alumina. *Water Research 20*(8), 977–986.

Brezzi, F., G. Manzini, D. Marini, P. Pietra, and A. Russo (2000). Discontinuous Galerkin approximations for elliptic problems. *Numer. Methods Partial Differential Equations 16*(4), 365–378.

Brusseau, M. and P. R. R. W. Gillham (1989). Sorption nonideality during organic contaminant transport in porous media. *Critical Reviews in Environmental Science and Technology 19*(1), 33–99.

Burbeau, A., P. Sagaut, and C.-H. Bruneau (2001). A problem-independent limiter for high-order Runge-Kutta discontinuous Galerkin methods. *J. Comput. Phys. 169*(1), 111–150.

Casoni, E., J. Peraire, and A. Huerta (2009). *One-Dimensional Shock-Capturing for High-Order discontinuous Galerkin Methods*, Volume 14 of *ECCOMAS Multidisciplinary Jubilee Symposium. Computational Methods in Applied Sciences*. Springer Netherlands.

Casoni, E., J. Peraire, and A. Huerta (2011a). A simple shock-capturing technique for high-order discontinuous Galerkin methods. *to appear in International Journal of Numerical Methods in Fluids*.

Casoni, E., J. Peraire, and A. Huerta (2011b). Un método de captura de choques basado en las funciones de forma para Galerkin discontinuo en alto orden. *to appear in Revista Internacional de Métodos Numéricos en Ingeniería*.

Casper, J. and H. L. Atkins (1993). A Finite-Volume high-order ENO scheme for two-dimensional hyperbolic systems. *J. Comput. Phys. 106*(1), 62–76.

Chang, S., T. Waite, P. Ong, A. Schfer, and A. Fane (2004). Assessment of trace estrogenic contaminants removal by coagulant addition, powdered activated carbon adsorption and powdered activated carbonmicrofiltration processes. *Journal of Environmental Engineering 130*(7), 736–742.

Chavent, G. and B. Cockburn (1989). The local projection $P^0P^1$-discontinuous-Galerkin finite element method for scalar conservation laws. *RAIRO Modél. Math. Anal. Numér. 23*(4), 565–592.

Chavent, G. and G. Salzano (1982). A finite-element method for the 1-D water flooding problem with gravity. *J. Comput. Phys. 45*(3), 307–344.

Cockburn, B. (2001). Devising discontinuous Galerkin methods for non-linear hyperbolic conservation laws. *J. Comput. Appl. Math. 128*(1-2), 187 – 204.

Cockburn, B., J. Gopalakrishnan, and R. Lazarov (2009). Unified hybridization of discontinuous Galerkin, mixed, and continuous Galerkin methods for second order elliptic problems. *SIAM J. Numer. Anal. 47*(2), 1319–1365.

Cockburn, B., S. Hou, and C.-W. Shu (1990). The Runge-Kutta local projection discontinuous Galerkin finite element method for conservation laws. IV. The multidimensional case. *Math. Comp. 54*(190), 545–581.

Cockburn, B., S. Y. Lin, and C.-W. Shu (1989). TVB Runge-Kutta local projection discontinuous Galerkin finite element method for conservation laws. III. One-dimensional systems. *J. Comput. Phys. 84*(1), 90–113.

Cockburn, B. and C.-W. Shu (1989). TVB Runge-Kutta local projection discontinuous Galerkin finite element method for conservation laws. II. General framework. *Math. Comp. 52*(186), 411–435.

Cockburn, B. and C.-W. Shu (1998a). The local discontinuous Galerkin method for time-dependent convection-diffusion systems. *SIAM J. Numer. Anal. 35*(6), 2440–2463.

Cockburn, B. and C.-W. Shu (1998b). The Runge-Kutta discontinuous Galerkin method for conservation laws. V. Multidimensional systems. *J. Comput. Phys. 141*(2), 199–224.

Cockburn, B. and C.-W. Shu (2001). Runge-Kutta discontinuous Galerkin methods for convection-dominated problems. *J. Sci. Comput. 16*(3), 173–261.

Crittenden, J., J. Berrigan, D. Hand, and B. Lykins (1987). Design of rapid fixed-bed adsorption tests for nonconstant diffusivities. *Journal of Environmental Engineering 113*(2), 243–259.

Cueto-Felgueroso, L. and I. Colominas (2008). High-order Finite Volume methods and multiresolution reproducing kernels. *Arch. Comput. Methods Eng. 15*(2), 185–228.

Demirdzic, I., Z. Lilek, and M. Peric (1993). A collocated Finite Volume method for predicting flows at all speeds. *Int. J Numerical Methods in Fluids 17*, 1029–1050.

Dolejší, V. (2004). On the discontinuous Galerkin method for the numerical solution of the Navier-Stokes equations. *Internat. J. Numer. Methods Fluids 45*(10), 1083–1106.

Donea, J. and A. Huerta (2003). *Finite element methods for flow problems*. Chichester: John Wiley & Sons.

Emery, A. (1968). An evaluation of several differencing methods for inviscid fluid flow problems. *J. Comput. Phys. 2*, 306–331.

Flora, J., R. Vidic, W. Liu, and R. Thumau (1998). Modeling powdered activated carbon injection for the uptake of elemental mercury vapors. *Journal of the Air and Waste Management Association 48*, 1051–1059.

Gadre, S., A. Ebner, and J. Ritter (2005). Further validation of the quartic concentration profile approximation for describing intraparticle transport in cyclic adsorption processes. *Adsorption 11*, 295–314.

Genz, A., B. Baumgarten, M. Goernitz, and M. Jekel (2008). Nom removal by adsorption onto granular ferric hydroxide: Equilibrium, kinetics, filter and regeneration studies. *Water Research 42*, 238–248.

Godunov, Sergei, K. (1954). *Different Methods for Shock Waves.* Ph. D. thesis, Moscow State University.

Godunov, S. K. (1959). A difference method for numerical calculation of discontinuous solutions of the equations of hydrodynamics. *Mat. Sb. (N.S.) 47 (89)*, 271–306.

Goodman, J. B. and R. J. LeVeque (1985). On the accuracy of stable schemes for 2D scalar conservation laws. *Math. Comp. 45*(171), 15–21.

Gottlieb, D. and J. S. Hesthaven (2001). Spectral methods for hyperbolic problems. *J. Comput. Appl. Math. 128*(1-2), 83–131. Numerical analysis 2000, Vol. VII, Partial differential equations.

Gottlieb, S., C.-W. Shu, and E. Tadmor (2001). Strong Stability-Preserving high-order time discretization methods. *SIAM Rev. 43*(1), 89–112.

Hand, D., J. Crittenden, and W. Thacker (1983). User-oriented batch reactor solutions to the homogeneous surface diffusion model. *Journal of Environmental Engineering 109*(1), 82–101.

Hand, D., J. Crittenden, and W. Thacker (1984). Simplified models for design of fixed-bed adsorption systems. *Journal of Environmental Engineering 103*(2), 440–456.

Hansbo, A. and P. Hansbo (2004). A finite element method for the simulation of strong and weak discontinuities in solid mechanics. *Comput. Methods Appl. Mech. Engrg. 193*(33-35), 3523 – 3540.

Harten, A. (1983). High resolution schemes for hyperbolic conservation laws. *J. Comput. Phys. 49*(3), 357–393.

Harten, A., B. Engquist, S. Osher, and S. R. Chakravarthy (1987). Uniformly high-order accurate essentially nonoscillatory schemes. III. *J. Comput. Phys. 71*(2), 231–303.

Harten, A. and S. Osher (1987). Uniformly high-order accurate nonoscillatory schemes. I. *SIAM J. Numer. Anal. 24*(2), 279–309.

Hartmann, R. (2006). Adaptive discontinuous Galerkin methods with shock-capturing for the compressible Navier-Stokes equations. *Internat. J. Numer. Methods Fluids 51*(9-10), 1131–1156.

Hartmann, R. and P. Houston (2002). Adaptive discontinuous Galerkin finite element methods for the compressible Euler equations. *J. Comput. Phys. 183*(2), 508–532.

Hesthaven, J. S. and T. Warburton (2002, September). Nodal high-order methods on unstructured grids. *J. Comput. Phys. 181*, 186–221.

Hirsch, C. (1990). *Numerical Computation of Internal and External Flows, Volume 2, Computational Methods for Inviscid and Viscous Flows*. Brussels, Belgium: John Wiley & Sons.

Holden, H., K.-A. Lie, and N. H. Risebro (1999). An unconditionally stable method for the Euler equations. *J. Comput. Phys. 150*(1), 76 – 96.

Hoteit, H., P. Ackerer, R. Mosé, J. Erhel, and B. Philippe (2002). New two-dimensional slope limiters for discontinuous Galerkin methods on arbitrary meshes. Research Report RR-4491, INRIA.

Hughes, T., J. Cottrell, and Y. Bazilevs (2005). Isogeometric analysis: CAD, finite elements, NURBS, exact geometry and mesh refinement. *Comput. Methods Appl. Mech. Engrg. 194*(39-41), 4135 – 4195.

Hughes, T. J. R. and M. Mallet (1986a). A new finite element formulation for computational fluid dynamics. III. The generalized streamline operator for multidimensional advective-diffusive systems. *Comput. Methods Appl. Mech. Engrg. 58*(3), 305–328.

Hughes, T. J. R. and M. Mallet (1986b). A new finite element formulation for computational fluid dynamics. IV. A discontinuity-capturing operator for multidimensional advective-diffusive systems. *Comput. Methods Appl. Mech. Engrg. 58*(3), 329–336.

Hughes, T. J. R., M. Mallet, and A. Mizukami (1986). A new finite element formulation for computational fluid dynamics. II. Beyond SUPG. *Comput. Methods Appl. Mech. Engrg. 54*(3), 341–355.

Johnson, C. and J. Pitkäranta (1986). An analysis of the discontinuous Galerkin method for a scalar hyperbolic equation. *Math. Comp. 46*(173), 1–26.

Koornwinder, T. H. (1992). Askey-Wilson polynomials for root systems of type $BC$. In *Hypergeometric functions on domains of positivity, Jack polynomials, and applications (Tampa, FL, 1991)*, Volume 138 of *Contemp. Math.*, pp. 189–204. Providence, RI: Amer. Math. Soc.

Krivodonova, L. (2007). Limiters for high-order discontinuous Galerkin methods. *J. Comput. Phys. 226*(1), 879–896.

Kuzmin, D. (2010, April). A vertex-based hierarchical slope limiter for p-adaptive discontinuous Galerkin methods. *J. Comput. Appl. Math. 233*, 3077–3085.

Lapidus, A. (1967). A detached shock calculation by second order finite differences. *J. Comput. Phys. 2*, 154–177.

Lasaint, P. and P.-A. Raviart (1974). On a finite element method for solving the neutron transport equation. In *Mathematical aspects of finite elements in partial differential equations (Proc. Sympos., Math. Res. Center, Univ. Wisconsin, Madison, Wis., 1974)*, pp. 89–123. Publication No. 33. Math. Res. Center, Univ. of Wisconsin-Madison, Academic Press, New York.

Lee, M., J. Crittenden, V. Snoeyink, and M. Ari (1983). Design of carbon beds to remove humic substances. *Journal of Environmental Engineering 109*(3), 631–645.

LeVeque, R. J. (1992). *Numerical methods for conservation laws* (Second ed.). Lectures in Mathematics ETH Zürich. Basel: Birkhäuser Verlag.

LeVeque, R. J. (2002). *Finite Volume methods for hyperbolic problems*. Cambridge Texts in Applied Mathematics. Cambridge: Cambridge University Press.

Li, Z. and R. Yang (1999). Concentration profile for linear driving force model for diffusion in a particle. *AIChE Journal 45*(1), 196–200.

Liu, Y., M. Vinokur, and Z. J. Wang (2006). Spectral difference method for unstructured grids. I. Basic formulation. *J. Comput. Phys. 216*(2), 780–801.

Luo, H., J. D. Baum, and R. Löhner (2007). A hermite WENO-based limiter for discontinuous Galerkin method on unstructured grids. *J. Comput. Phys. 225*(1), 686–713.

Maday, Y., S. M. Ould Kaber, and E. Tadmor (1993). Legendre pseudospectral viscosity method for nonlinear conservation laws. *SIAM J. Numer. Anal. 30*(2), 321–342.

Mavriplis, C. (1994). Adaptive mesh strategies for the spectral element method. *Comput. Methods Appl. Mech. Engrg. 116*, 77–86.

Montlaur, A., S. Fernández-Méndez, and A. Huerta (2008). Discontinuous Galerkin methods for the stokes equations using divergence-free approximations. *Internat. J. Numer. Methods Fluids 57*(9), 1071–1092.

Moukalled, F. and M. Darwish (2001). A high-resolution pressure-based algorithm for fluid flow at all speeds. *J. Comput. Phys. 168*(1), 101–133.

Nadukandi, P. (2011, May). *Stabilized finite element methods for convection-difusion-reaction, Helmholtz and Stokes problems*. Ph. D. thesis, Universitat Politècnica de Catalunya, Barcelona, Spain.

Nguyen, N., P. Persson, and J. Peraire (2007). RANS solutions using high order discontinuous Galerkin methods. In *Proc. of the 44th AIAA Aerospace Sciences Meeting and Exhibit*, Reno, Nevada. AIAA-2007-0914.

Nogueira, X., I. Colominas, L. Cueto Felgueroso, F. Navarrina, and M. Casteleiro (2009). Detección de ondas de choque mediante el método de minimos cuadrados móviles para discretizaciones de alto orden en mallas no estructuradas. In *Proceedings of Congreso de Metodos Numericos en Ingenieria 2009*, Barcelona, España.

Oimstead, K. and W. Weber (1990). Statistical analysis of mass-transfer parameters for sorption processes and models. *Environmental Science and Technology 24*(11), 1693–1700.

Osher, S. (1984). Riemann solvers, the entropy condition, and difference approximations. *SIAM J. Numer. Anal. 21*(2), 217–235.

Peraire, J. and P.-O. Persson (2008). The compact discontinuous Galerkin (CDG) method for elliptic problems. *SIAM J. Sci. Comput. 30*(4), 1806–1824.

Pérez-Foguet, A. and A. Huerta (2005). Caracterización adimensional del comportamiento de las ecuaciones de transporte en medios altamente adsorbentes. In *Proceedings of the Congresso de Métodos Numéricos en Ingeniería, Granada, SEMNI*.

Persson, P. and J. Peraire (2006). Sub-cell shock capturing for discontinuous Galerkin methods. In *Proc. of the 45th AIAA Aerospace Sciences Meeting and Exhibit*, Reno, Nevada. AIAA-2006-0112.

Peterson, T. E. (1991). A note on the convergence of the discontinuous Galerkin method for a scalar hyperbolic equation. *SIAM Journal on Numerical Analysis 28*(1), pp. 133–140.

Piegl, L., , and W. Tiller (1995). *The NURBS book*. London, UK: Springer-Verlag.

Premasuthan, S., C. Liang, and A. Jameson (2010). Computation of flow with shocks using Spectral Difference scheme with artificial viscosity. In *Proc. of the 48th AIAA CAerospace Sciences Meeting including the New horizons Forum and Aerospace Esposition*, Orlando, FL. AIAA-2010-1449.

Rahman, M., F. Amiri, and E. Worch (2003). Application of the mass transfer model for describing nonequilibrium transport of HOCs through natural geosorbents. *Water Research 37*, 4673–4684.

Reed, W. and T. Hill (1973). Triangular mesh methods for the neutron transport equation. Technical Report Technical Report LA-UR-73-479, Los Alamos Scientific Laboratory, Los Alamos.

Richter, G. R. (1988). An optimal-order error estimate for the discontinuous Galerkin method. *Math. Comp. 50*(181), 75–88.

Roy, D., G. Wang, and D. Adrian (1993). A simplified solution technique for carbon adsorption model. *Water Research 27*(6), 1033–1040.

Sevilla, R. (2009). *NURBS-Enhanced finite element method (NEFEM)*. Ph. D. thesis, Universitat Politècnica de Catalunya, Barcelona, Spain.

Sevilla, R., S. Fernández-Méndez, and A. Huerta (2008). NURBS-enhanced finite element method (NEFEM). *Int. J. Numer. Methods Eng. 76*(1), 56–83.

Sherwin, S. J., R. M. Kirby, J. Peiró, R. L. Taylor, and O. C. Zienkiewicz (2006). On 2D elliptic discontinuous Galerkin methods. *International Journal for Numerical Methods in Engineering 65*(5), 752–784.

Shu, C.-W. (1988). Total-Variation-Diminishing time discretizations. *SIAM J. Sci. Statist. Comput. 9*(6), 1073–1084.

Shu, C.-W. and S. Osher (1988). Efficient implementation of essentially nonoscillatory shock-capturing schemes. *J. Comput. Phys. 77*(2), 439–471.

Shu, C.-W. and S. Osher (1989). Efficient implementation of essentially non-oscillatory shock-capturing schemes, II. *J. Comput. Phys. 83*(1), 32 – 78.

Silvester, P. (1969). High-order polynomial triangular finite elements for potential problems. *International Journal of Engineering Science 7*(8), 849 – 861.

Sircar, S. and J. Hufton (2000). Why does the linear driving force model for adsorption kineticswork? *Adsorption 7*, 137–147.

Smith, E. (1991). Modified solution of homogeneous surface diffusion model for adsorption. *Journal of Environmental Engineering 117*(3), 320–338.

Smith, E. (1996). Uptake of heavy metals in batch systems by a recycled iron-bearing material. *Water Research 30*(10), 2424–2434.

Sod, G. (1978). A survey of several Finite Difference methods for systems of nonlinear hyperbolic conservation laws. *J. Comput. Phys. 27*(4), 1–31.

Sonetaka, N., H.-J. Fan, S. Kobayashi, Y.-C. Su, and E. Furuya (2009a). Characterization of adsorption uptake curves for both intraparticle diffusion and liquid film mass transfer controlling systems. *Journal of Hazardous Materials 165*, 232–239.

Sonetaka, N., H.-J. Fan, S. Kobayashi, Y.-C. Su, and E. Furuya (2009b). Simultaneous determination of intraparticle diffusivity and liquid film mass transfer coefficient from a single-component adsorption uptake curve. *Journal of Hazardous Materials 164*, 1447–1451.

Sperlich, A., S. Schimmelpfennig, B. Baumgarten, A. Genz, G. Amy, E. Worch, and M. Jekel (2008). Predicting anion breakthrough in granular ferric hydroxide (GFH) adsorption filters. *Water Research 42*, 2073–2082.

Sperlich, A., A. Werner, A. Genz, G. Amy, E. Worch, and M. Jekel (2005). Breakthrough behavior of granular ferric hydroxide (GFH) fixed-bed adsorption filters: modeling and experimental approaches. *Water Research 39*, 1190–1198.

Spiteri, R. J. and S. J. Ruuth (2002). A new class of optimal high-order strong-stability-preserving time discretization methods. *SIAM J. Numer. Anal. 40*(2), 469–491.

Sun, L., P. L. Queré, and M. Levan (1996). Numerical simulation of diffusion-limited psa process models by finite difference methods. *Chemical Engineering Science 51*(24), 5341–5352.

Tadmor, E. (1990, July). Shock capturing by the spectral viscosity method. *Comput. Methods Appl. Mech. Engrg. 80*, 197–208.

Toro, E. F. (1999). *Riemann solvers and numerical methods for fluid dynamics* (Second ed.). Berlin: Springer-Verlag. A practical introduction.

Traegner, U. and M. Suidan (1989a). Evaluation of surface and film diffusion coefficients for carbon adsorption. *Water Research 23*(3), 267–273.

Traegner, U. and M. Suidan (1989b). Parameter evaluation for carbon adsorption. *Journal of Environmental Engineering 115*(1), 109–128.

van Leer, B. (1974). Towards the ultimate conservative difference scheme. II. Monotonicity and conservation combined in a second-order scheme. *J. Comput. Phys. 14*(4), 361 – 370.

van Leer, B. (1977a). Towards the ultimate conservative difference scheme III. Upstream-centered finite-difference schemes for ideal compressible flow. *J. Comput. Phys. 23*(3), 263 – 275.

van Leer, B. (1977b). Towards the ultimate conservative difference scheme. IV. A new approach to numerical convection. *J. Comput. Phys. 23*(3), 276 – 299.

van Leer, B. (1979). Towards the ultimate conservative difference scheme V. A second-order sequel to Godunov's method. *J. Comput. Phys. 32*(2), 1–36.

Venkatakrishnan, V. (1995). Convergence to steady state solutions of the Euler equations on unstructured grids with limiters. *J. Comput. Phys. 118*(1), 120–130.

Von Neumann, J. and R. D. Richtmyer (1950). A method for the numerical calculation of hydrodynamic shocks. *J. Appl. Phys. 21*, 232–237.

Weber, W. and J. Crittenden (1975). Madam i: A numeric method for design of adsorption systems. *Journal (Water Pollution Control Federation) 47*(5), 924–940.

Weber, W. and E. Smith (1986). Removing dissolved organic contaminants from water. *Environmental Science and Technology 20*(10), 970–979.

Weber, W. and E. Smith (1987). Simulation and design models for adsorption processes. *Environmental Science and Technology 21*(11), 1040–1050.

Woodward, P. and P. Colella (1984). The numerical-simulation of two-dimensional fluid-flow with strong shocks. *J. Comput. Phys. 54*(1), 115–173.

Xu, Z. and Y. Liu (2011). A conservation constrained Runge-Kutta Discontinous Galerkin method with the improved CFL condition for conservation laws. *submitted to SIAM J. Sci. Comput.*.

Zhu, J., J. Qiu, C.-W. Shu, and M. Dumbser (2008). Runge-kutta discontinuous Galerkin method using WENO limiters II: Unstructured meshes. *J. Comput. Phys. 227*(9), 4330 – 4353.

# Index